ALMA MATER STUDIORUM
UNIVERSITÀ DEGLI STUDI DI BOLOGNA
FACOLTÀ DI SCIENZE

DOTTORATO DI RICERCA IN FISICA

TITOLO DELLA TESI:

Structural and Electronic study of High-k dielectric thin films on Si(100)

Candidato: Marco Malvestuto

Relatore:
Prof. Federico Boscherini

Coordinatore Dottorato:
Prof. Roberto Soldati

CICLO DOTTORATO: XVIII
SETTORE DISCIPLINARE DI AFFERENZA: FIS/03 FISICA DELLA MATERIA

REFERENCES

Contents

Abstract 1

1 Introduction 3
1.1 Scaling of Si-based devices . . . 4
1.2 High-κ Dielectrics . . . 5
1.3 Open problems . . . 7
1.3.1 The choice of High-K oxides . . . 7
1.3.2 The Oxide stability . . . 8
1.3.3 The band alignment . . . 9
1.3.4 A model for band offsets . . . 9

2 Experimental Techniques 13
2.1 XAS . . . 14
2.1.1 A Brief Overview of X-ray Absorption Spectroscopy . . . 14
2.1.2 X-ray absorption Physics . . . 16
2.1.3 Single scattering XAFS formula . . . 18
Multiple scattering formalism . . . 23
2.1.4 XAS measurements . . . 26
2.2 X-ray reflectivity . . . 29
2.2.1 reflEXAFS . . . 29
Refl-EXAFS at GILDA beamline: experimental apparatus . . . 30
2.2.2 Absortpion measurements at Y, Lu, Yb, and Hf edges . . . 30
2.2.3 Absortpion measurements at Oxygen K-edge . . . 32
2.2.4 Data analysis . . . 33
Fourier filtering . . . 36
Fitting refinement algorithm . . . 36
2.3 photoelectron spectroscopy [1, 2, 3, 4] . . . 38
The photo-excitation process . . . 39
Three step model . . . 39
one step model . . . 41
Core level spectroscopy . . . 42
2.3.1 Data analysis . . . 43
Line shape . . . 43
background removal . . . 44
The fitting program . . . 44

3 Sample growth 45
3.1 Sample Growth of Y_2O_3/Si(100) . . . 45
3.1.1 Film growth [5] . . . 45
3.1.2 Structural characterization of $Y_2O_3/Si(100)$ . . . 46
3.2 Introduction to Atomic Layer Deposition (ALD) . . . 50
3.2.1 Example of an ALD deposition process. . . . 51

3.2.2 ALD deposition of Lu_2O_3 and Yb_2O_3 films on Si (100). 55
Si substrate preparation 55
Film growth. 55
3.2.3 X-ray diffraction analysis of Lu_2O_3 and Yb_2O_3 powders . . . 56
3.2.4 Film characterization 57
3.2.5 Chemical bonding in Lu_2O_3 and Yb_2O_3: XPS study 59
3.3 Physical Vapor Deposition of Lu_2O_3 on Si(100) in Ultra High Vacuum conditions 63
3.3.1 Physical Vapor Deposition (PVD) 64
Experimental set-up. 64
The PVD Source 64
The crucible 64
The anode electrical insulation. 67
3.3.2 The calibration of the PVD Source. 68
3.3.3 Sample growth. 71
Substrate preparation 71
Stoichiometry 74
Deposition of Lutetium oxide films. 75
Data and Results 77
3.3.4 Conclusions 85

4 Results **87**
4.1 Y_2O_3/Si(100) 88
4.1.1 The Y K-edge 88
4.1.2 XAS data and analysis methods 88
4.1.3 The O K-edge 93
4.1.4 Discussion 95
4.1.5 Local structure of Y_2O_3 epilayers 95
4.1.6 Near interface structure 97
4.1.7 XANES and electronic structure of Yttrium (Transition Metal) oxide 98
Peaks A1 and A2 99
Peak B 100
Peaks C1 and C2 100
Molecular Orbitals 101
conclusions 102
4.1.8 CONCLUSIONS 106
4.2 XAS study of Lu_2O_3/Si(100) and Yb_2O_3/Si(100) films grown by ALD 107
4.2.1 X-ray absorption measurements and data analysis 107
4.2.2 Discussion 109
4.2.3 XANES and electronic structure of Lutetium and Ytterbium oxides 110

5 Atomic and electronic structure of Lu_2O_3/Si(100): $in-situ$ synchrotron radiation photoemission. 113

5.1 Photoemission measurements 114

5.1.1 Si $2p$ core level photoemission 114

5.1.2 O $1s$ core level photoemission 121

5.1.3 Valence Band photoemission. 124

5.1.4 Offset measurement 125

Method I 125

Method II 125

5.2 O K-edge XAS spectra. 127

5.3 TEM investigation 129

5.4 Conclusions 129

Conclusions 133

Bibliografy 135

Abstract

In this thesis an experimental study of the atomic and electronic structure of a class of high dielectric constant oxides and their interfaces with silicon is reported; these material systems are actively studied at present because of their potential applications in the field of microelectronic devices. X-ray absorption spectroscopy and photoemission spectroscopy, both using synchrotron radiation, were the main experimental techniques employed; Auger electron spectroscopy, low energy electron diffraction, atomic force microscopy, and transmission electron microscopy provided complementary information. Analysis of the x-ray absorption spectra was aided by *ab-initio* simulations using multiple scattering theory. The main topics addressed in this thesis are:

1. The local atomic structure at the initial stages of growth of yttrium oxide (Y_2O_3), lutetium oxide (Lu_2O_3) and ytterbium oxide (Yb_2O_3) thin films deposited on Si, with particular reference to the issue of thermodynamical stability and to the identification of the interface phases.

2. The set-up of a physical vapor deposition source for the growth in ultra high vacuum of Lu_2O_3 on Si(001).

3. The band alignment at the Lu_2O_3/Si(001) interface, studied by means of an *in-situ* photoemission experiment.

Concerning the first point, a number of thin and ultra-thin films deposited by means of different deposition techniques were studied. X-ray absorption spectroscopy measurements were performed both at the cation K- and L- edges (at the GILDA beamline at ESRF, Grenoble) and at the oxygen K-edge (at the BEAR beamline at ELETTRA, Trieste). Because of the limited thickness of the films measurements with high surface sensitivity were performed, also using the grazing incidence geometry in the hard X-ray region. The results provided original insight on the local atomic structure of the films and clarified the nature of interface layer. We found that this interface layer is most often a non-stoichiometric Si oxide with silicate-like and silicide-like atomic configurations also present in some cases. These assignments, confirmed also by *in-situ* photoemission spectroscopy results, illustrate the thermodynamical instability of these oxides in contact with Si in all cases investigated.

In order to perform in - situ photoemission spectroscopy experiments it was necessary to set - up and characterize a physical vapor deposition source for the growth in ultra high vacuum of Lu_2O_3 ultra thin films on Si(100). A detailed analysis and optimization of the source parameters was carried out. The stoichiometry, morphology

and long range order of the deposited layers was studied as a function of the deposition temperature and annealing treatments.

Thanks to the successful set-up of the source it was possible to perform an *in-situ* photoemission experiment on the Lu_2O_3/Si(100) interface, on the BEAR beamline at ELETTRA. This experiment provided original data on the atomic structure and interdiffusion at the interface, and allowed a measurement of the valence band discontinuity on an interface obtained under controlled conditions.

This thesis is composed of five chapters.

- *Chapter 1* provides a brief introduction to the study of high dielectric constant materials as replacements for SiO_2 as gate dielectrics in CMOS devices.

- *Chapter 2* describes the experimental techniques exploited, paying particular attention to x-ray absorption spectroscopy and photoemission.

- *Chapter 3* describes the growth techniques and post-growth treatments of the samples; the set-up and optimization of the physical vapor deposition Lu_2O_3 source and a structural characterization of the films deposited using it are also reported.

- *Chapter 4* reports results on ex-situ deposited samples.

- *Chapter 5* illustrates results on *in-situ* deposited samples.

This Ph. D. thesis was made possible by a grant from ”Commissione Luce di Sincrotrone” of INFM (Istituto Nazionale per la Fisica della Materia), now a part of CNR (Consiglio Nazionale delle Ricerche). Funding was also provided by ”Sezione E: semiconduttori ed isolanti” of INFM within project REOHK, and from Alma Mater Studiorum - University of Bologna. The set-up of the physical vapour deposition source was performed at the TASC laboratory of INFM and I would like to thank that laboratory and staff for hospitality. The many experimental sessions using synchrotron radiation were performed at ESRF (GILDA beamline) and ELETTRA (BEAR beamline), successive to approval of the scientific program by the review panels of those facilities; these experiments were made possible by user support program of INFM.

I thank Professor Federico Boscherini for his support throughout this research program. I trust that the results of this project fulfill his hopes and expectations for the work.

During the course of this work I have greatly benefitted from the experience and insightful guidance of many senior scientists. I would like to especially thank Prof. S. Nannarone, Dr. M. Pedio, Prof. M. Fanciulli, Dr. G. Scarel, and Dr. F. D’Acapito.

Bologna, March 15th, 2006.

Chapter 1

Introduction

1.1 Scaling of Si-based devices

In a groundbreaking article written in 1965, Gordon Moore described exponential growth in the number of transistors per integrated circuit and predicted this trend would continue. Moores Law, states that the number of transistors on integrated circuits doubles approximately every 24 months, resulting in higher performance at lower cost. This simple statement is the foundation of semiconductor and computing industries. It is the basis for the exponential growth of computing power, component integration that has stimulated the emergence of generation after generation of PCs and intelligent devices. Perhaps the most vital question for the industry is: how much longer can Moores Law continue? The silicon-based microelectronics industry, the leading feature of the silicon age, has made continuous progress since the beginning some 40 years ago. Its evolution is commonly quantified by the increasing performance of the logic and memory devices as a function of time. The technological route followed by the Si-based microelectronics industry was an increasingly complex optimization of a relatively small set of interrelated constituent materials and fabrication processes, which allowed to perform a calculated reduction on the dimensions, called "scaling" of the fundamental device in the circuits: the Si-based metal-oxide-semiconductor field-effect transistor (MOSFET). In particular, metal-oxide-semiconductor structures or capacitors used in memory (e.g. dynamic random-access memory, DRAM) and logic (MOSFET) devices are made out of doped single- and polycrystalline silicon together with amorphous, thermally grown silicon dioxide (SiO_2). Key elements enabling the scaling of Si MOSFETs are the materials (and resultant electrical) properties associated with the dielectric employed to isolate the transistor gate form the Si channel, namely SiO_2. (fig 1.1 shows a schematic representation on a MOSFET). The use

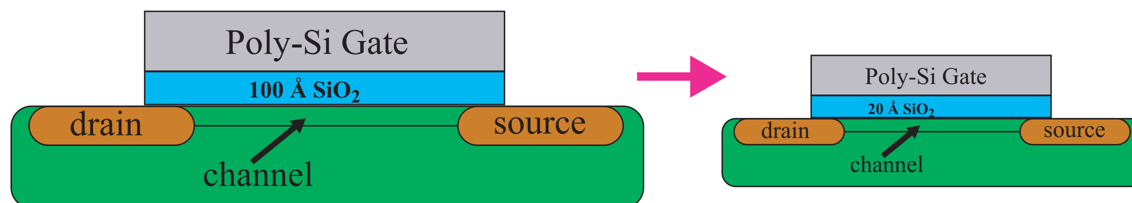

Figure 1.1: Scaling of MOSFET

of amorphous, thermally grown SiO_2 as a gate dielectric provides thermodynamically and electrically stable, high-quality Si-SiO_2 interface with superior electrical isolation properties. The progress represented by Moore's law is best characterized as a steep but smooth development, having achieved with no major revolution in fundamental device designs and non changes in the basic materials that constitute the "heart" of the MOSFET: Si and SiO_2. Nevertheless, the outstanding evolution of the silicon age is rapidly approaching a saturation point where device fabrication con no longer be simply scaled to progressively smaller sizes. As transistor geometries scale to the point where the traditional silicon dioxide (SiO_2) gate dielectric becomes just a few atomic

layers thick, tunneling current leakage and the resulting increase in power dissipation and heat become critical issues. Solving the gate dielectric problem is a critical issue for the industry. The 1998 Technology Roadmap for Semiconductors indicates that the present rate of device scaling will produce 100 nm generation devices using equivalent gate oxide thicknesses of 1.5 - 2 nm in 2005. The recently published version of the Roadmap demands reduction of the oxide thickness at an even faster rate. The

year of first product shipment	1997	1999	2001	2002	2005	2008	2011
technology generation	250 nm	180 nm	150 nm	130 nm	100 nm	70 nm	50 nm
equivalent oxide thicknes EOT (nm)	4-5	3-4	2-3	2-3	1.5-2*	≤1.5**	≤1.0**

Table 1.1: *solutions researched, ** no known solution

international Tech Road-map for Semiconductors foresees that further development in Si-based integrated circuits will rely on the use of alternative materials with dielectric constants much higher than that of silicon oxide (see figure 1.2).

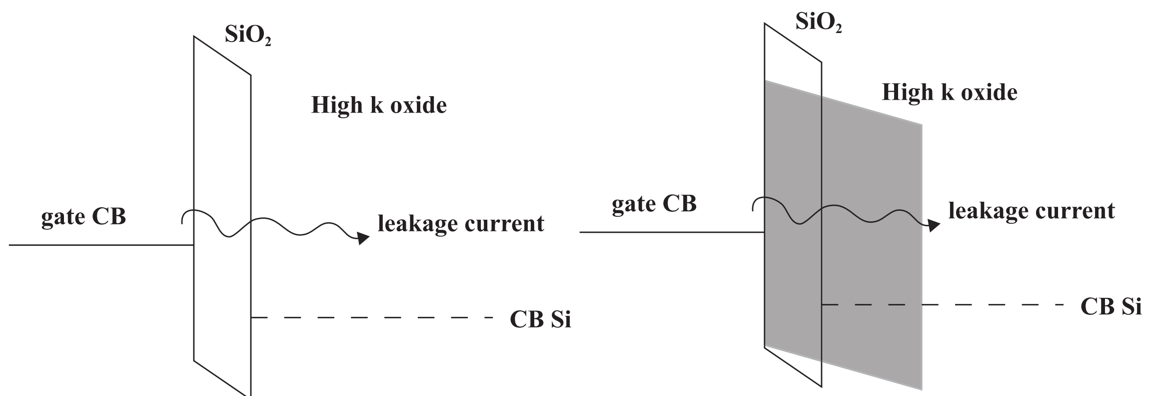

Figure 1.2: High-K material reducing tunneling leakage current.

1.2 High-κ Dielectrics

The silicon dioxide layer between the gate and substrate of conventional MOSFET devices has a major influence on the electrical behavior of the device. In order to successfully replace the SiO_2 dielectric with an alternative material, a long list of physical and electrical demands will have to be met. The ideal solution to reduce the gate leakage current would be simply replacing the SiO_2 layer with a different dielectric material, manufactured in an equally complex process step. Unfortunately, no material shows

exactly the same behaviour as silicon dioxide in combination with a significantly reduced gate leakage current. The typical leakage current of SiO_2, at a gate bias of 1 V, changes from $10^{-12} A/cm^2$ at 35 Åto $10^{-15} A/cm^2$ at 15 Å. For use in deep submicron CMOS technologies, the leakage current of the gate dielectric has to be less than $10^{-8} A/cm^2$. To avoid high leakage currents and still achieve the required capacitance, a material with higher permittivity will have to be used. The following formula shows the device parameters that determine the resulting gate capacitance:

$$C_{ox} = \kappa_{ox} \cdot \varepsilon_0 \cdot A/t_{ox} \tag{1.1}$$

The layer thickness (t_{ox}) can be increased to avoid high leakage currents, only when a material is used with higher relative permittivity κ_{ox}. Parameter A is the capacitance area, which will only be smaller in future semiconductor technologies (cosi dice Road map). The permittivity of free space is represented by the constant ε_0. Dielectric layers of different materials can be compared with the use of the equivalent oxide thickness (EOT) parameter (t_{eq}). This is the thickness of a silicon dioxide layer with similar gate capacitance. The EOT can be calculated with the following formula:

$$t_{eq} = (\kappa_{SiO_2}/\kappa_{ox}) \cdot t_{ox} \tag{1.2}$$

Research on alternative gate dielectrics can now be defined as finding a material with a very low leakage current and a very small equivalent oxide thickness. However, the actual thickness of the dielectric layer (t_{ox}) is an important parameter for the process technology. The following list shows some of the other requirements of a new gate dielectric:

- a high breakdown voltage to withstand the large electric fields (see figure 1.7)
- no build-in charge
- good adhesion to other process materials (silicon substrate and gate material)
- low defect density (no pinholes)
- easy to be etched
- flat surface to enable gate and metal interconnect manufacturing
- thermal stability (high temperature process steps)
- low processing temperature

Three types of dielectric materials can be found in literature: ferro-electric materials, polymers and metaloxides. The first group contains $Pb(Zr,Ti)O_3$ (PZT), $SrBi_2Ta_2O_9$ (SBT) and $(Ba,Sr)TiO_3$ (BST), which are materials with a very high dielectric constant (κ_{ox} = 300 ... 800). Currently, these dielectrics are used in high density DRAM capacitors and non-volatile ferro-electric RAM (FRAM). In the latter, the polarization characteristics of the material are used. Metaloxides have dielectric constants lower than the ferro-electric materials, but still higher than silicon dioxide. The following table shows the dielectric constants of candidate materials for future gate dielectrics.

material	formula	κ_{ox}
silicon oxide	SiO_2	3.0
Silicon nitride	Si_3N_4	7
Oxynitrides	$Si_xN_yO_z$	4 - 7
aluminum oxide	Al_2O_3	9
tantalum pentoxide	Ta_2O_5	25
hafnium oxide	HfO_2	30-40
zirconium oxide	ZrO_2	25
barium strontium titanate	$BaSrTiO_3$	300

Table 1.2:

1.3 Open problems

Since a high gate dielectric capacitance is required, an alternative to reducing the thickness is employing a high-κ dielectric (and keeping the thickness constant). This seemingly simple consideration raises numerous physical and technological issues. Among the most important physical problems, we may single out the understanding of the band alignment at the interface, of the atomic geometry at the initial stages of growth and of the system thermodynamic stability; the issues are clearly connected since the interface geometry will affect the stability and the presence of ”unwanted” interface phases will alter the band lineup, and complicate comparison to theory. From the applicative point of view, valence and conduction band discontinuities not smaller than 1 eV are required to limit carrier injection, and a sharp interface avoiding the presence of low-κ phases is a prerequisite for further decreases in dimensions. In 1998 McKee et. al. [6] reported the successful growth of epitaxial $SrTiO_3$ on Si(001), with abrupt interfaces; however, this encouraging result is still strongly debated in the scientific community. This problem calls for a combined effort in which experiment (preparation and measurement of well characterized interfaces) and theory (ab-initio simulation of the interface and its constituents) advance in close contact.

1.3.1 The choice of High-K oxides

Besides the by now classic transition-metal oxides such as HfO_2, rare-earth oxides are also actively studied worldwide as promising high- κmaterials. Most have values of the static dielectric constant in the range 12 - 25, significantly greater than the SiO_2 value of 3.9; the physical origin of this enhancement is the high lattice polarizability, due to the presence of low frequency vibrational modes and of partially anomalous atomic dynamical response [7]. Oxides under investigation, also by the present proposers, include La_2O_3, Pr_2O_3, Yb_2O_3, Lu_2O_3, $LaAlO_3$, Dy_2O_3, $DyScO_3$, and others; many have cubic lattice parameters close to double the value of Si, suggesting that epitaxial growth might be favorable. Some devices which utilize high- dielectrics have been realized, mostly with amorphous HfO_2 or silicates; however, no consensus has been reached on the optimal material for application, nor has a comprehensive understanding of the underlying physics been attained - to put it politely.

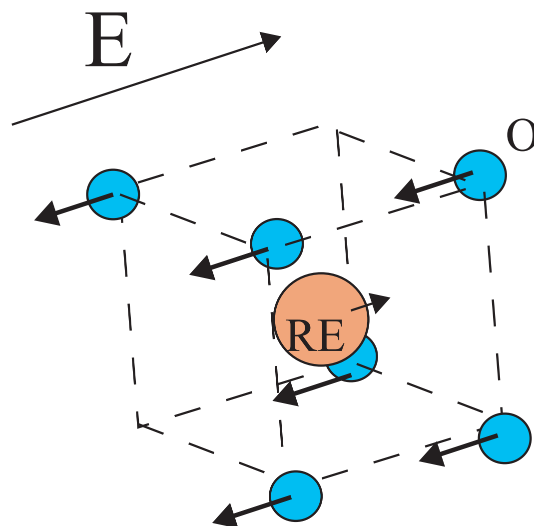

Figure 1.3:

1.3.2 The Oxide stability

The stability of oxides on Si has been initially studied with the help of tabulated thermodynamic data for bulk materials; such a ”macroscopic” approach, although useful as a starting point, is not expected to be able to adequately describe processes which take place at the interface. Experimentally, one generally observes the formation of a thin ”interface layer” between Si and the oxide proper. This interface layer, the thickness of which is 5-10 Å, is most often a non-stoichiometric Si oxide, with occasional silicate-like atomic coordination. Spectroscopic investigations by some of the proposers [8], [9],[10] and others confirm this assignment. Since series capacitances add in reciprocal fashion (see figure 1.4), the presence of this low-κ interface layer adversely affects device performance. An understanding of the driving processes for

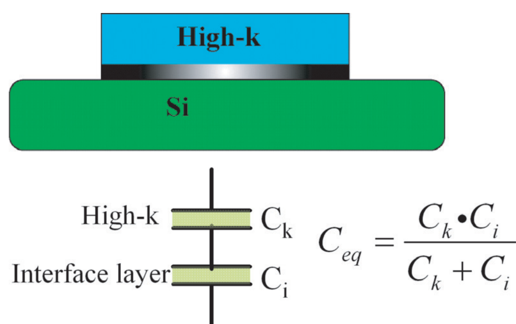

Figure 1.4:

interface layer formation is lacking at present. It must rely on the study of the first

stages of the adsorption process, ideally in a clean, ultra high vacuum, environment.

1.3.3 The band alignment

The band alignment problem has been first studied empirically, adapting the metal-induced gap states (MIGS) model of metal-semiconductor interfaces [11], [12]. The behavior of high-κ / Si interfaces is predicted to be generally halfway between the Bardeen and Schottky limits; predicted values for the band alignment are generally in good (within 0.1 eV) to modest (0.5-1 eV) agreement with experiment, but then, of course, this approach includes no information about the actual interface. Other more realistic, but also more complex, approaches have employed fully ab initio techniques,[13], [14] with a similar level of success. Clearly, when at all feasible, atomistic approaches should be preferred.: indeed, the detailed local structure can modify local dipoles and hence induce band offset changes at the level of 0.5 to 1 eV; [13], [14] incidentally this implies that proper experiment-theory comparison -and therefore the assessment of the success of a theoretical prediction- is generally difficult as the simulated local structure is not the same as the real one (which is typically unknown). Additional theoretical issues include the inclusion of many-body effects in the line-up,[13] our opinion being that these corrections must be included.

1.3.4 A model for band offsets

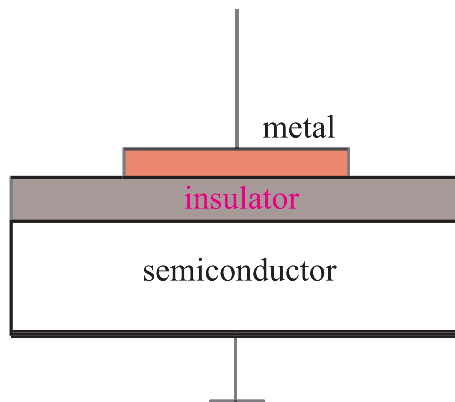

Figure 1.5: Metal-Oxide-Semiconductor diode.

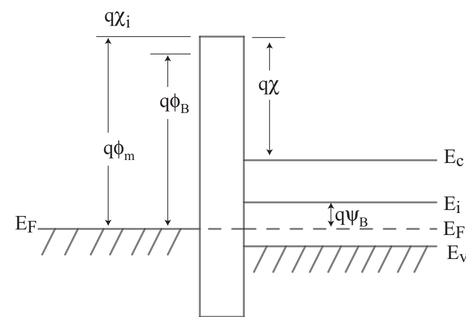

Figure 1.6: Energy band diagrams of ideal MOS diodes. da descrivere il significato

Interfaces between semiconductors and oxide are of eminent importance in semiconductor devices. The band line-up at oxide-semiconductor interfaces is one of the important design parameters in MOS field effect transistors. The electronic properties of contacts between a semiconductor and an oxide are determined by the alignment of the band structures across the interface and the existence of space-charge layers[16, 17]. Insulators may be considered as semiconductors with very large band gaps. A particular model to describe the band alignment in such systems is the model

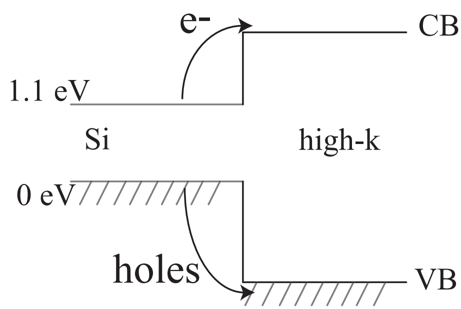

Figure 1.7:

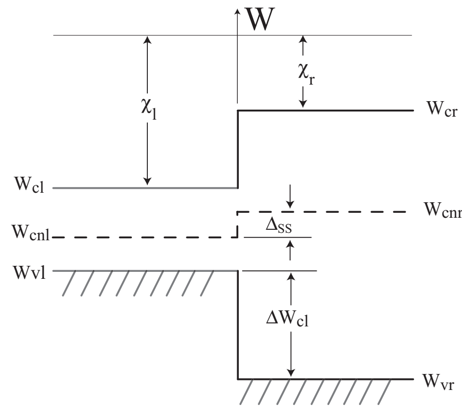

Figure 1.8: Band diagram of semiconductor-oxide exhibiting interface dipoles in the CLN methods.

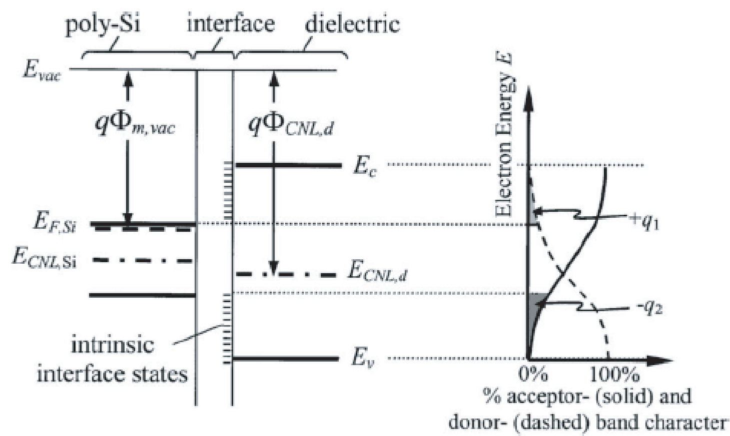

Figure 1.9: Energy band diagram (left!) and charging character of interface states (right) for silicon-dielectric interfaces. The shaded area represents the total negative charge on the dielectric side, while the gray region represents the total positive charge on the dielectric side [15].

of metal induced gap states (MIGS) [16, 17]. This model says that the reference level is the so-called charge neutrality level (CNL or branch points: the character of surface states changes across the band gap from predominantly donor- to acceptor-like closer to the valence-band top and the conduction-band bottom, respectively. The energy at which the contributions from both bands are equal in magnitude is called branch point or charge neutrality level) of the intrinsic surface states. A semiconductor surface has gap states due to the broken surface bonds. These are spread across the energy gap. The CNL is the highest occupied surface state on a neutral surface of a semiconductor 1.9. It is like a Fermi level of the intrinsic gap states. At abrupt interfaces, band edge discontinuities are established within a few atomic layers while he regions of band bending depend on the doping profiles on both sides of the contact and will extend over a few Debye lengths. Here, only the band edge offsets shall be considered. As at metal-semiconductor contacts, electronic interface-induced gap states (IFIGS) exist at semiconductor-oxide interfaces. In the example shown in fig.1.8, the valence band of the semiconductor on the left partly overlaps the band gap of the dielectric oxide on the right within the offset $\Delta W_v = W_{vr} - W_{vl}$ of the valence-band edges. In this energy range the wavefunctions of electrons near the valence-band minimum on the left will penetrate into the oxide in the right. The valence band discontinuity may then be written as

$$\Delta W_v = W_{vr} - W_{vl} = (W_{pd} - W_v)_l - (W_{pd} - W_v)_r + S \cdot \Delta_{ss} \tag{1.3}$$

$$VBO = (\chi_{ox} - W_{ox}) - (\chi_{Si} - W_{Si}) + S \cdot \Delta_{ss} \tag{1.4}$$

where S:

$$Bardeen = 0 < S < 1 = Schottky \tag{1.5}$$

The dipole contribution Δ_{ss} describes the charge transfer by the difference $X_{sl} - X_{sr}$ of the electro negativities of the semiconductor and the oxide in contact. The XPS method for determining valence band offsets is explained in the following paragraph 5.1.4.

The band offset consist of two components , a component intrinsic to the bulk oxide and Si χ_l and χ_r and a component which depends specifically on the interface bonding configuration [18, 19]. The intrinsic component is of interest because the specific bonding at the interface is generally not known[20]. Usually the intrinsic component is the main component. The band line up at an interface is controlled by a dipole formed by charge transfer across the bonds at the interface [17]. In the case of two non-interacting surfaces, the conduction band line up is given by the difference between the electron affinities (the energy of the conduction band edge below the vacuum level) (Fig. 1.8). This is known as the Schottky limit. If the surfaces interact, an interface dipole due to charge transfer across the interface by modifies this offset. The charge transfer acts to align an energy level in each surface. In the limit of strong coupling, known as the Bardeen limit, these levels are fully aligned. The band offset is then given by the difference of this energy level below the two conduction bands, and is independent of the vacuum levels. Most high K oxides are intermediate between the

two limits.

Chapter 2

Experimental Techniques

2.1 XAS

2.1.1 A Brief Overview of X-ray Absorption Spectroscopy

The term *X-ray Absortpion Fine strucutre* referes to oscillations in the absorption coefficient on the high energy side of an absrption edge. Such osccilations, first observed in 1931 by Kronig [21] can extend up to 100 eV above the edge, may have a magnitude of 10 % of the absorption jump (see fig 2.1) and are not present in the gaseous phase. Historically, the first measurements of the fine structure in x ray absorption

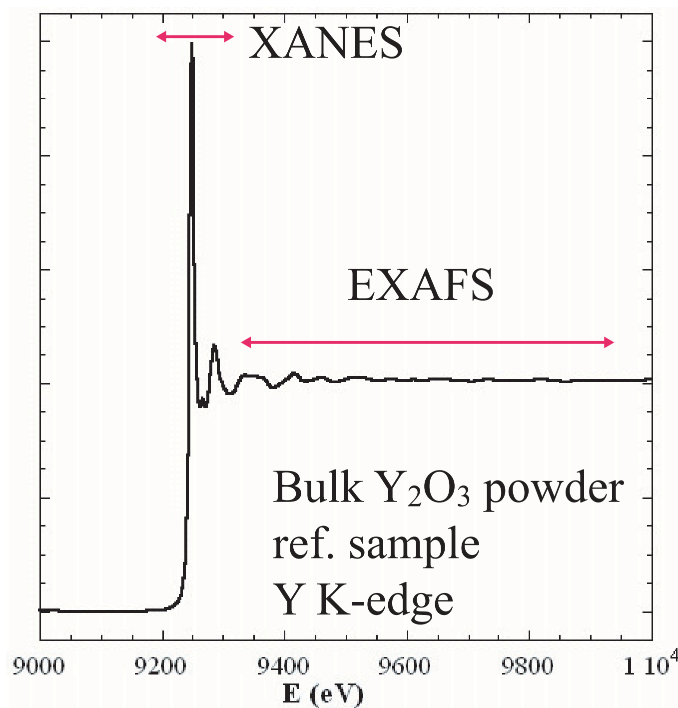

Figure 2.1: XAFS oscillation in the K absorption edge of Yttrium in bulk Y_2O_3 powder.

spec tra were made in 1920 by Fricke [22] and Hertz [23]. The first explanation, based on newly developed quantum mechanics, was given by Kronig [21] in 1931. He explained the finene structure in terms of the singularities at the Brillouin zone boundaries. Later, this became known as a long range order "'LRO"' theory. Also Kronig [21] interpreted the XAFS of the molecules in terms of a short range order "'SRO"' theory. He realized that the final state wave function should have modulations caused by the backscattering from the neighbors. The controversy between SRO and LRO explanations of the fine structure was resolved only 40 years later in 1971, when Sayers, Stern and Lytle [24] applied a Fourier transform with respect to the photoelectron wave vector. The peaks in Fourier transform were expected to be close to the distances to coordination shells of the absorbing atom [25]. This work showed that the SRO theory works for both molecules and solids. Thus it became clear that the extended

X-ray absorption fine structure (EXAFS) contains an important structural information concerning nearest neighbor distances and coordination numbers.

Another breakthrough was the availability of Synchrotron Radiation sources [26] (see figure 2.2) that delivered X-ray intensities orders of magnitude greater than rotating anodes, and reduced the time for acquiring a spectrum on a concentrate sample to the oreder of minutes.

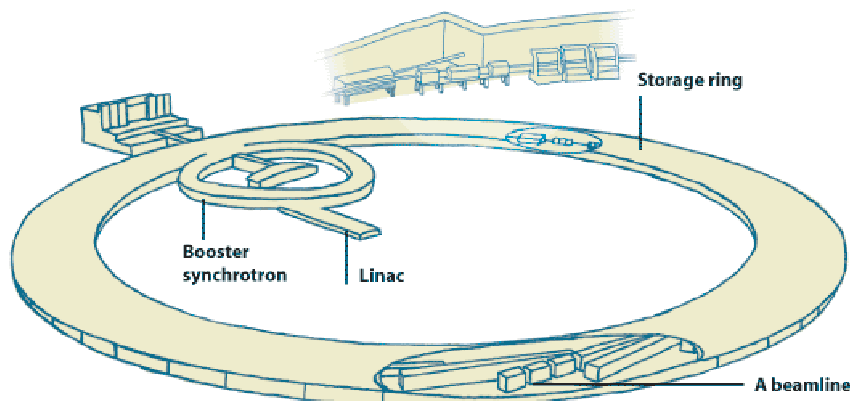

Figure 2.2: Schematic view of synchrotron radiation facility.

Nowadays it is established that a single scattering short range order therory is adequate under most circumstances, if we exclude the energy range immediately above the edge (up to about 30eV). In this renage, which is referred to as XANES region (acronym for X-ray Absorption Near edge Spectroscopy), the energy of the photoelectron is very small (its wavelenght is comparable with the interatomic distances), while its mean free path is quite high (some tenths of Å); as a consequence the probability for the photoelectron to be scattered form more than one atom in the surroundings of the absorber increases.

XAFS, with the use of state of art analysis tools, provides information on the local structure around the absorber which is energetically elected; by using this technique it is possible to measure the bond lengths distribution and to determine the number of neighbors of the absorber. In some particular case, XAFS permits also to identify unknown neighbors and/or to measure the relative number of different neighbor in a mixed shell. It can furnish information on the bond angles and on the geometry of the photo absorber site, by studying multiple scattering and exploiting the polarization dependence.

As a result, XAFS has become a very important investigation techniques in different scientific fields, such as physics, material science, chemistry, biology and biophysics; the local character of the probe made it complementary to X-ray Diffraction,

which provides on the contrary information on the long range order. XAFS will be addressed in details in the following.

During the 80's a number of theoretical groups developed ab initio codes for EXAFS analysis[27, 28, 29, 30, 31]. All of them are based on the multiple scattering (MS) theory.

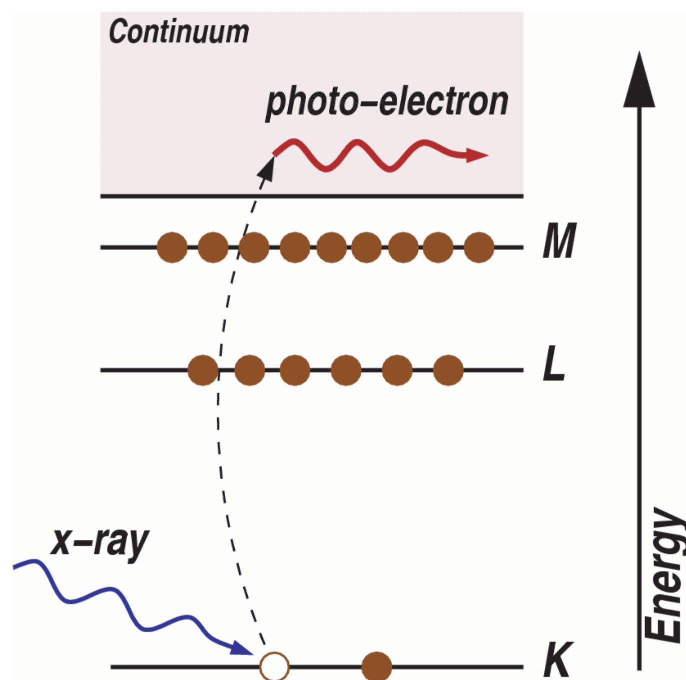

Figure 2.3: Photoelectric effect.

2.1.2 X-ray absorption Physics

In order for a particular electronic core level to participate in the absorption, the binding energy of this core level must be less than the energy of the incident x-ray 2.3. If the binding energy is greater than the energy of the x-ray, the bound electron will not be perturbed from the dell-defined quantum state and will not absorb the x-ray. If the binding energy of the electron is less than that of the x-ray, the electron may be removed from its quantum level. In this case, the x-ray is destroyed (i.e., absorbed) and any energy in excess of the electronic binding energy is given to a photo-electron that is ejected from the atom. When the core electron absorbs the photon, its energy is suddenly raised above the Fermi level. In this energy range, the stationary states are delocalized over the whole system (as molecular orbitals in molecules and band states in solids). Therefore, the photoelectron wave function spreads out from the absorption site and is scattered at the potentials of the surroundings atomic sites. The scattered waves are in turn scattered from all the other sites. The amplitude of the

photoelectron wave function at the absorption site (and thus the absorption cross section) is determined by the interference of these multiply scattered waves (figure 2.4). The mathematical formulation of these concepts leads to multiple scattering theory,

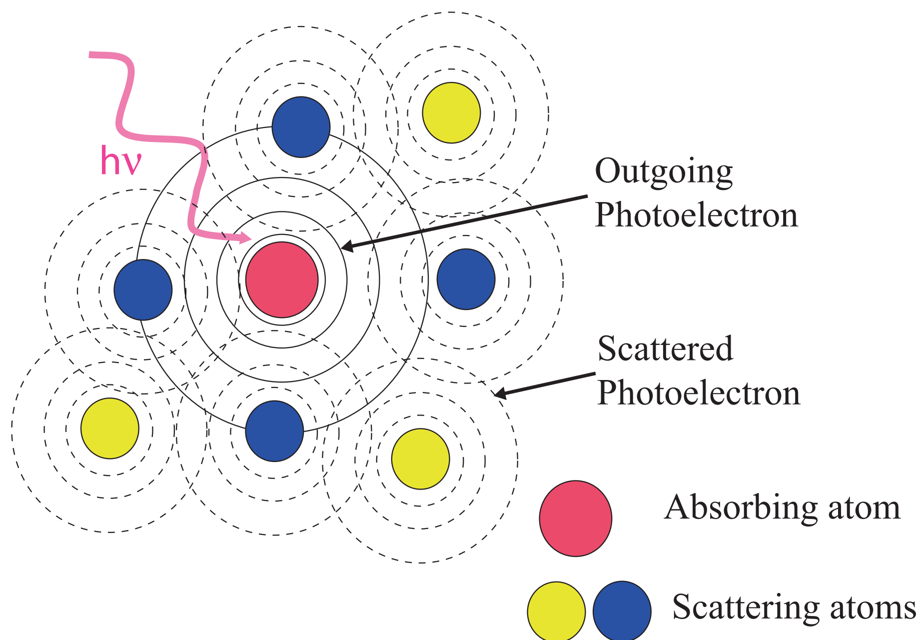

Figure 2.4: Pictorial view of the photoelectron self-interference effect, the atom in black absrobd the photon, the outgoing photoelectron wave is partially backscattered by the neighboring atoms.

which is physically intuitive, applicable to all kinds of materials from molecules to amorphous and crystalline solids, and sufficiently flexible to incorporate systematic improvements. The success of this spectrometry lies in the fact that the photoelectrons act as very sensitive probes that can feel the charge distribution and the arrangement of the neighbouring atoms around the absorbing atom, or, with other words, they can feel the arrangement of the neighbouring atoms (chemical environment). When the photon energy $\hbar\omega$ is low, the photoelectrons can populate either unoccupied bound states or low-lying continuum states. This part of the spectrum (Fig. 2.1) is called the XANES region; the acronym stands for $X - rayAbsorptionNear - EdgeStructure$. XANES spectra are unique to the oxidation state and speciation of the element of interest, and consequently is often used as a methods to determine the oxidation state and coordination environment of materials. XANES spectra are commonly compared to standards to determine which species are present in an unknown sample. Once species are identified, Their relative abundance is quantified using linear-combination fitting (or other curve-fitting algorithms) using XANES standards to reconstruct the experimental data. It is important to note that XANES is sensitive to bonding environment as well as oxidation state. Consequently, XANES is capable of discriminating species of similar formal oxidation state but different coordination. On its high-energy end,

XANES extends up to $ExtendedX - rayAbsorptionFineStructure$ [32, 33, 34, 35], EXAFS in short, where the photoelectron kinetic energy is high.EXAFS spectra are best described as a series of periodic sine waves that decay in intensity as the incident energy increases from the absorption edge. These sine waves result from the interaction of the elected photoelectron with the surrounding atomic environment. As such, their amplitude and phase depend on the local structure of excited atom. Since this interaction is well understood, theory is sufficiently advanced that the local structure of the excited atom can be determined by matching a theoretical spectrum to the experimental spectrum. This fitting yields many types of information, including the identity of neighboring atoms, their distance from the excited atom, the number of atoms in the shell, and the degree of disorder in the particular atomic shell (as expressed by the Debye-Waller factor).

When the x-ray photon energy increase, the absorption μ progressively decrease. This smooth behaviour is interrupted by sharp discontinuities, absorpion edge 2.1. These edges occur at a defined energy corresponding to the binding energy of the electron in the material. The ejected electron interacts with the surrounding atoms to produce the spectrum that is observed.

2.1.3 Single scattering XAFS formula

The intensity I_0 of an X-ray beam, when crossing an homogeneous sample of thickness x normally to its surface, is attenuated according to the exponential Lambert-Beer's law:

$$I = I_0 exp(-\mu x) \tag{2.1}$$

where I is the number of photons per time and cross section unit. The linear abosrption coefficient μ , related to the photoelectric effect, monotomically decreases as a function of energy. This is true expect at the energies coresponding to the photoelectric absopriotn form core levels; at these energies characteristic sharp edges are obseverd. μ is the reduction in the energy density u carried by the electromagnetic field, due to the interaction with the materil, which can be also expressed as:

$$\mu(\omega) = -\frac{1}{u}\frac{du}{dx} \tag{2.2}$$

$$u = \frac{\varepsilon_0 \omega^2 A_0^2}{2} \tag{2.3}$$

where A_0^2 is the amplitude of the vector potential associated to the electric field, whose maximum amplitude is E_0; ε_0 is the dielectric constant of vacuum. $\mu(\omega)$ depends on the atomic density of the sample n and on the probability of transition W_{fi} for the photoabsorber form the inital state $|\psi_i\rangle$ to the different possible final states $|\psi_f\rangle$, corresponding to possible different core holes or multiple excitations:

$$\mu(\omega) = \frac{2\hbar}{\varepsilon_0 \omega A_0^2} n \sum_f W_{fi} \tag{2.4}$$

In order to calcualte the probablitiy of transition W_{fi}, the time dependent perturbation theory is exploited, which permits to expand in series the interaction potential between the atom and the electromagnatic field, and to use the only first term of the series if the interaction is weak. The transition probability is in this way determined by the Fermi's golden rule: Fermis golden rule [[36, 37]]

$$Wfi = \frac{2\pi}{\hbar} \left| \langle \psi_i | \hat{H}_I \left| \psi_f \right\rangle \right|^2 \rho(E_f) \tag{2.5}$$

where $\rho(E_F)$ is the final density of states and $\hat{H}_I$ is the interaction Hamiltonian operator for the photoelecteic absotprion which, at the first order, can be written as:

$$\hat{H}_I = i\hbar \frac{e}{m} \sum_j \vec{A}(\vec{r}_j) \cdot \vec{\nabla}_j \tag{2.6}$$

where $j$labels the electrons inside the atom and $\vec{\nabla}_j$ their linear momentum. By using equations **??** and 2.6, we find the probability of transition for the photoelectric absorption of photons belonging to a monochromatic, polarized and collimate beam:

$$W_{fi} = \frac{\pi\hbar e^2}{m^2} |A_0|^2 \left| \langle \psi_i | \sum_j e^{i\vec{k}\vec{r}_j} \hat{\eta} \cdot \vec{\nabla}_j \left| \psi_f \right\rangle \right|^2 \rho(E_f) \tag{2.7}$$

$\vec{k}$ and $\hat{\eta}$ are the electric field vector ($k = 2\pi/\lambda$)and the polarization unity vector. If we use the first order term of the series exapansion for the exponential, we obtain the transition probability in the dipole approximation (valid for $\left|\vec{k}\vec{r}_j\right| << 1$):

$$W_{fi} = \frac{\pi\hbar e^2}{m^2} |A_0|^2 \left| \langle \psi_i | \sum_j \hat{\eta} \cdot \vec{\nabla}_j \left| \psi_f \right\rangle \right|^2 \rho(E_f) \tag{2.8}$$

if we substitute the momentum with the position operator:

$$W_{fi} = \frac{\pi e^2}{\hbar m^2} |A_0|^2 \left| \langle \psi_i | \sum_j \hat{\eta} \cdot \vec{r}_j \left| \psi_f \right\rangle \right|^2 \rho(E_f) \tag{2.9}$$

In the dipole approximation the following selections rules are valid for the angular momentum:

$$\Delta l = \pm 1; \Delta s = 0; \Delta j \pm 1 = \Delta m = 0 \tag{2.10}$$

If the transition involves only one electron, the first rule implies that, in case of symmetry s (i.e. l=0) for the initial state, the final state has p symmetry (i.e. l=1). In order to calculate the transition probability of equation 2.9 and hence the absorption coefficient, it would be necessary to know the final state $\left|\psi_f\right\rangle$ (the initial state is simply the fundamental state of the absorbing atom). This is a priori difficult, since the

final state involves all the electrons in the atom and, furthermore, it is perturbed by the local environment of the absorber. An approximation used to simplify the situation is the single electron one, based on the fact that a large fraction $\mu_{el}(\omega)$ of the absorption coefficient is due to the transitions where only one electron modifies its state and the others $N-1$ just relax their orbitals to accomplish the new potential created by the presence of a core hole. The remaining fraction of μ is due to inelastic transitions, where the excitation of the primary core electron takes to the excitation of more external electrons, which can occupy higher energy states (shake up process) or leave the absorber atom (shake off process); the photon energy is in this case shared by all these excited electrons. The absorption coefficient, following this approximation, can be written

$$\mu(\omega) = \mu_{el}(\omega) + \mu_{anel}(\omega) \tag{2.11}$$

$$\mu_{el}(\omega) \propto \left| \left\langle \psi_i^{N-1} \psi_i \left| \hat{\eta} \vec{r}_j \right| \psi_f^{N-1} \psi_f \right\rangle \right|^2 \rho(\varepsilon_f) \tag{2.12}$$

where ψ^{N-1} is the Slater representation for the wave functions of passive electrons while ψ, $\vec{r}$ and ε_f are the wave function, position vector and final energy of the active electron. If the photoelectron has sufficiently high kinetic energy, it takes such a short time in leaving the absorber atom that its motion is not affected by the slower relaxation of the passive electrons [38]. In this case, we can separate the contributions of the active and passive electrons in the initial and final wave functions (sudden approximation):

$$\mu_{el}(\omega) \propto \left| \left\langle \psi_i \left| \hat{\eta} \vec{r}_j \right| \psi_f \right\rangle \right|^2 S_0^2 \rho(\varepsilon_f)\ S_0^2 \left| \left\langle \psi_i^{N-1} \psi_f^{N-1} \right\rangle \right|^2 \tag{2.13}$$

S_0^2 represents the overlap integral of the passive electrons wave functions in the initial and final states, The sudden approximation, which reduces the calculation of the final state to the final state for the only photoelectron, is rigorous starting form some tenth of eV above the edge. In general S_0^2 varies between 0.7 and 1, and can be experimentally determined measuring a standard compound with local enviroment similar to that of the sample under investigation, as done during this work. If there is no relaxation of the N-1 electrons, i.e. $S_0^2 = 1$, $\mu_{el}(\omega)$ in equation 2.13 has to be equal to $\mu(\omega)$ of equation 2.11: this means that S_0^2 measures the fraction of absorption due to the only elastic transitions. There is a theoretical separation of the local absorption coefficient $\mu(E)$ into a smooth embedded atom absorption $\mu_0(E)$ and an oscillating fine structure, which is conveniently described by the XAFS function:

$$\chi(E) = \frac{\mu(E) - \mu_0(E)}{\Delta\mu_0} \tag{2.14}$$

where $\mu_0(E)$ is the smooth atomic background absorption, which can be simulated by a spline, and $\Delta\mu_0$ is the jump in the absorption coefficient at the edge. Since in the Extended-XAFS (EXAFS) region (starting form about 30 eV above the edge) the final density of states varies slowly and monotonically with energy, the oscillations con-

tained in $\chi(E)$ come only form the matrix element. Different derivations for the single scattering XAFS formula have been proposed (see for example ref.[39]); they normally use Muffin Tin approximation for the atomic potential, i.e. radial inside a sphere surrounding each atom and constant between the atoms. Even if this approximation is

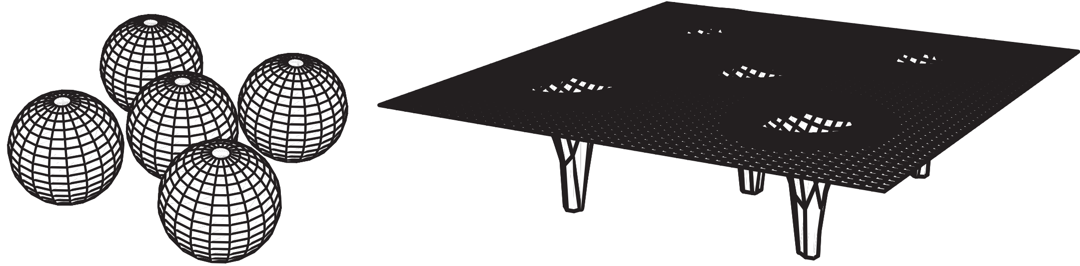

Figure 2.5: Muffin Tin potential.

quiet crude, it works well in the EXAFS region, where the high energetic photoelectrocn is essentially scattered by the inner part of the potential and moves almost freely in the interstitial region; the high energy makes it less sensitive to the potential details. If spherical photoelectron wave functions are employed, the single scattering XAFS formula, as a function of the photoelectron wave number $k = \sqrt{\frac{2m(E-E_0)}{\hbar^2}}$, is:

$$\chi(k,\Gamma) = Im\left(\frac{(N_\Gamma S_0^2)F_\Gamma(k)}{kR_\Gamma^2}e^{i(2kR_\Gamma+\Phi_\Gamma(k))}e^{-2\sigma_\Gamma^2k^2}e^{-2R_\Gamma/\lambda(k)}\right) \quad (2.15)$$

$$= \sum_\Gamma N_\Gamma A(k)\frac{|f_{eff_\Gamma}(\pi,k,R)|}{kR_\Gamma^2}sin(2kR_\Gamma + 2Re(\delta_\Gamma^c(k)) + \Phi_{eff_\Gamma}(k))e^{-2\sigma_\Gamma^2k^2}e^{-2R_\Gamma/\lambda_\Gamma(k)} \quad (2.16)$$

- $R_{0,\Gamma}$ nominal path lenght
- $f_{eff_\Gamma}(k)$ effective scattering amplitude
- $\Phi_\Gamma(k)$ effective scattering phase shift
- $\lambda(k)$ is the mean free path of the photoelectron;

The sum is performed over j-different atomic shells which contain each N_j identical neighbors; in the case of mixed shells, linear combinations have to be used. Rj is the vector which links the absorber to the j-neighbors, $|f_j(k,R_j)|$ is the modulus of the backscattering function of the atoms in the shell j, while $\phi_j(k,R_j)$ is the phase; in the spherical wave-approach they depend on R_j. $\delta_c(k)$ is the phase shift of the photoelectron wave induced by the central atom , this phase shift is counted twice (the

photoelectorn leaves the atom and come back after the scattering form the neighbors). $e^{-2k^2\sigma_j^2}$ is the Debye-Waller actor which measures the broadening of the distances distribution, σ_j^2 is the mean square fluctuation of the bond lengths R_j. If the distribution of the distances is gaussian (harmonic approximation), σ_j^2 can be expresses in terms of vibrational normal modes using the Debye's or Einstein's models [40]. $\lambda_j(k)$ measures the mean distance covered by the photoelectron before losing coherence with its initial state; it causes a damping in the XAFS amplitude since only photoelectrons which do not lose coherence with the initial state give a contribution to the signal. The relative lifetime is $\tau = \lambda/v$ where v is the speed of the photoelectron; the lifetime can be written as the sum of two contributions:

$$\frac{1}{\tau} = \frac{1}{\tau_h}\frac{1}{\tau_e} \tag{2.17}$$

The first is related to the core hole lifetime and diminishes with increasing atomic numbers, since the number of possible final states increases; this term is energy-independent. The second contributions is related to the photoelectron and is due to the inelastic interaction with electrons of the absorber neighbors; this term is energy-dependent. The product $\hat{\eta} \cdot \hat{R}_j$ between the polarization and the position unitary vectors takes into account the fact that the photoelectron is preferentially ejected in the direction of the field. For isotropic samples as polycrystalline powders, amorphous materials, or single crystals with a cubic symmetry this product can be substituted by the angular average 1/3. As far ad the photoelectron is sufficiently energetic and interacts only with the inner orbitals, we can consider the scattering centers as point-like and neglect the curvature of the spherical wave. As a consequence, the scattering process can be treated in the plane-wave formalism, the complex backscattering amplitude can be expanded in series of partial waves and does not depend on R_j any more:

$$f(k,\pi) = \frac{1}{k}\sum_{t=0}^{\infty}(-1)l(sl+1)e^{i\delta_l}sin\delta_l \tag{2.18}$$

δ_l are the phase shifts of the partal waves. In the isotropic and small atom approximation the single scattering XAFS formula becomes:

$$\chi(k) = -S_0^2(k)\sum_j \frac{N_j}{kR_j^2}\left|f_j(k,\pi)\right| sin(2kR_j + 2\delta_c(k) + \phi_j(k))e^{-2k^2\sigma_j^2}e^{-2R_j/\lambda_j(k)} \tag{2.19}$$

For non Gaussiam distances distribution, the XAFS formula can be written in series of cumulants C_k [41]; the odd cumulants determine the phase of the signal, while the even ones determine the amplitude. In the case the contribution to XAFS of the j-th atomic shell is:

$$\chi_j(k) = -\frac{S_0^2}{k}N_j\left|f_j(k,\pi)\right| exp(C_0 - 2k^2C_2 + \frac{2}{3}k^4C_4 ...)sin[2kC_1 - \frac{4}{3}k^3C_3 ... + \phi(k)] \tag{2.20}$$

In the formulation of the equation 2.19, relative to the Harmonic approximation, S_0^2 can be determined by measuring a standard compound, $|f_j(k,\pi)|$ and $2\delta_c(k)+\phi_j(k)$ can be either calculated *ab initio* or extracted from standard compounds with similar local environment; $\lambda_j(k)$ can be also estimated. As a consequence three quantities remain unknown and can be determined by fitting the experimental data: the number of atoms for each shell N_j, the distances R_j and the Debye-Waller factors.

Multiple scattering formalism

The limiting energy that divides XANES from EXAFS is by no means exactly defined since the transition from the one regime to the other is smooth: as $\hbar\omega$ is increased, the transition starts happening gradually. As a rule of thumb, near-edge structure ends approximately where the electron wavelength equals the distance from the absorbing atom to its nearest neighbors, which usually means about 4050 eV above the edge. In the XANES regime, the electrons kinetic energy is small and the scattering on the neighboring atoms tends to be strong for this reason.The simple expression of equation 2.19 is not valid any more and a multiple scattering has to be taken into account. The inclusion of multiple scattering (MS) contributions is mandatory in the XANES region, but also in the EXAFS one some of them have quite high amplitude and have to be included in order to analyze data. In particular, triangular paths involving a second neighbor atom and a first neighbor one result in some case important. Also longer collinear paths are in some case predicted to give quite high contribution due to the enhanced forward scattering caused by the intermediate atom. This phenomenon is referred to as *focusing* or *shadowing* effect [42].

The XAFS can be expanded in series of sums, each of ones accounts for all contributions of multiple scattering involving a definite number of atoms [43]:

$$\chi = \sum_{j=0} \chi_2^{0i0} + \sum_{i\neq j;i,j\neq=0} \chi_3^{0ij0} + \sum_{i\neq j\neq k;i,j,k\neq=0} \chi_4^{0ijk0} + \dots \tag{2.21}$$

In the sum, the term $\chi_\Gamma^{0ijk\dots0}$ represents the contribution to XAFS of the multiple scattering involving $\Gamma-1$ scatterers (labelled i,j,k, etc); the first sum stands for the single scattering. If an ad-hoc effective Debye-Waller factor is associated to each path Γ, togheter with a scattering amplitude f_Γ(including the damping due to the finite mean free path(, the XAFS function can be written in a form similar to that one of the single scatterig equation 2.19:

$$\chi_\Gamma(k) = -S_0^2(k)\sum_j \frac{N_\Gamma}{kR_\Gamma^2}|f_\Gamma(k,\pi)|\,sin(2kR_\Gamma+2\delta_c(k)+\phi_\Gamma(k))e^{-2k^2\sigma_\Gamma^2}e^{-2R_\Gamma/\lambda_\Gamma(k)} \tag{2.22}$$

The majority of these paths have usually a negligible amplitude and a preliminary estimation and filtering is necessary in order to select the useful ones for the fit procedure. The series expansion of equation 2.22 is rigorous in the EXAFS region, but unluckily cannot be applied very close to the edge (few tenth of ev), since the series is not convergent for very small k. In this case the problem has to be treated in am more gen-

eral way; for example by expressing the absorption cross section in terms of Green's functions. The Green's function for a system described by an hamiltonian H is:

$$G(E) = lim_{\xi \to 0^+} \frac{1}{E - H - i\xi} \tag{2.23}$$

The absorption cross section σ, proportional to the absorption coefficient μ, can be written in Rydberg unities ($e = \hbar = 1$) as:

$$\sigma = 16\pi^2 \alpha \hbar \omega Im \langle \psi_i | \hat{\eta}^* \cdot r' \frac{1}{\pi} G(Ei + \hbar\omega)(\hat{\eta} \cdot r) | \psi_i \rangle \tag{2.24}$$

where $|\psi_i\rangle$ is the single electron initial state, and G the "single particle" Green's function:

$$G(r, r', Ei + \hbar\omega) = \sum_f \int \prod_{i=1}^{N-1} d^3 r_i \prod_{i=1}^{N-1} d^3 r_i' \psi_i^{N-1^*}(\vec{r'}, \vec{r_1'}, ..., \vec{r_{N-1}'}) \tag{2.25}$$

$$\frac{\psi_f^{N^*}(\vec{r'}, \vec{r_1'}, ..., \vec{r_{N-1}'}) \psi_f^N(r, r_1, ..., r_{N-1})}{E_i + \hbar\omega - E_f - i\eta} \psi_i^{N-1}(\vec{r}, \vec{r}_1, ..., r_{\vec{N}-1}) \tag{2.26}$$

This function describes the propagation of the photoelectron in the final state energy Ef form point r to point r', the formalism takes into account the many body character of the process. The single particle Green fucntion satisfies the following Dyson's equation:

$$(\nabla^2 + E - V_c(\vec{r}))G(\vec{r}, \vec{r'}, E) - \int d^3 r'' \sum(\vec{r}, \vec{r''}, E) G(\vec{r''}, \vec{r'}, E) = \delta(\vec{r} - \vec{r'}) \tag{2.27}$$

$\sum(\vec{r}, \vec{r''}, E)$ is called self-energy and has a role of exchange-corelation potential which is, in the most general case, energy dependent and not local. $V_c(\vec{r})$ is the local Coulomb-Hartree potential due to the electrostatic interaction with nuclei and other electrons. A simplification often used in the calcualtion is the Muffin Tin symmetry for the potential; the Green function around a site n can be written as:

$$\frac{1}{\pi} G(\vec{r_n}, \vec{r_n'}, E) = \sum_{LL'} R_L^n(\vec{r_n}, E) \tau_{LL'}^{nn} R_{L'}^n(\vec{r_n'}, E) + \sum_L R_L^n(\vec{r_n}, E) S_L^n(\vec{r_n'}, E) \tag{2.28}$$

Here L is the couple of quantum numbers (l,m), R_L^n and S_L^n are the radial solutions, respectively regular and irregular at the origin (r_n=0), of the Schr$\ddot{o}$dinger equation for r_n, r_n' inside Muffin Tin sphere. The angular part is given by the spherical harmonics $Y_L(\vec{r_{ij}})$. These solutions link with continuity on the sphere surface with the combinations of Besse, Neumann and Hankel functions which are necessary to describe the wave function in the flat-potential region. $\tau_{LL'}^{nn}$ are the so called *scattering path operators* [44] and represent scattering by site n from an incoming wave L to an outgoing wave L'. These operators are defined by the Lippmann-Schwinger equation $G(E) = G_0 + GVG_0$ [45, 36, 46] where $H = H_0 + V$ is the hamiltonian of the system and by the transition matrix $TG_0 = VG(E)$, which is linked to the scattering path

operators by:

$$T = \sum_{i,j} \tau^{ij}_{LL'} \tag{2.29}$$

The *scattering path operators* can be written in function of the scattering matrix T_a and the propagators matrix G:

$$\tau^{ij}_{LL'} = [T_a^{-1} - G]^{-1} = [I - T_a G]^{-1} T_a \tag{2.30}$$

The scattering matrix describes the scattering amplitude of a spherical wave of angular momentum L into an outgoing wave of angular momentum L', due to the spherical symmetry of the potential the matrix is diagonal an the L indexes and it can be written by using the operator t^i_l, which depends on the atomic "phase shifts" δ^i_l [45, 36]:

$$T_a|^{ij}_{LL'} = t^i_l \delta_{ij} \delta_{LL'} = exp(i\delta^i_l) sin(\delta^i_l) \delta_{ij} \delta_{LL'} \tag{2.31}$$

As it can be inferred from this expression, the matrix is also diagonal on the site indexes. The propagator matrix G, as well diagonal on the site indexes, is defined by:

$$G^{ij}_{LL'} = 4\pi i \sum_{L''} i^{l+l''-l'} C^{L'}_{L,L''} h^+_{l''}(kr_{ij}) Y_{L''}(\hat{r_{ij}}) \tag{2.32}$$

where the Gaunt's coefficient $C^{L'}_{L,L''}$ are:

$$C^{L'}_{L,L''} = \int d\Omega Y_L(\theta,\phi) Y_{L'}(\theta,\phi) Y_{L''}(\theta,\phi) \tag{2.33}$$

while $h^+_{l''}(kr_{ij})$ are the spherical Hankel function. Due to the strong localization of $\langle\psi_i|$ on the photoabsorber site, for a K or L edge it is sufficient to calculate the Green function inside the photoabsorber sphere in order to evaluate the absorption cross section of equation 2.24; this means considering the only absorber site (n=0) in equation 2.28. The evaluation of the Green function on the absorber site, and so of the cross section, can be rigorously performed by numerically inverting the matrix $[I - T_a G]$ of equation 2.30; the inversion of this matrix can be generally done only through its knowledge n all the site and momentum indexes. For $k \to 0$ the Hankel's function module which enter the expression for G are in fact large and $[I - T_a G]$ has large out-of-diagonal elements, so that its inversion gives terms which couple the different atoms and structural configurations, and the only total signal makes sense. If the photoelectron energy is quite high, $T_a G$ can be treated as a perturbation of I and expanded in geometric series:

$$(I - T_a G)^{-1} = \sum_n (T_a G) \tag{2.34}$$

The series converges only if its spectral radius (the modulus of the biggest eigenvalue) is smaller than 1; this condition roughly fixes the limit of the validity of the series expansion representation, and it is normally satisfied staring form few tenth of eV of

all the scattering paths which start form the absorber and involve only one scatterer,the cubic term stands for paths involving scattering form two neighbors, etc. This could be demonstrate that, introducing the series expansion 2.34 in the expression of the scattering path operators, of the Green function and finally of the absorption coefficient, the XAFS function can be written in the multiple scattering form of equations 2.21, defining effective Debye-Wallers and backscattering amplitudes. A more complete and “step to Step” derivation of the general XAFS formulation in the multiple scattering approach can be found in references [43, 47, 48]. The numerical inversion of the matrix $(I - T_a G)$ gives the first method to simulate the XAFS signal in the near edge region; since in this way all the paths are implicitly summed by the inversion, this strategy is referred to as Full Multiple Scattering (FMS). The XANES of Y_2O_3, Lu_2O_3,Yb_2O_3 and SiO_2 samples at the Oxygen and metal edges which will be presented in the following have been simulated in FMS approach; this strategy allows to simulate XANES starting form the geometric configuration of a cluster of atoms surrounding the photoabsorber. The geometric structure of a site is deeply linked to the electronic structure of the material, as a matter of fact a completely different approach based on a band structure calculations could be adopted in order to reproduce XANES, at least in case of a periodic structure [49, 50]. Near the edge the absorption coefficient describes the transitions of the photoelectron to the lowest unoccupied states compatible with the selection rules for the angular momentum. In the case of a semiconductor these transition have, as final states, some unoccupied state in the bottom of the conduction band. If we consider a K-edge in the dipole approximation, the final state must have a p-symmetry; the XANES signal is in this way proportional to the p-projected local density of states in the bottom of the conduction band. The equivalence of the band structure calculation and the FMS approach has been demonstrated by [50].

2.1.4 XAS measurements

The simplest detection scheme for a XAFS measuremets is the transmission, where the X-ray flus impinging on the sample I_0 and the transmitted flux I of equation 2.1 are directly measured, using for example ionization chambers, and give the total absorption coefficient

$$\mu = -\frac{ln(I/I_0}{x} \tag{2.35}$$

In case of an uniform sample, the total absorption coefficient can be divided into the absorption of the atoms of interest and the other atoms $\mu_T = \mu_A + \mu_B$. In order to evaluate the signal to noise ratio, we have to consider that the structural information is carried by the only modulations of $\mu_A(\Delta\mu_A)$. If the expression of the signal to noise is maximized in function of the sample thickness we find $\mu_T X = 2.55$ and:

$$\frac{S}{N} = 0.736\frac{\Delta\mu_A}{\mu_T} I_{inc}^{1/2} \tag{2.36}$$

The signal to noise is maximized when the thickness of the sample is of the same order of magnitude of the photoelectron mean free path, typically about $10\mu m$. The higher ratio $\frac{\Delta\mu_A}{\mu_T}$, proportional to the concentration of the absorber, the better is the signal to noise. Transmission measurement are fast and accurate if concentrate, sufficiently thin and homogeneous samples are available. It is sometimes advantageous to make XAS measurements by indirect methods, rather than by measurements of incident and transmitted x-ray intensities. In the case of diluted samples, the detection of fluorescence radiation which origin from the relaxation of the exited state, becomes more favorable over transmission [51]. When the ore hole is filled by an electron from an higher energy level, the energy in excess, corresponding to the difference between the two electronic levels, can be delivered by the creation of a photon X (fluorescence photon) or by the expulsion of another electron from an higher energy level (Auger electron). The two processes are in competition: for light atoms the Auger effect is more probable, while for heavy atoms fluoresce emission becomes more likely. The relative weight of the two processes is measured by the fluorescence yield:

$$\eta_s = \frac{X_s}{X_s + A_s} \tag{2.37}$$

where X_s and A_s are the probability of emission of one fluorescence photon or Auger electron (see figure). The fluorescence photons corresponding to a particular eletronic

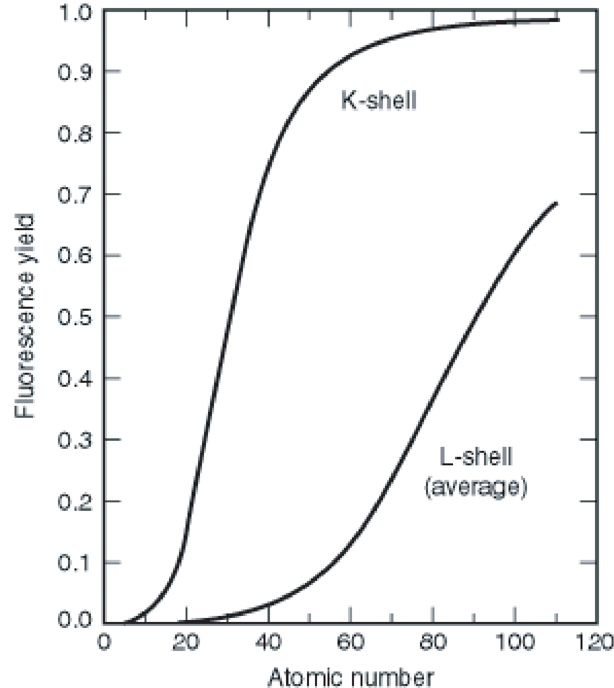

Figure 2.6: Fluorescence yields for K and L shells. The plotted curve for the L shell represents an average of L1, L2, and L3 effective yields (ref. X-Ray Data Booklet [52]).

transition taking place in the atoms of interest can be selected in energy by using an energy resolving detector (see figure 2.7) and give, upon definite conditions, a signal

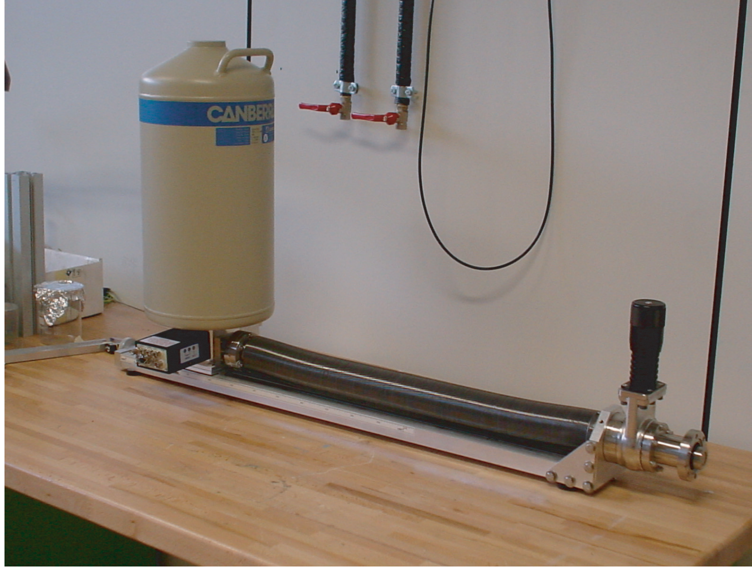

Figure 2.7: HPGe solid state detector.

that is proportional to the absorption coefficient. If a solid state detector is employed (see figure 2.7), the choice of an energy range is carried out electronically. For an infinite thick sample and an incidence angle of 45°, the intensity of fluorescence radiation on the detector with solid angle acceptance $\Omega/4\pi$ is:

$$I_f = \frac{I_0 \eta_s (\Omega/4\pi) \mu_A(E)}{\mu_T(E) + \mu_T(E_f)} \tag{2.38}$$

Here E is the energy of the incident photon and E_f is the characteristic fluorescence energy. If the element under investigation is dilute enough, the denominator in equation 2.38 does not sensibly oscillate as a function of energy and I_f is proportional to μ_A. An extension of equation 2.38 to the case of inhomogeneous samples and to the case in which the fluorescence of interest gives a very weak signal, comparable with background radiation, can be found in the paper of Lee *et al*. [39]. Fluorescence yield detection has been employed for the majority of the XAFS measurements of this thesis. A third possible strategy is given by the detection of Auger [53, 54] and secondary electrons [54, 55] (and interesting ref [56]); in this case the intensity of the electrons signal I_e is similar to that of fluorescence radiation:

$$I_f = \frac{I_0 (1 - \eta_s)(\Omega/4\pi) \mu_A(E)}{\mu_T(E) + n(E)} \tag{2.39}$$

n(E) is the exponential attenuation of the non-radiative signal, i.e. the inverse of the sampling depth for electrons. the total electron signal is dominated by that of sec-

ondary electrons which have typically energies of some eV and a mean free path not longer than 10nm. The short sampling depth of electrons makes non-radiative detection unfavorable with respect to fluorescence for thick samples; in case of very thin samples (a few nanometers) all depends an the solid angle acceptance for fluorescence(electron detectors and on the fluorescence/electron yield.

2.2 X-ray reflectivity

X-ray absorption spectroscopy can be made surface sensitive by using glancing angle geometry. For glancing angles of incidence, X-rays undergo total external reflection at the interface between air and a condensed medium and an evanescent(or exponentially damped) wave penetrates only $20-50$ Åinto the medium. A measure of the angle dependent reflectivity curve beyond the critical angle con provide information about the composition, the density and the smoothness of the reflectivity medium. On the other hand, from the energy dependence of either the reflected or the fluorescence signal, measured at a fixed glancing angle, the energy dependence of the absorption coefficient $\mu(E)$ of the medium can be obtained. The structural information carried by either signal is specific to the surface layer probed by the evanescent wave. The thickness of this layer is related to the selected glancing angle and can be changed by varying the latter around the critical angle. Glancing angle XAS has an important advantage over the more traditional surface science techniques, which detect electrons emitted from the surface, in that as X-rays are more penetrating than electrons, measurements can be carried out in real environments without the need of ultra-high vacuum.

2.2.1 reflEXAFS

Because the index of relfection of X-rays is lower than 1, the surface sensitivity can be obtained by working in grazing-incidence geometry. Infact, in the X-ray region the refraction index n has the form

$$n = 1 - \delta + i\beta \tag{2.40}$$

where δ nad β are of the order of $10^{-5} - 10^{-6}$ (james, 1962; Parrat, 1954). From Snell's formulae it is found that for grazing angles φ_c the incoming X-ray beam is totally reflected. The critical angle φ_c depends on the energy and on the electronic density of the material, and is found to be

$$\varphi_c = (2\delta)^{1/2} \cong 0.5 - 5mrad. \tag{2.41}$$

Below the critical angle the refracted beam propagates along the sample surface and the electric field decays exponentially into the sample. The depth $z_{1/e}$ at which the intensity of the refracted beam is reduced by 1/e is a funtion of the optical constants

and of the incident angle. $z_{1/e}$ is given by the following approximated formula,

$$z_{1/e} = \lambda / \left[4\pi (\varphi_c^2 - \varphi^2)^{1/2} \right], \tag{2.42}$$

which is valid to within 6 % for angles $\varphi_c < 0.85\varphi_c$. Typical values for $z_{1/e}$ are of the order af a few tens of $\AA$ Here will focus our attention on the X-ray absorption spectroscopy technique. The absorption coefficient μ is related to the imaginary part of the refraction index by

$$\mu = 4\pi\beta/\lambda \tag{2.43}$$

and β is related to δ via a Kramers-Kronig transformation (James, 1962). Also the fluorescence from the surface layer can be used as an indirect method to measure the absorption coefficient. This method, a valid alternative to the reflectivity measurement when working on diluted samples at very low incidence angles is also particularly effective in the study of thin films deposited on surfaces. In this case the fluorescence intensity I_f is given by

$$I_f = I_0 \mu_s z_s \varepsilon (\Omega/4\pi)(T/sin\varphi) \tag{2.44}$$

where I_0 is the intensity of the incoming beam (photons s^{-1}), μ_s and z_s are the sample absorption coefficient and thickness, respectively ($z_s << z_{1/e}$), ε is the fluorescence yield of the element selected and Ω is the solid angle collected by the detector.

Refl-EXAFS at GILDA beamline: experimental apparatus

Refle-XAFS experiments are carried out in dedicated vacuum chamber containing the sample holder and supporting the detectors for incoming beam normalization, sample reflectivity and fluorescence. These sketch on an apparatus for the collection of XAS spectra in total reflection mode is shown in fig2.8. The sample is mounted on a support that permits the vertical alignment as well as the rotation around an axis perpendicular to the beam. The beam is sized by one (or several) slits to a few tens of μm. The vertical size of the beam is actually the result of a trade off between beam intensity and sample size. The absorption coefficient can be measured by detecting the sample reflectivity (using an ion chamber or a photo diode on the reflected beam) or the sample fluorescence.

2.2.2 Absortpion measurements at Y, Lu, Yb, and Hf edges

Yttrium and Hafnium K-edges, Lutetium and Ytterbium L_{III}-edges XAS measurements were performed at the GILDA beam line $BM08$ of the European Synchrotron Radiation Facility in Grenoble, France. Cation absorption coefficients for all epilayers were collected in the fluorescence mode using a dynamically sagitally focusing Si(311) monochromator, and a 13-elements hyperpure Ge detector (see figure 2.8). Higher order harmonics were rejected by exploiting a pair of Palladium coated grazing incidence

Figure 2.8: Gilda end station at ESRF.

mirrors and detuning the crystals. Digital electronics was used to read the fluorescence detector using a $1\mu s$ peaking time, typical counting rates being in the order of $500c/s$ for the thinnest samples; in these conditions spectral distortions due to detector dead time are negligible. The energy spacing for the spectra was $0.5eV$ in the near-edge region and equivalent to less than 0.05 $\AA^{-1}$ in the EXAFS region. Due to the very limited thickness of this system, the samples were measured in the grazing incidence geometry (Refle-XAFS; see 2.2.1 and [57]) and the incidence angle on the samples was chosen to be $\phi = 0.1^{\circ}$, near the critical value $\phi_c = 0.13^{\circ}$ measured 200 eV above the edge. A $50\mu m$ input slit was used to define the beam for grazing incidence and in these conditions the photon flux on the sample was estimated to be $\approx 10^9 photons/sec$. The exploitation of parallel acquisition via thirteen detectors elemets allows to overcome the detection saturation problem by averaging the signals form the different elements after the exclusion of saturated channels. The rotating sample holder reduces smooths out the spurious peaks. The signal was normalized point by point by recording the flux incident on the sample with a ionization chamber filled with Argon gas.

2.2.3 Absortpion measurements at Oxygen K-edge

Oxygen K-edge measurements were performed at the BEAR beamline [58] of the ELETTRA facility in Trieste, Italy. The energy resolution was 200 meV for the XANES spectra and 350 meV for the EXAFS ones; the typical photon flux on the sample was of the order of $10^{10} photons/s$. Measurements on samples with thickness below $5nm$ were performed by recording the total electron yield drain current in order to enhance the surface sensitivity. Instead, fluorescence yield was used for the 20 nm sample in order to probe the full thickness of the epilayer; to this end a windowless hyperpure germanium detector was used. Samples were placed on a sample holder consisting of a steel plate mounted on a vertical rotary feedthrough. For the fluorescence measurements the sample was polarized at $+1000V$ in order to avoid electrons excited by the photon beam reaching the photodiode detector. The energy steps are reported in table 2.1 and the acquisition time was 1 s per point. In figure 2.9 a semplified CAD design of the BEAR's end station at ELETTRA is reported reported.

XAS region					
XANES (eV)	500-525	525-550	550-560	560-590	
step (eV)	0.5	0.1	0.25	1	
EXAFS (eV)	510-525	525-545	545-630	630-830	830-1050
step (eV)	5	0.5	1	2	3

Table 2.1: Energy regions for the measurements of spectra of O K-edge.

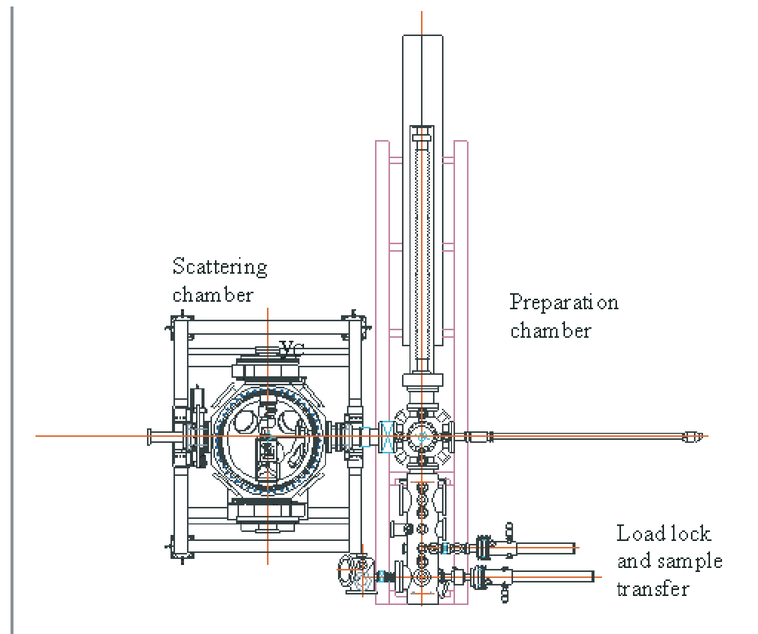

Figure 2.9: semplified CAD design of the BEAR's end station at ELETTRA

2.2.4 Data analysis

XAFS data analysis usually follows three steps: first the XAFS function is extracted from equation 2.14, then an evaluation of the backscattering amplitudes and phase shifts is done and finally a fit to the data varying some of the structural parameters in equation 2.19 is performed. The analysis software exploited in this work was the FEFF package, elaborated at the University of Washington, Seattle. For the background extraction the Athena package was exploited. This program first performs a pre-edge background removal using a linear function; in this procedure most of the energy dependence of the absorption other than that form the absorption edge of interest is eliminated . Then it carries out normalization to the edge jump and, finally, it performs a post-edge background removal . The last procedure consists in subtracting from $\mu(E)$ a smoothly varying background function $\mu_0(E)$, which approximates the absorption from the isolated embedded atom, obtaining in this way $\chi(E)$. he function exploited to approximate the post.edge background is a fourth-order polynomial spline whose knots are equally spaced in k space, the flexibility of the spline is determined by the number of knots. the spline and its first two derivatives are required to be continuous at the knots and one degree of freedom is associated to each knot; the background function is not required to go through the experimental curve at the knots. The basic idea of the program is that no signal in th Fourier transform of the EXAFS function $\chi(k)$ can have a physical meaning below a quite small threshold value of R, so the free coefficients of the spline are chosen in order to minimize the R components below a fixed R value R_{bkg}. This means that the method chooses the spline to best fit only the low-frequency components of $\mu(E)$, and not the whole absorption spectrum as other

codes use to do. The value of R_{bkg} can be chosen by the user, a good choice being about half the distance of the first shell peak, and determines the maximum number of knots i.e. thee stiffness of the spline. As a matter of fact, from information theory ideas [59] the number of independent points for an EXAFS fit is:

$$N_{ind} = \frac{2\Delta R\Delta k}{\pi} \tag{2.45}$$

where ΔR and Δk are the k- and R- range of useful data. If the fit is performed form R== to R=R_{bkg}, as in the case of the background removal, the number of independent points is:

$$N_{ind}^{bkg} = \frac{2R_{bkg}\Delta k}{\pi} \tag{2.46}$$

Snce each knot is associated with one degree of freedom, the maximum number of knots is the integer part of N_{ind}^{bkg} in the previous equation; the program uses a number of knots equal to $N_{ind}^{bkg} - 1$.

After background removal, all the atomic clusters which are useful for simulating EXAFS and multiple scattering signals are generated starting from the knowledge of their lattice parameters and spatial groups. This is done by the TkAtoms code, which produces a list of coordinates for all the atoms inside a cluster of chosen dimension [60]. For each cluster an *ab initio* modeling of the absorption cross section was done by exploiting the FEFF 820 code [47], which implements a Green function approach similar to that explained previously. For EXAFS analysis a Dirac-Fock atomic code [61, 30] was exploited to obtain free electronic densities, which were successively overlapped (following the Mattheiss's prescription [62]) in order to obtain a total electron density and to construct Coulomb potential. A ground -state Von Barth-Hedin potential [63] was exploited for exchange-correlation potential and the Hedin-Lundqvist (HL) energy-dependent self-energy correction was added [64]. Then the total potential was approximated with a Muffin Tin one, and the Dirac equation in the spinor relativistic approximation was solved to obtain radial wave functions and partial wave shifts, that are necessary to construct the single particle Green function of equation 2.28. Finally the Green function was calculated in the multiple scattering approach, paths with negligible amplitude were rejected and amplitude and phases for all paths inside a definite dlsuter were recorded in different files as a function of the energy. They have been used successively during the fitting procedure. The algorithm of the structural EXAFS analysis is represented by the flow diagram 2.10 FEFF and FEFFIT The code implements two further procedures, which are necessary for the simulation of XANES,and which have been exploited in this work: the full mltiple scattering approach (FMS) and a self consistent calcualtaion of the potentials. The first consists in the numerical inversion of the matrix of the previous ection; the time required for this inversion scales with the cube of the number of atoms in the cluster and the calculation is possible only bu using powerful computing resourses, for example the Xeon double-cpu 2.8 GHz Windows workstation belonging to Synchrotron Radiation group of the Department of Physics at the University of Bologna.

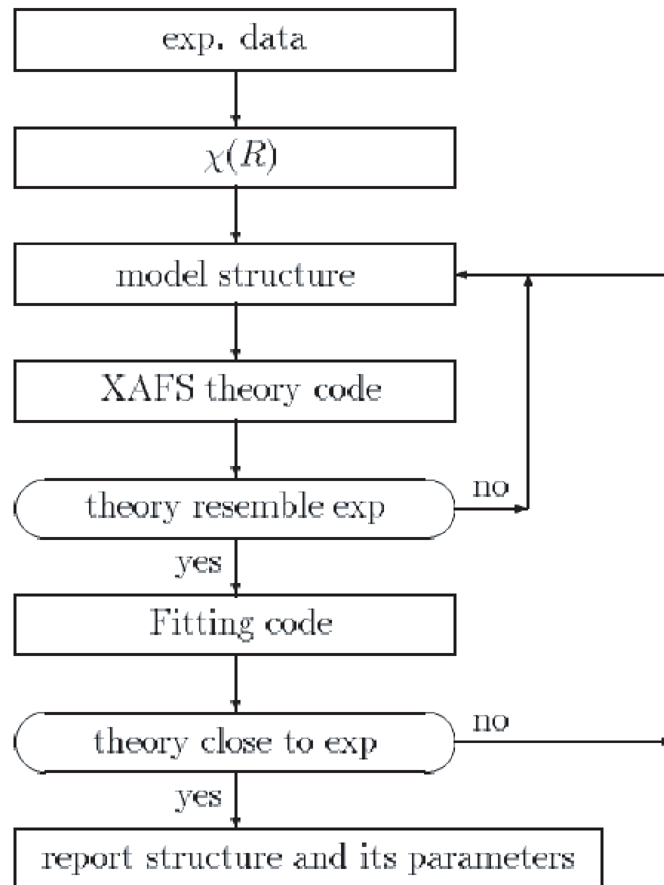

Figure 2.10: Flow diagram representing EXAFS data analysis.

Fourier filtering

The observed and calculated EXAFS are usually multiplied by a factor k^n to compensate for the rapid attenuation of the EXAFS with increasing k. The arbitrary exponent n is called the k-weighting and is typically 2 or 3. The Fourier transform of a k-weighted EXAFS spectrum is a complex function of the distance, and can be treated as a type of radial distribution function. If the phase function a(k) were uniformly 0, the magnitude of the Fourier transform would peak near the distances of the backscattering atoms. In practice, a 'phase' correction relating the peak positions to the true interatomic distances is required [](Lee et al., 1981). 19 The inverse transform of the Fourier transform is the original EXAFS. Noisy or otherwise unwanted parts of the EXAFS or its Fourier transform may be given lower weights ('filtered') by applying a window function prior to the forward or inverse Fourier transformation. Fourier filtering involves the following operations (see fig 2.11):

i) The original spectrum is multiplied by k^n.

ii) The k^n-weighted spectrum is multiplied by a window function.

iii) The windowed spectrum is Fourier transformed.

iv) The Fourier transform is multiplied by a window function.

v) The windowed Fourier transform is inverse Fourier transformed.

The Fourier-filtered EXAFS is given by the equation:

$$\chi_{filtered} = \mathbf{FT}^{-1}\left\{\Lambda_R \mathbf{FT}\left\{\Lambda_k \cdot k^n \cdot \chi_{original}\right\}\right\} \tag{2.47}$$

where **FT** is the Fourier transform

- $\mathbf{FT}^{-1}$ is the inverse Fourier transform
- n is the k-weighting
- Λ_k
- Λ_R

Fitting refinement algorithm

Feffit varies the structural parameters of the model so as to optimize the match between the calculated EXAFS χ_{calc} and the observed EXAFS cobs. The optimisation is achieved by minimising X^2_{exafs} which is defined as follows:

$$X^2_{exafs} = \int_{k=0}^{\infty} [w(\chi_{obs}(k) - \chi_{calc}(k))]^2 \, dk \tag{2.48}$$

where w is the weighting factor;

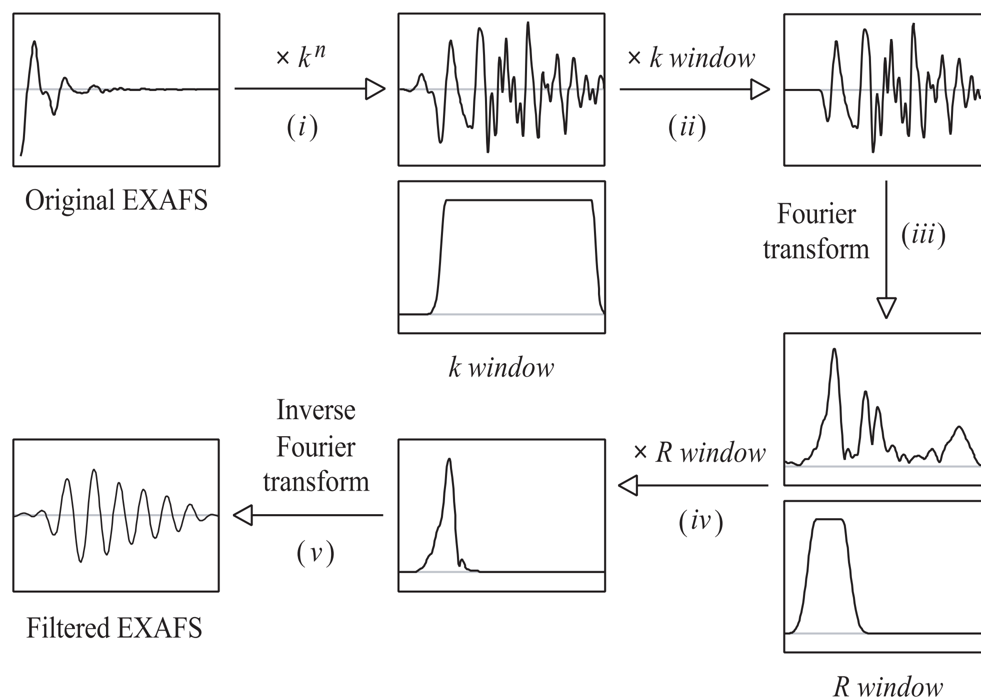

Figure 2.11: Fourier filtering of EXAFS data.

- $\chi_{obs}(k)$ is the filtered observed EXAFS curve; and
- $\chi_{calc}(k)$ is the filtered calculated EXAFS curve.

Most of the parameters, including the E_0 value, the filter parameters, the weighting factors as well as the model and empirical parameters, may be refined. The refinement uses the Levenberg-Marquardt method (Marquardt, 1963). The integral is calculated numerically.

2.3 photoelectron spectroscopy [1, 2, 3, 4]

Photoelectron spectroscopy is a general term which refers to all techniques based on the photoelectric effect. The energetic and the geometry of the photoemission project are sketched in the following figure. A beam of monochromatized radiation supplied by either a gas-discharge lamp or a synchrotron beamline is incident on a sample. As a result, electrons are emitted by photoelectric effect and escape into the vacuum in all directions.

By collecting the photoelectrons with an electron energy analyzer characterized by a finite acceptance angle, one measures the kinetic energy E_{kin} of the photoelectrons for a given emission angle. This way, the photoelectron momentum **p** is also completely determined: its modulus is given by

$$p = \sqrt{2mE_{kin}} \tag{2.49}$$

and its components parallel and perpendicular to the sample surface are obtained from the polar (ϑ) and azimuthal (φ) emission angles. Knowing the energy of the light $h\nu$ and the work function Φ we can determine the binding energy (E_B) for a given photoelectron considering the following equation:

$$E_k = h\nu - \Phi - |E_B| \tag{2.50}$$

The figures 2.12 below show the relation between the energy levels in a solid and the associated electron energy distribution obtained by photoemission.

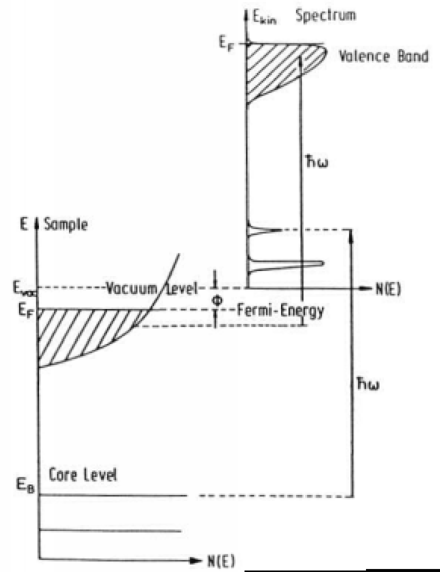

Figure 2.12: Relation between the energy levels in a solid and the associated electron energy distribution obtained by photoemission

Photoemission offers a direct method for the determination of the electronic energy levels, so one of its most direct applications is the chemical analysis. Other applications are, at higher energies (XPS): the study of the composition of multicomponent systems, chemical shift, films growing, and at lower energies (UPS): the study of adsorption processes, metal-insulator transitions, determination of density of states at the Fermi level. Below 2.13 there is a sketch of a typical Photoemission Beamline.

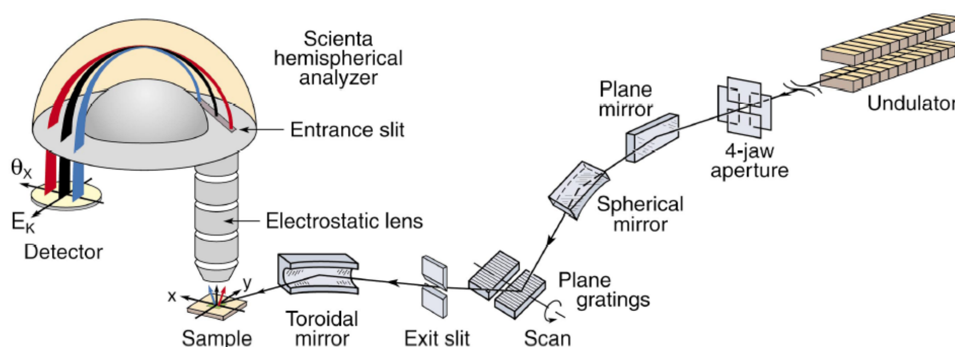

Figure 2.13:

The photo-excitation process

Photoemission represents the excitation of an electron from an initial state, below the Fermi level in the case of condensed matter systems, to a final state above the vacuum level. As illustrated in figure 2.12, the initial state may fall within the delocalized valence bands or it may represent a more localized core level.

A description of the interaction between the electron and the photon has been discussed in section 2.1.2.

Several models have been proposed to treat the photoemission process theoretically but two of them are definitively used.

Three step model

A phenomenological description that splits the process into three steps has been developed by Berglund and Spicer in 1964. In this approach, optical excitation between two Bloch states, are treated separately into three independent and sequential steps:

1. Optical excitation of the electron in the bulk.

2. Travel of the excited electron to the surface.

3. Escape of the photoelectron into vacuum.

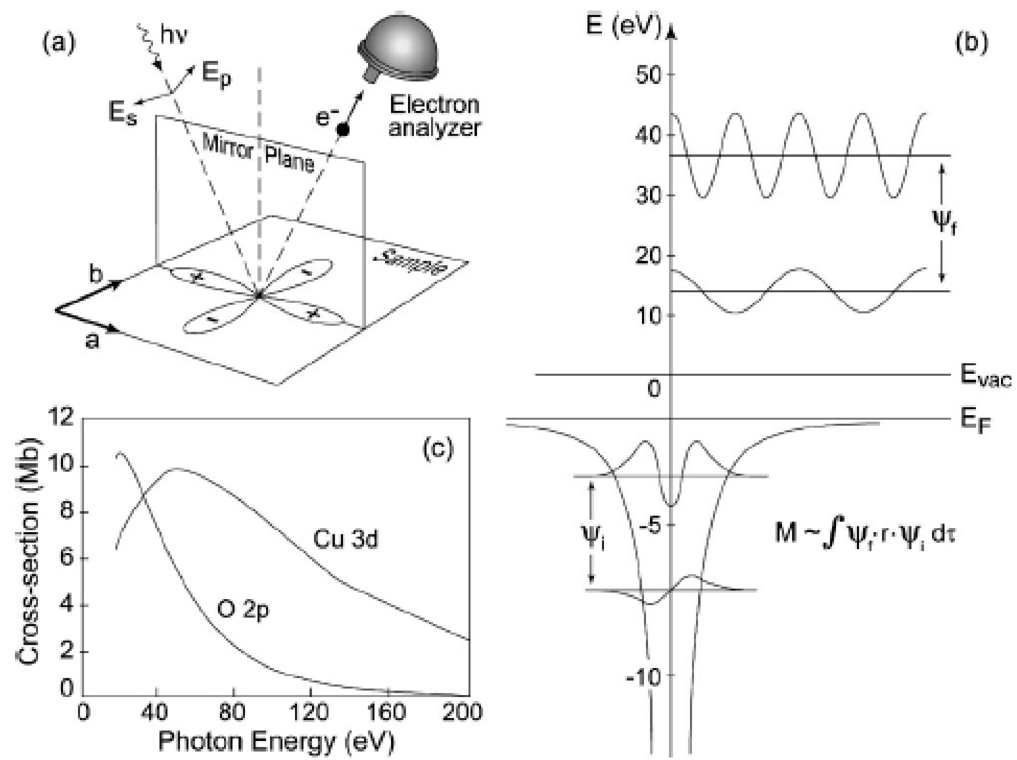

Figure 2.14:

The total photoemission intensity measured as a function of E_{kin} at a momentum **k**, namely

$$I(k, E_{kin}) = \sum_{f,i} w_{f,i} \tag{2.51}$$

is then given by the product of three independent terms: the total probability for the optical transition, the scattering probability for the travelling electrons, and the transmission probability through the surface potential barrier.

- *Step (i)* contains all the information about the intrinsic electronic structure of the material and it is related to w_{fi}; it would be convenient to factorize the wave functions in w_{fi} into photoelectron and (N-1)-electron terms. The problem simplifies within the *sudden approximation*, which is extensively used in many body calculations of photoemission spectra; In this limit, the photoemission process is assumed to be *sudden*, with no post-collisional interaction between the photoelectron and the system left behind (in other words, an electron is instantaneously removed and the effective potential of the system changes discontinuously at that instant). The sudden approximation is inappropriate for photoelectrons with low kinetic energy, which may need longer than the system response time to escape into vacuum. In this case, the so-called *adiabatic limit*, one can no longer factorize ${\Psi_f}^N$ into two independent parts and the detailed screening of photoelectron and photohole has to be taken into account.

- *Step (ii)* can be described in terms of an effective mean free path, proportional to the probability that the excited electron will reach the surface without scattering (i.e., with no change in energy and momentum). The inelastic-scattering processes, which determine the surface sensitivity of photoemission, also give rise to a continuous background in the spectra which is usually ignored or subtracted.

- *Step (iii)* is described by a transmission probability through the surface, which depends on the energy of the excited electron as well as the material work function ϕ.

one step model

A more rigorous approach is to proceed with the so-called one-step model in which photon absorption, electron removal, and electron detection are treated as a single coherent process. Excitation occurs between the initial one-electron Bloch state into a so called "time reversed LEED state" that is free electron like in vacuum and decays inside the crystal. In this case bulk, surface, and vacuum have to be included in the Hamiltonian describing the crystal, which implies that not only bulk states have to be considered, but also surface and evanescent states, as well as surface resonances. The two concepts are illustrated in the figure 2.15.

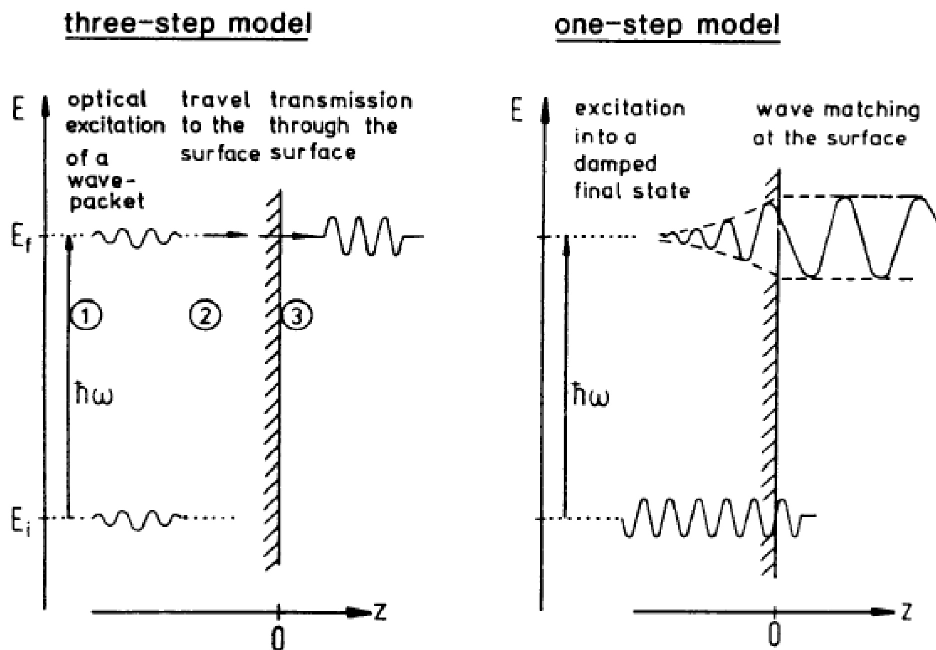

Figure 2.15:

Core level spectroscopy

While an excitation of valence band electrons may already by achieved by the light of gas discharge lamps, only synchrotron radiation sources offer a sufficient photon energy for the photoionizaton of subshell states. The application of soft x-ray radiation" ($200eV \leq h\nu \leq 700eV$) for a direct photoemission process allows the energy- and angle-resolved detection of core level electrons. In analogy to valence band photoemission techniques x-ray photoelectron spectroscopy (XPS) uses the kinetic energy of the photoexcited electrons to derive the binding energy of the initial electronic state which is directly related to the ionization energy of the appropriate atomic orbital. The measured photoelectron intensity $I(E_{kin}, h\nu, \vartheta, \varphi)$ may therefore be evaluated (1) for a determination of the chemical composition, (2) for an analysis of the atomic binding conditions, and (3) for a depth-profiling of the sample constituents in the surface-near region.

1. Due to its occupied atomic orbitals each atom exhibits different ionizable energy levels, which are reflected as element-specific peaks in the x-ray photoelectron spectrum. As these emissions, which are characterized by their binding energies, simply overlay each other in compounds or mixtures, *ESCA Electron Spectroscopy for Chemical Analysis* measurements allow the identification of all participating elements by determination of their atomic core level lines. If additional information concerning the cross section of the electronic transition, the

mean free path of the electrons and the spectrometer efficiency is provided, even a determination of the chemical stoichiometry is possible.

2. The exact peak position of core level emissions in XPS spectra are governed by the oxidation level of the emitting atom and the electric field generated by adjacent atoms. Generally, in case of a coordination with more electronegative ligands the core level electrons of a central atom appear at higher binding energy making them more difficult to excite. This so-called *chemical shift* may influence the energetic position of the emission peak up to 10 eV, which enables an identification of binding partners and a distinction of single or double covalent bonds. Therefore, high-resolution x-ray photoelectron spectroscopy is the preferred technique to trace chemical reactions or redox processes.

3. Keeping the sample orientation to the light source unchanged a variation of the detection angle ϑ in the XPS environment allows to tune the averaged information depth $z \propto cos(\vartheta)$ of the emitted photoelectrons. Using the analyzer angle ϑ as a parameter the peak ratio of elemental core level emissions mirrors an eventual concentration gradient perpendicular to the surface. From the statistical error and from the number of angular-dependent spectra a depth-resolved profile of the atomic distribution may be derived with defined accuracy. A suitable electron energy ensures a sufficient variation of the escape depth for different emission angles.

In summary these application options ensure the convenience of x-ray photoelectron spectroscopy for the chemical analysis of solid state surfaces. The width of a core line is determined by three factors:

1. the resolution of the photoemission spectrometer;

2. the presence of satellites that are not resolved;

3. the intrinsic lifetime width of the core hole.

2.3.1 Data analysis

Line shape

A range of physically possible line profiles in core-level XPS is possible, and simple Gaussian or Lorentzian functions are very rarely adequate. However recorded spectra exhibit deviations from idealized profiles due to a range of instrumental and physical effects:

- The response function of the electron analyzer (which may be asymmetric),

- The profile of the x-ray line-shape (predicted to be asymmetric for unmonochromatized metal anodes [1]),

- Intrinsic life-time broadening of the core-level hole state (usually assumed to be Lorentzian in nature),

- Phonon broadening,
- Differential surface charging of the sample.

In addition to these instrumental considerations the shape of a synthetic peak is also influenced by the choice of background algorithm used to remove, so called, extrinsic electrons from the data. If the photoemission is assumed to be a sudden switch-on process then Doniach-Sunjic [65] line shapes are used in the fitting model. A Doniach-Sunjic line shape is a combination of: (1) the Lorentzian width, G, which is the intrinsic shape of the photoemission peak dependent on life-time effects; (2) the Gaussian width, G, which is a convolution of the instrumental broadening (analyser and photon beam) and the electron-phonon scattering width; (3) the singularity index, α, which describes the energy dependent screening of the core-hole by conduction electrons. In dielectric photoemission ($\alpha = 0$) has to be modeled by Voigt-function peak shapes (i.e. the result of a convolution between Gaussian and Lorentzian line shapes). The Voigt functional form has been the basis for the quantitative analysis of XPS spectra in this thesis.

background removal

The background that is present in XPS spectra is due to the transport of electrons through a material after excitation by X-rays; this can be described by equations [66] that involve a one-sided convolution of the recorded data with an energy-loss probability distribution. This loss function offers a prescription by which electrons leaving the sample with an initial energy may have their characteristic energy altered by the interactions with the surface. The line-shapes described in the above paragraph are very dependant on the availability of background subtraction algorithms that complement their use. If a background is incorrectly removed from a spectrum then the merit of attempting to model the result with theoretically correct synthetic line-shape is less clear. Shirley background [67, 68] was used to remove as much asymmetry as possible from recorded data

The fitting program

XPS data analysis was performed by using CasaXPS program. The output of this program reveals parameters such as: energy positions; peak areas; peak widths and heights.

Chapter 3

Sample growth

3.1 Sample Growth of Y_2O_3/Si(100)

The Y_2O_3/Si(100) samples investigated in this section have been grown by Prof. Dimoulas's group at the Institute of Materials Science, National Center for Scientific Research DEMOKRITOS, Athens, Greece.

3.1.1 Film growth [5]

Y_2O_3 layers were grown on 2 in. p-type Si(001) wafers; The substrates used were semi-insulating with a resistivity of 8000 $V \times cm$. Growth was performed in an UHV chamber with base pressure ($\approx 2 \times 10^{-10} Torr$), equipped with a three-pocket electron gun and high-temperature effusion cells optimized for MBE growth of Si and Si-based semiconductor alloys. Prior to growth, the silicon substrates were heated up to 770 °Cin the MBE chamber under a weak Si flux of 0.05 $\text{Å}/sec$ in order to desorb the native oxide. The procedure was monitored by RHEED and in all samples a (2×1) reconstruction was observed, indicating a clean silicon surface. The small Si flux favors the formation of silicon suboxides. The Si buffer was grown at 650 °Cat a rate of 0.3 Å/s using electron-beam evaporation. After desorption, the substrates were cooled down to 450 °C, which was the growth temperature for all samples. Y_2O_3 was evaporated by means of an electron gun from a sintered ceramic target. The oxide growth rate was ≈ 0.4 $\text{Å}/s$ for all films. Five samples with thicknesses ranging from 2 to 20 nm were deposited and studied; some samples were subsequently annealed *in situ* for 30 min at 500 °C. In Table 4.1 the characteristics of the samples are listed. *In situ* monitoring by RHEED showed that Y_2O_3 grows on Si with orientation Y_2O_3(110) //Si (001) with two domains rotated by 90° with respect to one another, as previously established [69]. HRXRD analysis performed on as-grown and annealed epilayers confirmed the RHEED results are in agreement with previous results. The out-of-plane lattice parameter and the mosaicity were found not to be influenced by the annealing. The structure grown had the form Y_2O_3 /(20 nm) undoped Si buffer/Si (001) substrate. It should be emphasized that O_2 gas was not introduced in the chamber during growth in an attempt to minimize (or avoid) the oxidation of Si. When the growth temperature

is 450 °C, the Y_2O_3 diffraction pattern (Fig. 3.3) consists of a single strong peak.

3.1.2 Structural characterization of $Y_2O_3/Si(100)$

The structural quality of the epilayer and the interface were characterized by x-ray diffraction and cross-sectional and plan-view HRTEM using a Philips CM20 200 kV machine. The $\theta - 2\theta$ x-ray diffraction data is shown in Figs. 3.3. $\theta - 2\theta$ x-ray diffraction data for sample grown at different temperatures are also shown (3.1,3.2,3.4. In these spectra the Y_2O_3 diffraction pattern is superimposed on that of Si. Films grown at low temperature (280 °C) typically exhibit weak (222) diffraction peaks as shown in Fig. 3.1, indicating that the material grows in such a way that the (111) lattice planes of Y_2O_3 are parallel to the (001) planes of Si. At slightly higher temperature ($T_g = 320$ °C) growth develops in such a way that two different orientations, Y_2O_3 (111)//Si (001) and Y_2O_3 (110)//Si (001) coexist in the same film as shown in Fig. 3.2. When the growth temperature is increased to (450 °C), the (222) diffraction peak disappears. In this case, the Y_2O_3 diffraction pattern (Fig. 3.3) consists of a single strong peak (440),

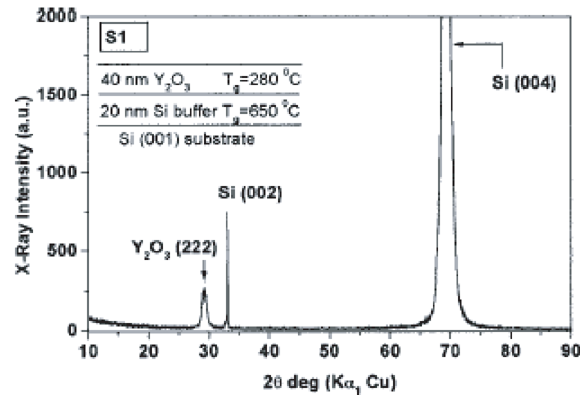

Figure 3.1: X-ray $\theta - 2\theta$ scan for sample S1 grown at 280 °C. The (111) planes of the Y_2O_3 epilayer are parallel to the (001) planes of the Si substrate.

indicating that single crystalline material is grown such that the (110) planes are preferentially oriented parallel to the (001) planes of Si substrate. This represents the case studied in this work. Infact on the basis of x-ray data, it could be inferred that an optimum temperature for the growth of good epitaxial quality crystalline Y_2O_3 on Si (001) is around 450 °C. In a film grown at 610 °C(Fig. 3.4), the Y_2O_3(440) peak intensity is significantly decreased compared to the corresponding one of sample S3 in Fig. 3.3. Additional weak peaks are observed (Fig. 3.4), corresponding to (100) and higher order diffraction from hexagonal YSi_2 epitaxially formed with the c axis laying on a plane parallel to the substrate. It is characteristic that the Y_2O_3 (001) diffraction peak does not appear in any of the four spectra indicating that cube-on-cube epitaxy of Y_2O_3 (001) on Si (001) is not favored despite the fact that $a_{Y_2O_3} \approx 2a_{Si}$. Film S3, which appears to be of very good quality on the basis of x-ray data (Fig. 3.3) is more thoroughly examined by TEM. Bright field image micrographs and a diffraction pattern from cross-sectional Si (110) TEM are shown in Figs. 3.5,3.6,3.7.

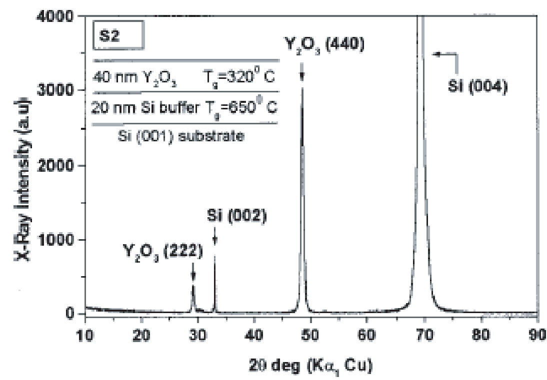

Figure 3.2: X-ray $\theta - 2\theta$ scan for sample S2 grown at 320 °C. Two different crystallographic orientations coexist in the same film.

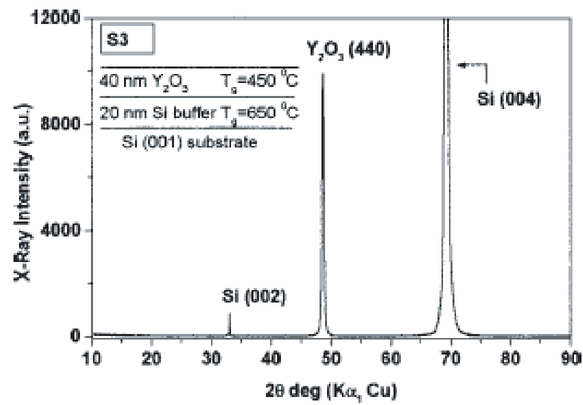

Figure 3.3: X-ray $\theta - 2\theta$ scan for sample S3 grown at 450 °C. The single strong diffraction peak (440) indicates good crystalline quality heteroepitaxial material such that Y_2O_3 (110)//Si (001).

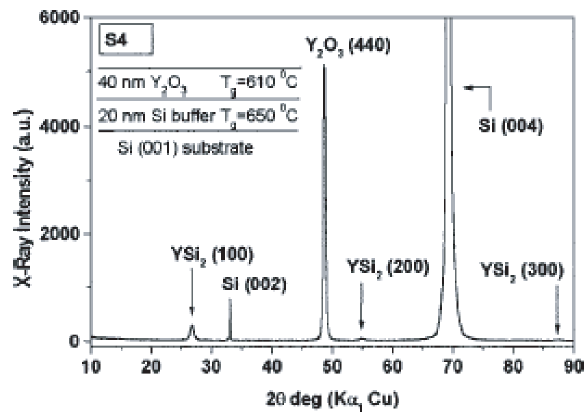

Figure 3.4: X-ray $\theta - 2\theta$ scan for sample S4 grown at 610 °C. In addition to Y_2O_3 (440), weak YSi_2 (100) and higher order diffraction peaks appear, corresponding to a hexagonal phase with the *c* axis parallel to the surface. This could be evidence of a reaction between the epilayer and the Si substrate.

The diffraction pattern in the same figure consists of Y_2O_3 peaks (weaker spots), superimposed on the well-known pattern of Si ($\overline{1}\overline{1}0$) represented by the stronger intensity spots. The Y_2O_3 diffraction pattern (Fig. 3.5(a)) in combination with the real image indicates that thin film material of very good crystalline quality is obtained, although a microstructure consisting of two domains with different crystallographic directions is present in the film. Both domains contribute (see overlapping spots in Fig. 3.5(b)) to the strong Y_2O_3 (440) and the rest (weaker) peaks of the same family. These are aligned along the Si (001) crystallographic direction indicating perfect heteroepitaxial growth in such a way that Y_2O_3 (110) planes are parallel to Si (001) ones in agreement with the x-ray data of Fig. 3.3. The implications made above with regard to the existence of a microstructure are confirmed by the highresolution real image of Fig. 3.6(a) where two different crystallographic domains marked by A and B can be seen. The images in figure 3.6(b) show the crystal orientations of the epilayer (with respect to that of the Si substrate) which correspond to the observed domain images [70]. In A, the family of planes perpendicular to the Y_2O_3 (110) crystallographic direction are imaged, which is consistent with the appearance of corresponding peaks such as the Y_2O_3 (222) close to Si (111) and the Y_2O_3 (004) in the diffraction pattern (see Figs. 3.5(a) and 3.5(b)). In domain B, which can be generated from A by a 90 rotation through an axis perpendicular to the surface, an image of the family of planes perpendicular to Y_2O_3 (100) and (010) crystallographic directions is obtained. In summary, the two crystallographic domains observed have Y_2O_3 (001)//Si ($1\overline{1}0$) (domain A) and Y_2O_3 (001)//Si (110) (domain B), while both have Y_2O_3 (110)//Si (001). The domains extend from the interface to the top of the films and have lateral sizes in excess of 100 nm as, for example, in the case of domain B in Fig. 3.6(a). The domain boundaries are not clearly defined since there is always a transition region between them. A magnification of the high-resolution image is shown in Fig. 3.7. An amorphous materials phase is present at the Y_2O_3 /Si interface, which forms a nonuniform layer with thick-

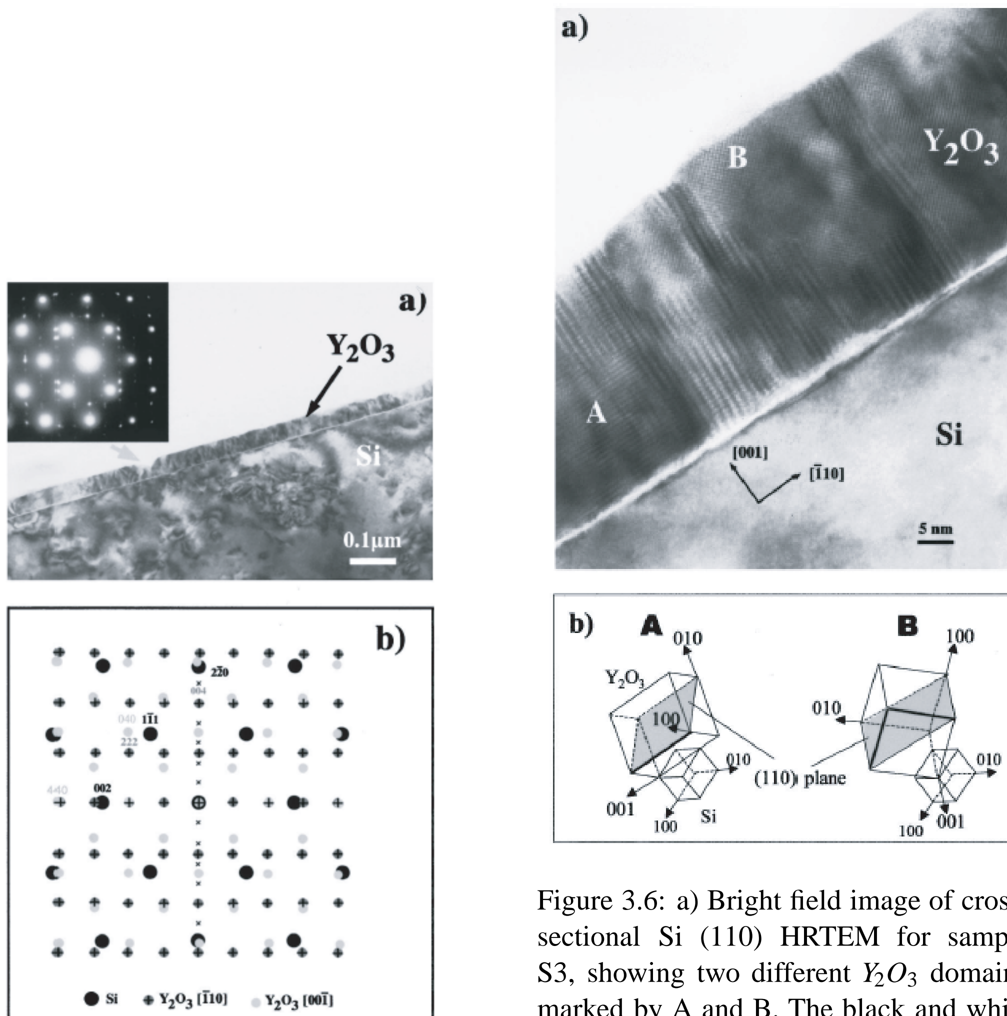

Figure 3.5: a) Bright field image of cross-sectional Si (110) TEM for sample S3. The gray arrow shows the point where Y_2O_3 material is missing. The inset shows the Y_2O_3 diffraction pattern weaker spots superimposed on the one for Si spots of stronger intensity. b) A superposition of the calculated diffraction patterns Y_2O_3 (110) and Y_2O_3 (001) is used to simulate the observed diffraction pattern (inset in a). Miller indices are used to assign a set of high intensity spots observed in the diffraction pattern.

Figure 3.6: a) Bright field image of cross-sectional Si (110) HRTEM for sample S3, showing two different Y_2O_3 domains marked by A and B. The black and white contrast represents a superstructure with period ;13.2 Å. b) Schematic drawings of the Y_2O_3 crystal orientations with respect to the Si substrate, which are consistent with the real image observations of domains A (Y_2O_3 001//Si (110) and B (Y_2O_3 001//Si (110). The schematic shows that the two domains are rotated between each other by 90° through an axis perpendicular to the surface, both having the Y_2O_3 (110) family of lattice planes parallel to the Si (001) surface. The heavy lines indicate the planes in cross section that are best imaged in a).

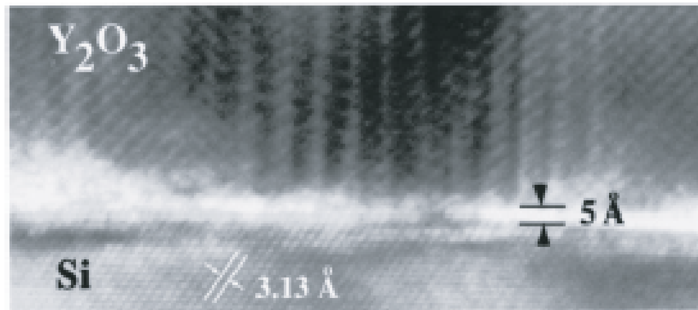

Figure 3.7: Magnified high-resolution image of cross-sectional Si 110! TEM showing that an amorphous materials phase is present at the interface.

ness varying in the range between 5 and 15 Å. Although such an interface layer could be *YSiO* silicate, previous work [71] has suggested that it is SiO_2 . This cannot be residue of native SiO_2 due to incomplete substrate surface treatment since the Y_2O_3 is grown directly on the Si buffer, which was deposited in situ without breaking vacuum. It should be noted that despite the presence of the amorphous layer at the interface, the Y_2O_3 film has a good epitaxial single crystalline quality. This could be explained by assuming that, during the initial stages, direct epitaxy of pure Y_2O_3 on silicon takes place, while the amorphous phase is formed later during growth due to an enhanced diffusivity of oxygen, which reaches the interface and reacts with Si.

3.2 Introduction to Atomic Layer Deposition (ALD)

Assembling thin films atom by atom allows very high control over their composition and structure. One such technique is atomic layer deposition (ALD; also called atomic layer epitaxy), in which a vapor reacts with a surface until a monolayer has been chemisorbed. Atomic layer epitaxy (ALD) [72, 73, 74] is a special modification of the chemical vapor deposition technique for depositing thin films and related surface structures. In ALD the reactant vapors are pulsed onto the substrate alternately one at a time, and between the reactant pulses the reactor is purged with an inert gas (N_2 for example). With a proper adjustment of the experimental conditions all the process steps are saturative, i.e. the precursors (see for example a Lu metal precursor in fig 3.8)exposed on the surface chemisorb on it or react with the surface groups saturatively forming a tightly bound monolayer on the surface, and the subsequent purging step removes all the excess molecules from the reactor chamber. When the next precursor is dosed in, it will thus encounter only the surface monolayer with which it reacts, producing the desired solid product and gaseous by-products. Under such conditions the film growth is self-limiting, since the amount of solid deposited during one cycle is dictated by the amount of precursor molecules in the saturatively formed surface monolayer. the self-limiting film growth mechanism which gives it a number of

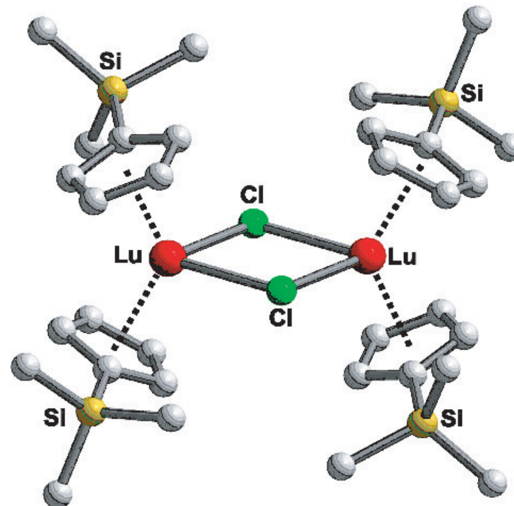

Figure 3.8:

attractive properties, like accurate and simple film thickness control, sharp interfaces, uniformity over large areas, excellent conformality, good reproducibility, multilayer processing capability, and high film qualities at relatively low temperatures [75]. The advantageous consequences of the self-limiting growth mechanism are summarized in figure 3.9.

3.2.1 Example of an ALD deposition process.

The principle of atomic layer deposition (ALD) is drawn in the pictures below. The initial situation is a substrate on which the new layer will be deposited. The substrate has a certain surface termination of atomic bonds (-O-H), which is stable in an inert gas ambient like nitrogen (N_2) for example.

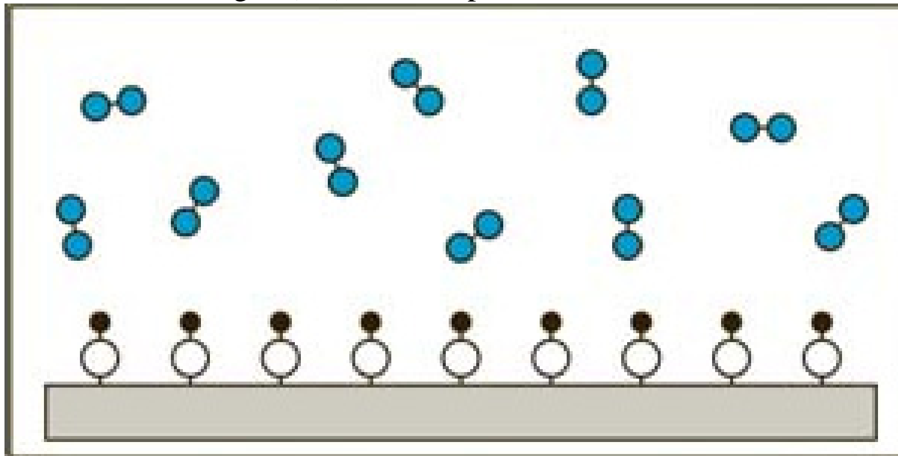

In the first step of the process, a vapor of the first chemical reactant (precursor) is let into the reaction chamber. This precursor can be a small or large molecule, but will

Characteristic feature of ALE	Inherent implication for lm deposition	Practical advantage
Self-limiting growth process	Film thickness is dependent only on the number of deposition cycles	Accurate and simple thickness control
	No need for reactant ux homogeneity	Large-area capability Large-batch capability Excellent conformality No problems with inconstant vaporization rates of solid precursors Good reproducibility Straightforward scale-up
	Atomic level control of material composition	Capability to produce sharp interfaces and superlattices Possibility to interface modi cation
Separate dosing of reactants	No gas phase reactions	Favours precursors highly reactive towards each other, thus enabling effective material utilization
	Suf cient time is provided to complete each reaction step	High-quality materials are obtained at low processing temperatures
Processing temperature windows are often wide	Processing conditions of different materials are readily matched	Capability to prepare multilayer structures in a continuous process

Figure 3.9:

eventually contribute a single type of atom to the layer. An example is aluminumchloride ($AlCl_3$), which will only leave the aluminum atom in the final layer.

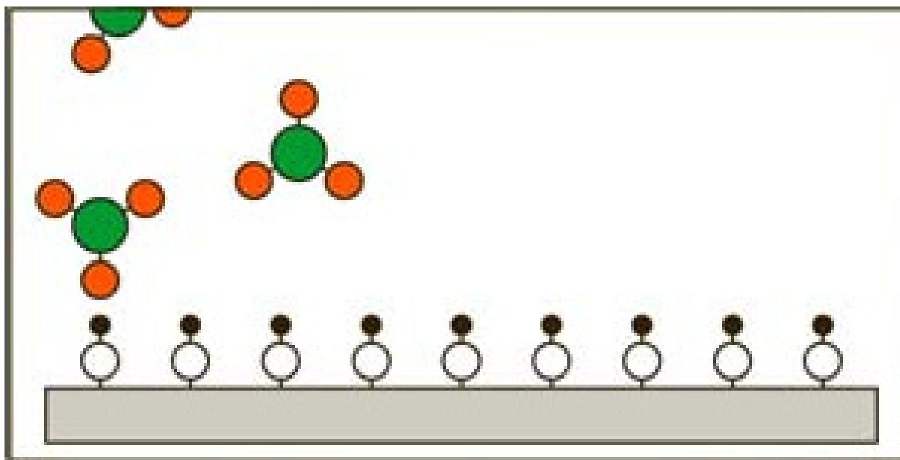

The precursor molecules will react with the surface of the substrate. To continue the example of $AlCl_3$, the following chemical reaction will occur:

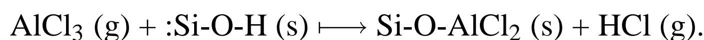

$AlCl_3$ (g) + :Si-O-H (s) $\longmapsto$ Si-O-$AlCl_2$ (s) + HCl (g).

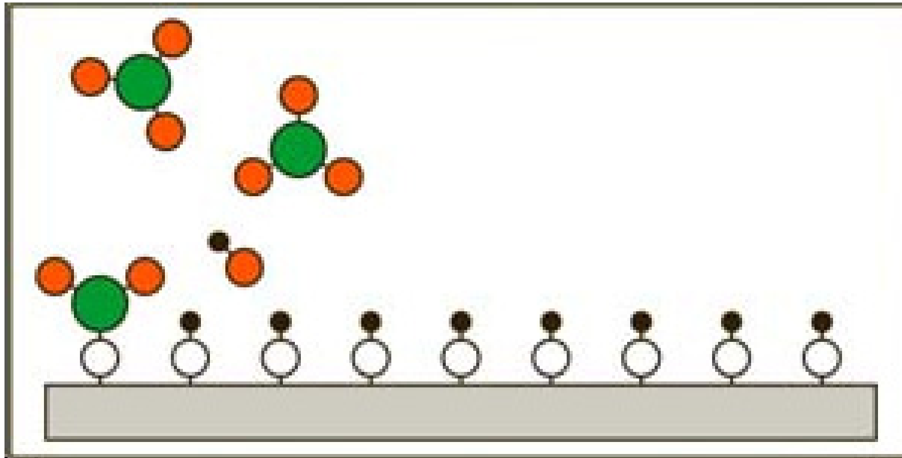

This reaction is chosen to be self-limited by saturation of the surface. The result is a single layer of molecules of the first precursor attached to the surface.

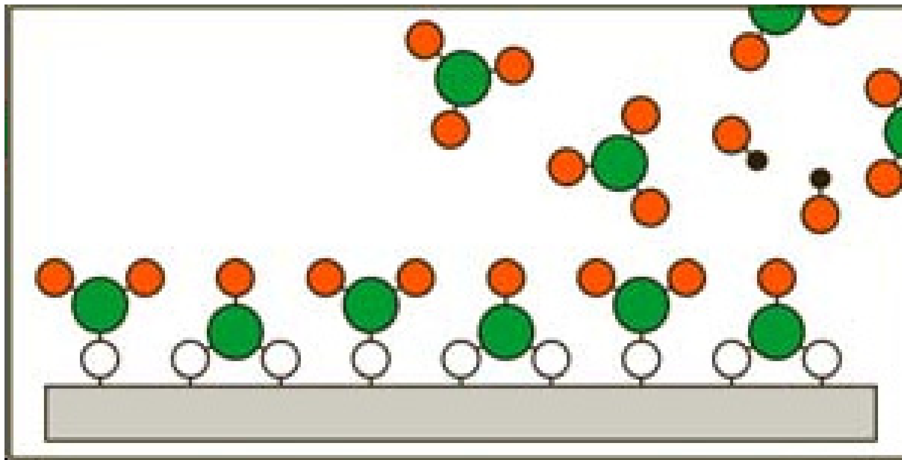

A purge step with an inert gas will remove the unreacted part of the first precursor from the system, to avoid gas phase reactions between the first and the second precursor.

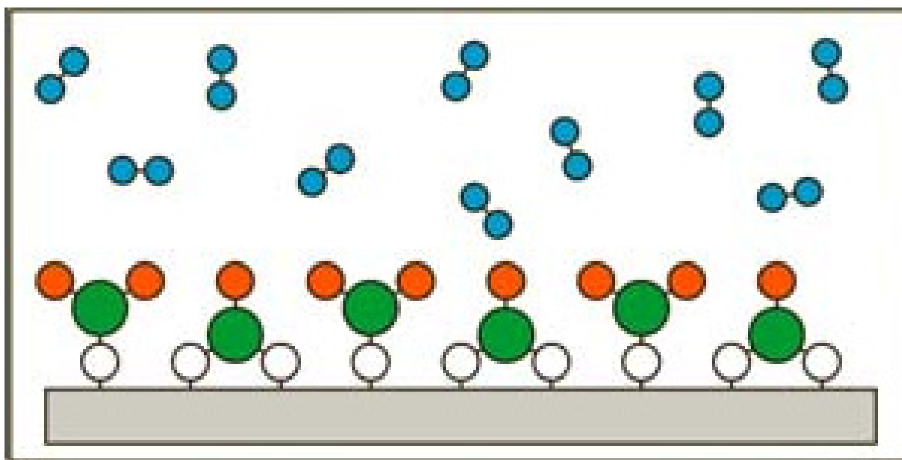

A second reactant vapor is used to react with the surface of the first layer. In this example water vapor (H_2O) is used to remove the cloride atoms from the surface and prepare the surface for repetition of the two reaction steps. The water vapor will react

according to:

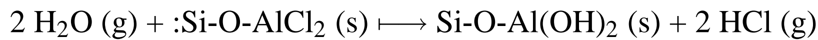

$$2\,H_2O\,(g) + {:}Si\text{-}O\text{-}AlCl_2\,(s) \longmapsto Si\text{-}O\text{-}Al(OH)_2\,(s) + 2\,HCl\,(g)$$

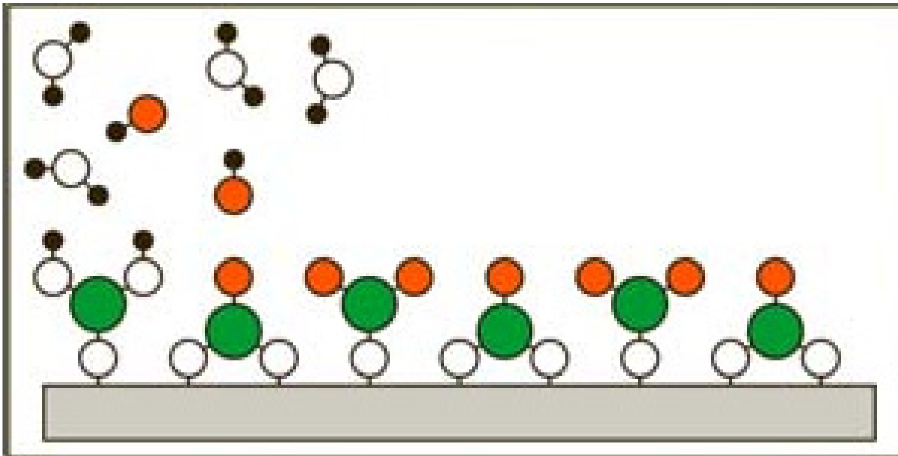

The second reaction will continue until the surface is saturated. The result is a monolayer of a material consisting of two elements (in this case aluminum and oxide). A second purge step with nitrogen gas will remove the remaining water vapor.

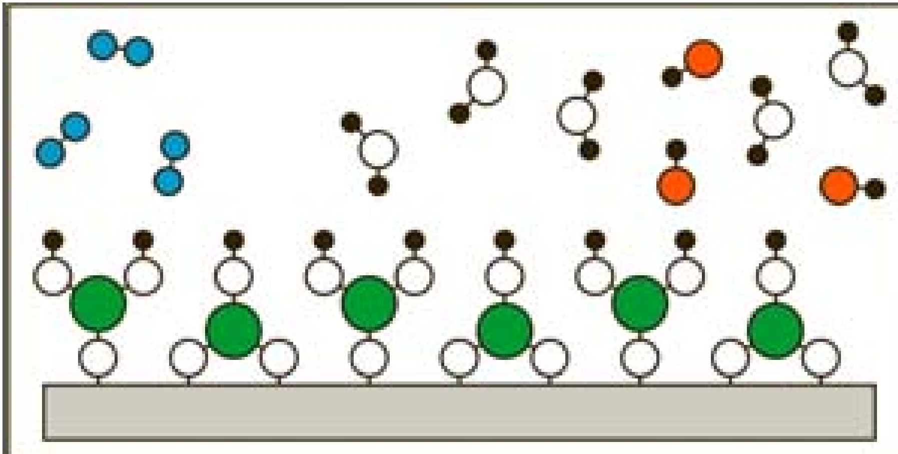

The system is now ready to repeat the deposition with a reaction of the first precursor with the surface. The required thickness is achieved by repeating the reaction steps with both precursors, separated by N_2 purge steps.

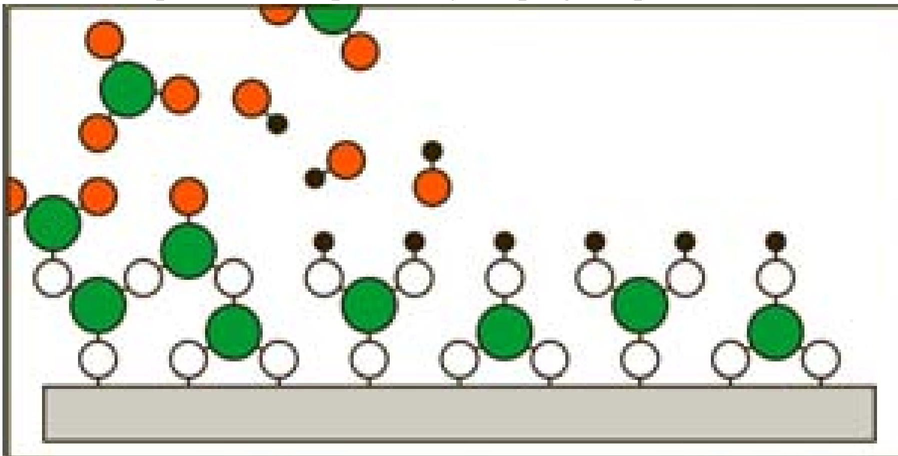

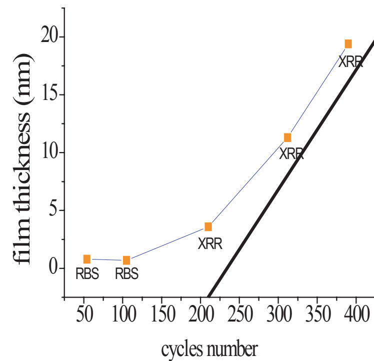

Figure 3.10: Prima figura

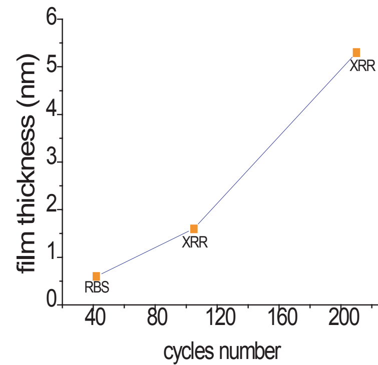

Figure 3.11: Seconda figura

In reality, several problems change the result from the ideal situation. Besides the intended chemical reaction, other reactions may occur at the same time. The reaction of a precursor may not saturate the complete substrate in time, or the precursor molecule is too large to enable reactions with all available bonding sites. Other problems include re-evaporation from the surface or condensation of the precursor gas.
ALD offers a number of other remarkable capabilities in addition to the control of stoichiometry at an atomic level. The thickness of a film can be set digitally by counting the number of reaction cycles and is substantially immune to variations caused by nonuniform distribution of vapor or temperature in the reaction zone. In fig 3.10 and 3.11 are reported typical examples of the film thickness versus the number of ALD cycles (in this case Yb_2O_3 films grown using the $Yb(C_5H_5)$ Yb precursor and H_2O and O_3 oxygen precursors); the thickness was measured using x-ray reflectivity (XRR) and Rutherford back-scattering (RBS) for the thicker and thinner films, respectively. The growth rates (γ) were consequently estimated. The ALD Lu_2O_3, Yb_2O_3 films are very smooth according to atomic force microscopy (AFM): root mean square roughness between 0.2-0.3 nm in the thickness range between 2-11 nm.

3.2.2 ALD deposition of Lu_2O_3 and Yb_2O_3 films on Si (100).

Si substrate preparation

Prior to deposition, the Si(100) substrates were covered with a thin chemical oxide layer (RCA for 10 min at 85 °C($HCl : H_2O_2 : H_2O$ (1:1:5)), dip for 30 s in a diluted HF solution $(HF : H2O(1:50))$ at room temperature, and RCA again for 10 min at 85 °C). In the $Hf-last$ samples the substrate was H-terminated Si(100) (RCA for 10 min at 85 °C, and dip for 30 s in a diluted HF solution). A 1 min long rinse in deionized water followed each cleaning step.

Film growth.

A set of Lu_2O_3 and Yb_2O_3 films were deposited using a F-120 ASM Microchemistry reactor on Si(100) at the growth temperature of 360 C. The Lu_2O_3 films were deposited alternating injections of the newly synthesized complex $[(\eta^5 - C_5H_4SiMe_3)2LuCl]_2$

	Lu_2O_3	Yb_2O_3:
metal source	$[\eta^5C_5H_4(SiMe_3)]2LuCl_2$	$Yb(C_5H_5)3$
metal source temperature	190 195 °C	100 °C
Oxygen source	H_2O	H_2O and O_3
Growth temperature	360 °C	360 °C
Carrier and purge gas	N_2	N_2
Growth rate	0.1 nm/cycle	0.036 nm/cycle using H_2O 0.026 nm/cycle using O_3

Table 3.1: Growth parameters of Lu_2O_3 and Yb_2O_3 films.

(see fig 3.8) (11 s) as Lu source, [76] and injections of H_2O (11 s) as oxygen source, both carried in the reaction chamber by an N_2 flux. The Lu and O precursors were kept respectively at 195 °Cand 18 °C. An N_2 flux (8 s) purged away the reaction by-products after each step of the ALD cycle. The Yb_2O_3 films were deposited alternating injections of $Yb(C_5H_5)_3$ (12 s) kept at 100 C as Yb source (STREM Chemicals), and injections of either H_2O or O_3 (12 s) as oxygen sources. The Yb and O precursors were kept respectively at 100 °Cand 18 °C. O_3 was fed into the reactor in a 400 sccm flux and at a 167 g/cm^3 concentration. 310 and 41 cycles, respectively, were applied for the films studied in this work. Some samples were treated in a rapid thermal annealing furnace at 950 °Cfor 60 s in N_2. The precursor combinations of both cations with the two mentioned oxygen sources give rise to non-uniform film thickness distributions over the Si substrates (see table 3.1)

3.2.3 X-ray diffraction analysis of Lu_2O_3 and Yb_2O_3 powders

XRD measurements have been performed with an angle of incidence of 3°. Rietveld refinements have been performed starting from the powder diffraction files of the ICSD database and imposing a random texture of the crystallites. The diffraction spectra and corresponding refinements are presented in figure 3.12,3.13

Powder	Exp. Par.	Ref. Exp. (ICSD)
Lu_2O_3 cubic Ph.	a=10.394(5)	a=10.391(3)
Yb_2O_3 cubic Ph.	a=10.431(5)	a=10.436(1)

Table 3.2: Lattice parameters [in Å] as obtained from Rietveld refinement and as reported in ICSD database. The error on the last digit is indicated between brackets.

Lu_2O_3 and Yb_2O_3 powders are crystallized in the cubic bixbyite structure. Excellent agreement is found between the experimental and the reference lattice parameters. However, the relative intensities are not perfectly reproduced suggesting that a preferential orientation of the crystallites must be induced by the powder sample preparation.

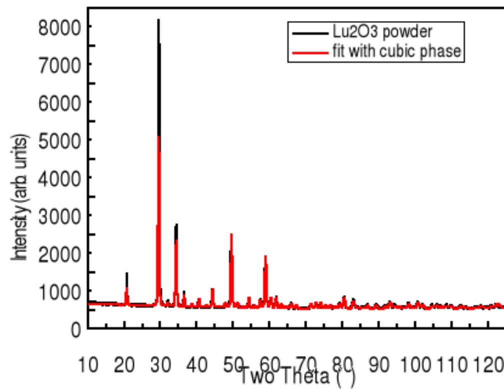

Figure 3.12: XRD of Lu_2O_3 powder.

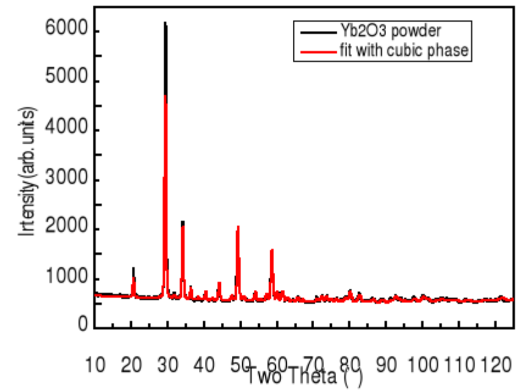

Figure 3.13: XRD of Yb_2O_3 powder.

X-ray diffraction on powder samples show the excellent agreement between the reference lattice parameters and the ones measured on powders.

3.2.4 Film characterization

Prior to XAS measurements, the films were characterized using in - house techniques. The thickness (t) was determined using x-ray reflectivity (XRR) and Rutherford backscattering (RBS) for the thicker and thinner films, respectively. The growth rates (γ) were consequently estimated. Grazing incidence x-ray diffraction (GIXRD) was used to determine the film crystallinity. The XRR spectra of as grown films were simulated by adding a low density capping layer on top of the oxide; this capping layer accounts for moisture on the film surface, and for a non-gaussian distribution of the electronic density variation and roughness.

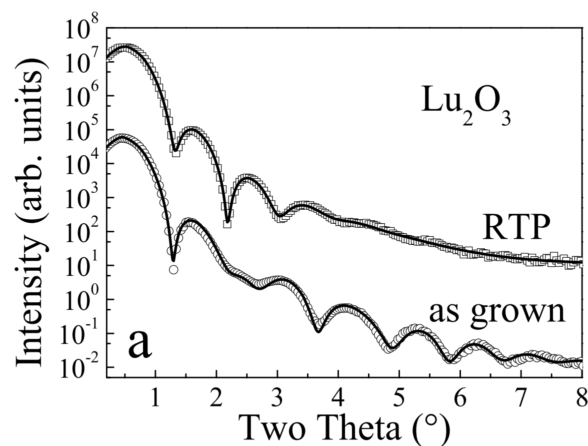

Figure 3.14: XRR of Lu_2O_3 films 8 nm thick.

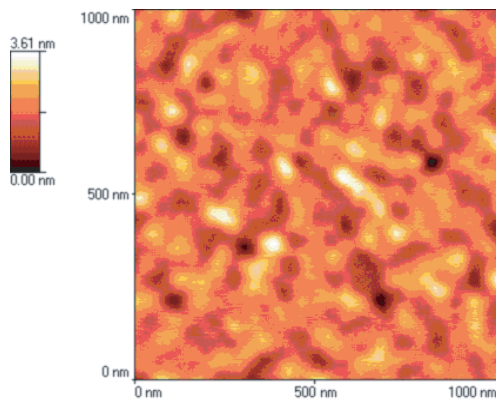

Figure 3.15: AFM image of d sample

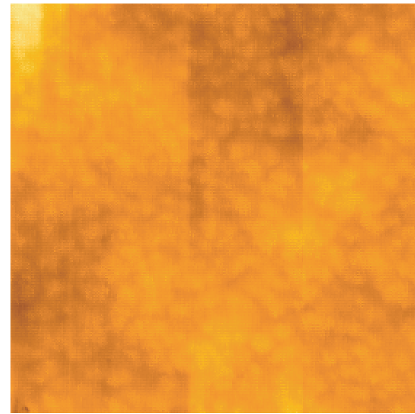

Figure 3.16: AFM image of b sample

The presence of an interfacial layer (IL) was also considered, which was simulated starting from a 1.1 nm thick layer with the electronic density of SiO_2 (0.67 $e^{-}/\text{Å}^3$). The electronic density (ρ) of each layer and the root mean square roughness (σ) were determined from XRR data by fitting to the experimental profile (not shown). The results obtained for representative films by RBS and XRR are summarized in table 3.3, which also lists the samples studied by XAS. Due to the limited signal, in - house XRR and GIXRD on films of thickness below 3 nm are not appropriate. Indeed, LEIS data show that the thinner films (sample *a* and *b*) is continuous, bacause no Si emerges on the surface Si from the substrate is detected in AES spectra (see fig 3.17), sensitive to 5 nm - of the order of the electron mean free path. From the XPS O 1s spectra it seems that the whole layer transforms into a silicate after annealing. The values

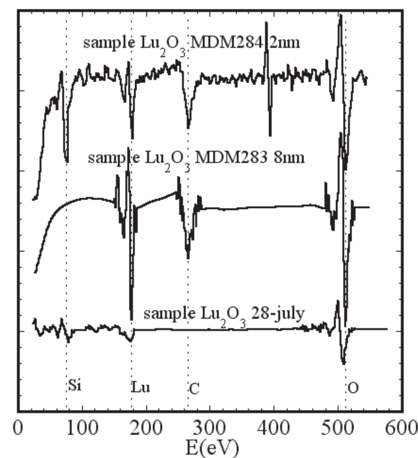

Figure 3.17:

reported in table 3.3 indicate that the determined growth rate is rather high for the Lu_2O_3 films, and does not significantly change as the number of cycles increases.

Sample	code	Layer	Ox. Precursor	Treatment	t	γ	ρ	σ_{XRR}
					(nm)	(nm/cycle)	(e^-/Å^3	(nm)
a	284	Lu_2O_3	H_2O	as grown	2.5 [RBS]	0.14		
b	284	Lu_2O_3	H_2O	annealed	3.0 [RBS]			
c	283	Lu_2O_3	H_2O	as grown	7.4(1)	0.090	2.09(5)	0.4(1)
		IL			0.9(1)		1.36(5)	0.3(1)
d	283	Lu_2O_3	H_2O	annealed	7.1(1)		2.23(5)	1.0(1)
		IL			1.5(1)		1.62(5)	0.8(1)
e	266	Yb_2O_3	H_2O	as grown	0.8[RBS]	0.020		
f	279H	Yb_2O_3	O_3	annealed	0.5			
g	270	Yb_2O_3	O_3	as grown	0.5[RBS]	0.011		
h	264	Yb_2O_3	H_2O	as grown	11.3(1)	0.036	2.22(5)	0.9(1)
		IL			1.1(1)		0.85(5)	0.4(1)
i	264	cap		annealed	1.0(1)		1.38(5)	0.7(1)
		Yb_2O_3	H_2O		8.2(1)		2.28(5)	0.6(1)
		IL			5.1(1)		1.58(5)	1.9(1)
j	268	Yb_2O_3	O_3	as grown	5.2(1)	0.024	2.39(5)	0.6(1)
		IL			1.9(1)		0.91(5)	0.4(1)
k	268	Yb_2O_3	O_3	annealed	9.0(1)		1.58(5)	0.4(1)
		IL			0.8(1)		0.92(5)	0.4(1)

Table 3.3:

Instead, for the Yb_2O_3 films the growth rate is higher in films deposited using H_2O rather than O_3 as an oxygen source, and changes significantly with the number of applied cycles. The electronic density values of Lu_2O_3 and Yb_2O_3 are consistent with those expected for stoichiometric oxides ($Lu_2O_3 = 2.18e^-/\text{Å}^3$ [77] and $Yb_2O_3 = 2.11e^-/\text{Å}^3$ [78]). Upon annealing, Lu_2O_3 films densify (film d), and exhibit an increase of the IL thickness and density. Yb_2O_3 grown both using either H_2O or O_3 undergo more dramatic changes upon annealing: the thickness of the Yb_2O_3 layer deposited using H_2O (film i) decreases, the *IL* densifies and increases significantly in thickness. The thickness of the Yb_2O_3 layer deposited using O_3 increases after annealing, and its electronic density decreases. GIXRD data and analysis are shown in Fig. 3.18. Lu_2O_3 film *c* is poorly crystallized, and after annealing crystallizes completely in the bixbyite structure [77]. Yb_2O_3 film h is crystallized already as deposited in the bixbyite structure [78]. Film *j* is poorly crystallized as deposited, partly due to its low thickness. The diffracted intensity from the annealed Yb_2O_3 films deposited using either H_2O or O_3 decreases, suggesting a low crystalline fraction in the samples. This phenomenon is related to the lower thickness of the Yb_2O_3 layer of film *i* than the one of the as grown film *h*, and to the lower electronic density of the Yb based layer of film *k*, than the one of the as deposited film *j*.

3.2.5 Chemical bonding in Lu_2O_3 and Yb_2O_3: XPS study

The composition of the films was analyzed using XPS. XPS spectra for a thick ALD Lu_2O_3 film are reported in fig. 3.19. In figure 3.19 the XPS analysis shows that the subsurface layer of as grown amorphous Lu “oxide is $Lu(OH)_3$ and that an additional oxygen state is present (besides those of crystalline Lu_2O_3 and OH^-). The intensity of *O-H* group signal diminishes after Ar^+ ion etching indicating OH^- groups present

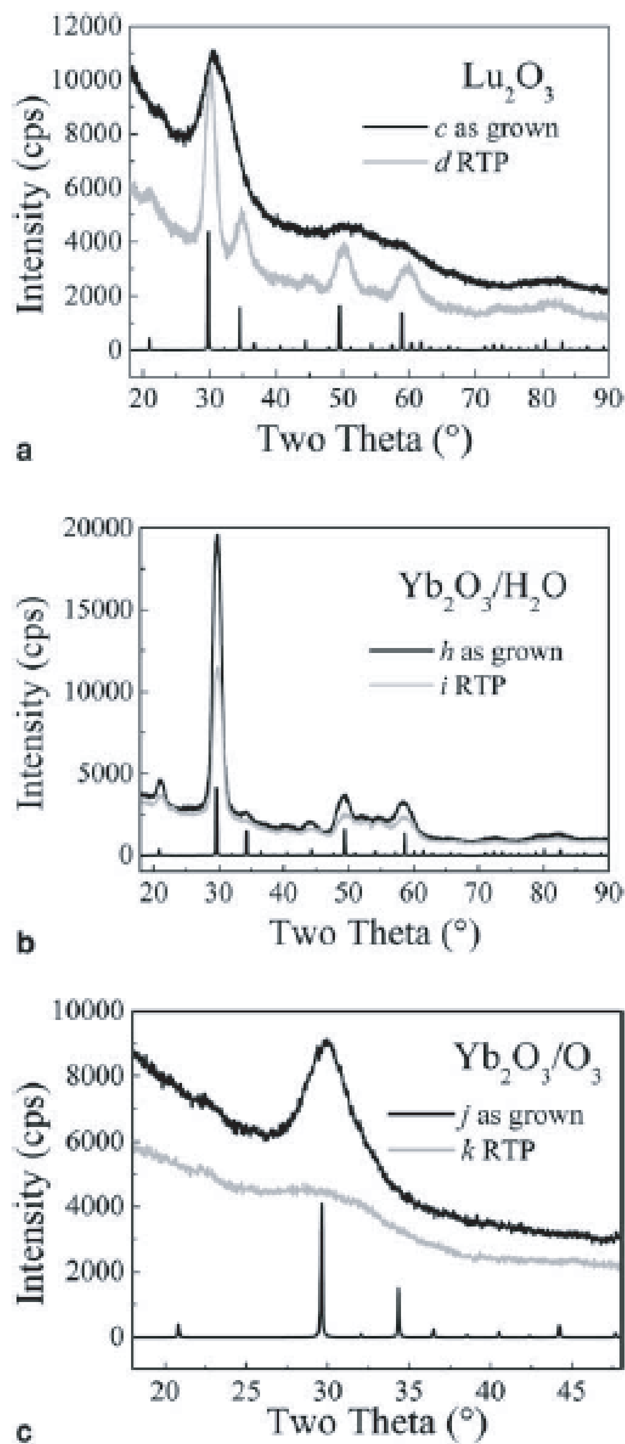

Figure 3.18: GIXRD data of films c and d (a), h and i (b) and j and k (c). As grown: black line; annealed: grey line. The position and relative intensities of the diffraction lines of bixbyite Lu_2O_3 and Yb_2O_3 as obtained from ICSD database are indicated.

only an the surface. ALD as grown ultrathin Lu oxide layers are found to be mostly $Lu(OH)_3$ (see fig. 3.20) and Lu silicate ($\approx$ 1.2 nm) is forming at Lu_2O_3/Si interface already during the growth (see fig. 3.20). Upon annealing at T=300 °Cthe surface density of (OH^-) groups decrease significantly, while the simoultaneous increasing of $O\ 1s$ peak at 531.9 eV and Si 2p line at 102.1 eV suggests that SiO_x or silicate-like compounds continue to form at the surface. Upon RTP at 950 °Cand exposition to N_2 atmosphere the Lu_2O_3 phase becomes instable and a $Lu_2Si_xO_{3-x}$ phase is formed. In this case the Silicate $O\ 1s$ signal is strongly enhanced and the Lu_2O_3 signal disappears 3.20. Skematic representations of film stacks (different layers/Si substrate) as function of film treatments are represented in fig. **??**. A model of the ALD growth of Lu_2O_3 on Si is proposed by Zenkevich et al and is reported in fig 3.21.

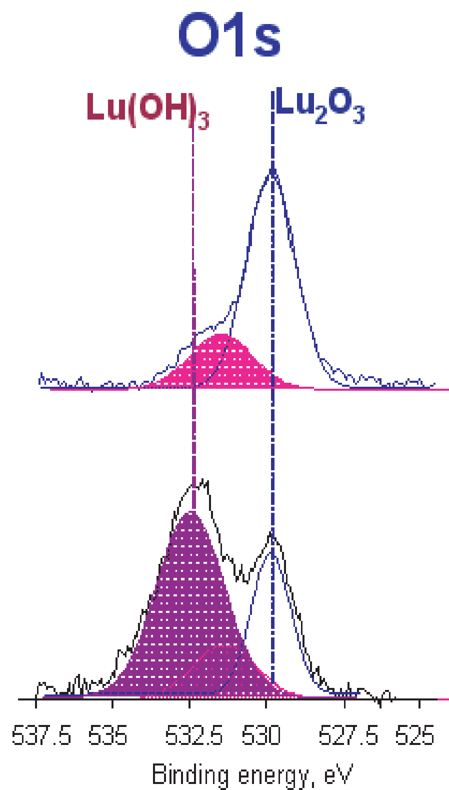

Figure 3.19: Photoemission spectra of O 1s core level.

The Yb_2O_3/Si is qualitatively similar to that of Lu_2O_3/Si (see fig. 3.22. The presence of the silicate layer at the initial growth stages of both Yb_2O_3 and Lu_2O_3 films suggests the thermodynamically instability of these oide phases at the Silicon interface.

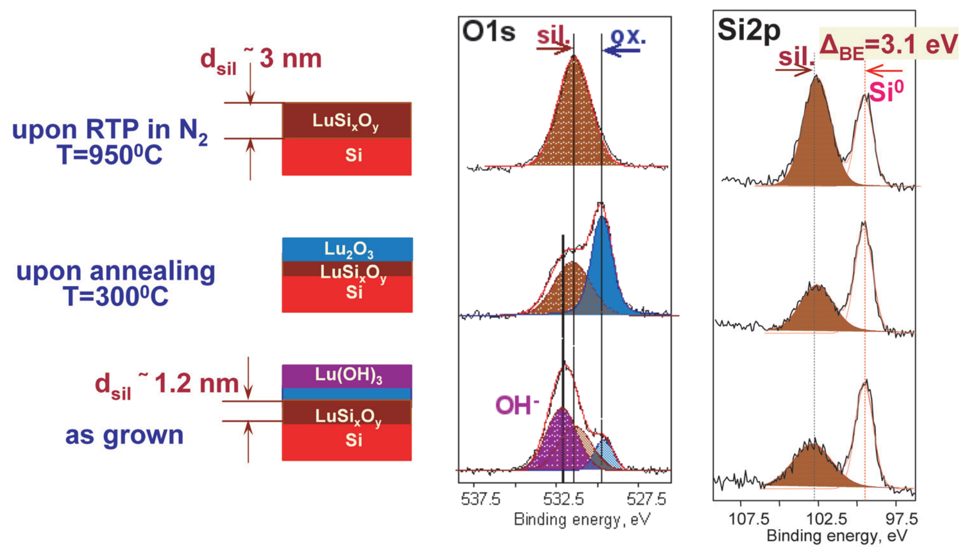

Figure 3.20:

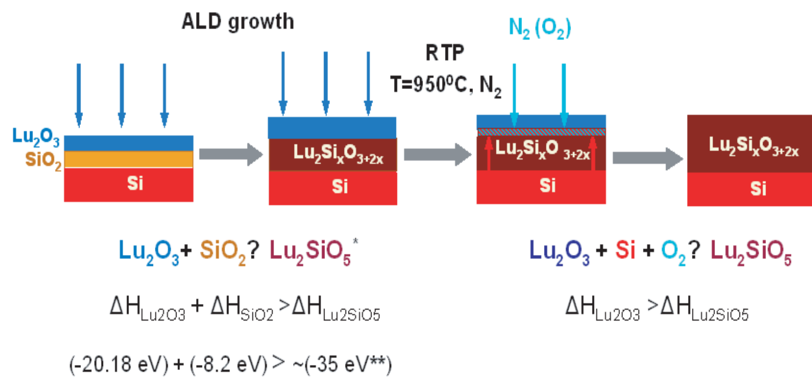

Figure 3.21:

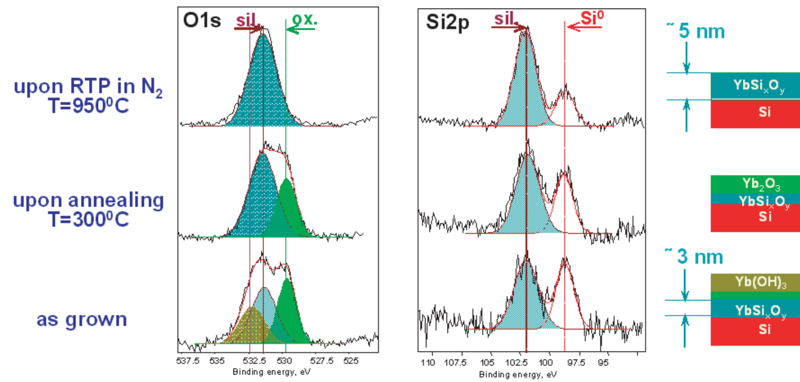

Figure 3.22:

3.3 Physical Vapor Deposition of Lu_2O_3 on Si(100) in Ultra High Vacuum conditions

An understanding of whether the film deposition conditions promote the thermodynamical instability on silicon or if the problem is intrinsic to the rare earth oxide must rely on the study of the initial stage of the adsorption process on the clean Si surface ideally in a clean environment. A description of the mechanism of the driving processes for the formation of the interface layer is lacking at present. These problem calls for an extensive study on the preparation and characterization of RE-oxide/Si interfaces. We set up a Physical Vapor Source (PVS) in an UHV chamber in order to study the growth of Lu oxide deposited on Si substrate in a series of growth conditions and post growth treatments. A PVS has been chosen to directly sublimate a rare earth oxide powder while UHV conditions avoided several problems as the formation of RE-hydroxide due to the rare earth oxide hygroscopicity and allowed to use a clean Si surface without using Oxygen terminated surface. The Physical Vapor Deposition (PVD) technique examined in this dissertation is distinct from previous PVD techniques because it uses a very high crucible temperature while maintaining UHV in the preparation chamber. Because the critical deposition processing conditions, a detailed analysis of parameters (e.g. the e-beam accelerating voltage, the filament current, the electric insulating materials) has been carried out. After set up optimization, the ability to create a low contamination films of RE oxide via this method was demonstrated and the oxide deposition to study film growth and interface formation was shown feasible. The two main phases of this study will be reported and described in the following paragraphs and consist of:

1. Previous to the film growth, an extensive optimization and characterization of the source.

2. the sample growth and characterization by means of Auger Spectroscopy, AFM, LEED and TEM.

3.3.1 Physical Vapor Deposition (PVD)

Experimental set-up.

In order to achieve reliable (controlled deposition rate, long-life of the evaporator, reproducibility) growth conditions for Lu_2O_3 ultra thin films on Silicon a PVD (PVD) apparatus has been used, with special attention to the optimization of the working parameters of the source. The apparatus consists of an Ultra High Vacuum chamber (base pressure 10^{-10} mbar), a TriCon source (used in Diode configuration; grid is not used when the crucible is mounted) [79] working as a Knudsen cell, Oxygen leak valve and standard characterization tools including a Cilyndrical Mirror Analyzer (CMA) for Auger and EELS measurements, a LEED instrument.

The PVD Source

In order to achieve a film deposition in ultra high vacuum conditions, the cleanliness, long in-vacuum life of the evaporator and working condition reproducibility are essential. The TriCon Source has been developed [79] for thin film growth on the basis of PVD working in ultrahigh vacuum (UHV) conditions. The source is based on electron bombardment: electrons are accelerated by means of high electrostatic fields (1-5 kV) and focused onto the evaporating surface. The source has been modified with special attention to:

1. the crucible shape and material
2. the anode electrical insulation

The crucible The external surface of the crucible is bombarded by electrons leading to an almost uniform heating of its entire body. No bombardment occurs inside the crucible, avoiding the problems related to material charging by electron bombardment and thus making possible the evaporation of nonconducting materials. In this way the source crucible works as a conventional Knudsen cell whose temperature can be controlled by the accelerating anode voltage. Most of the electron kinetic energy is transformed into heat and temperatures as high as 2500 K can be reached; the powder in the crucible is heated in contact with the crucible surface and powder sublimation occurs. The TriCon source crucible [79] has been modified with special attention to its shape and material (see figure 3.25). The crucible pocket like shape (figure 3.25) assures the highest $crucible\ surface/powder\ volume$ ratio and also a certain amount of sublimated material beam collimation. The dimensions of the crucible are reported in figure 3.25. In order to strongly reduce the crucible material sublimation and in order to ensure low outgassing during operation a low vapor pressure material has been used: Tantalum (see table in figure 3.4).

The home made tantalum crucible has been spot welded with a tantalum stripe to the main stain anode. The stripe keeps the crucible to 12 mm away from the stain anode in order to avoid the melting of the latter. The spot welding assures low thermal conductivity between the crucible and the stain anode.

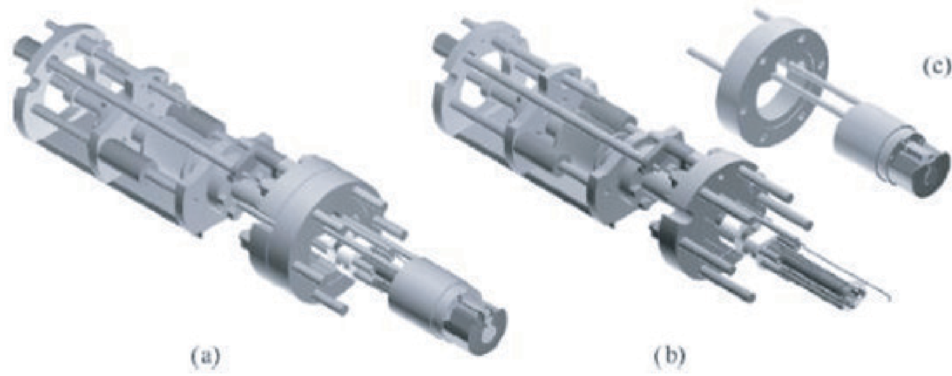

Figure 3.23: (a) CAD three dimensional view of the TriCon source; (b) electrodes/linear motion assembly; (c) cooling shroud, with double sided CF35 flange.

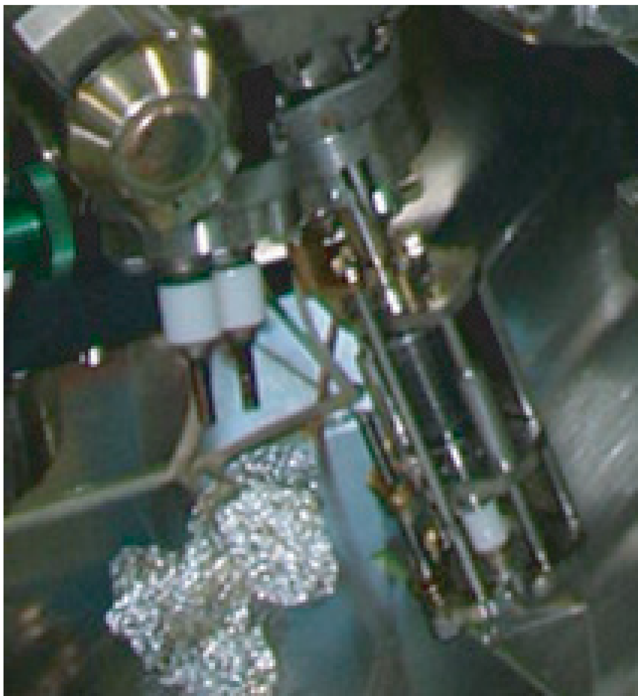

Figure 3.24: Photo of TriCon source mounted on the IPES preparation chamber.

Ta	Vapor Pressure (Torr)	Temperature °C
	10^{-8}	1957
	10^{-7}	2097
	10^{-6}	2237
	10^{-5}	2407
	10^{-4}	2587
	10^{-3}	2807
	10^{-2}	3057
	10^{-1}	3357
	1	3707

Table 3.4: Tantalum Vapor Pressure vs. Temperature (VEECO)

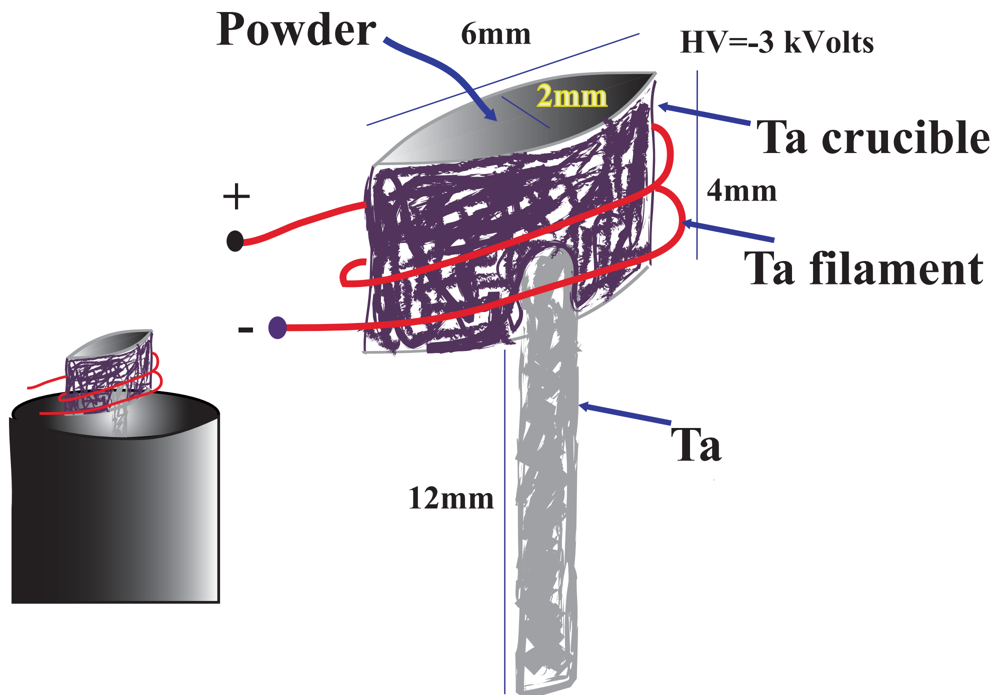

Figure 3.25: Tantalum home made crucible with hot filament (red)

The anode electrical insulation. The position of the anode and its distance from the anode shield is controlled by three *iron* screws which are directly in physical contact with the anode and are mounted on a Teflon support which is fixed to the anode shield. The support assures the electrical insulation between the screws, in contact with the anode, and the anode shield (mass). As the temperature of the Teflon support increases due to the thermal dissipation of the crucible, electrical breakdown occurs between the anode and the mass when the accelerating high voltage is applied to the anode. In fact, the material resistivity of the support (Teflon volume resistivity ohm/cm $1.0 \cdot 10^{16}$ at 300 K and $1.0 \cdot 10^{9}$ @ 500 K) strongly reduces with increasing temperature. In order to avoid this problem, alumina (Alumina volume resistivity ohm/cm $1.0 \cdot 10^{18}$ at 300 K and $1.0 \cdot 10^{16}$ @ 500 K) screws have been used between the Teflon support and the anode (see figure 3.26).

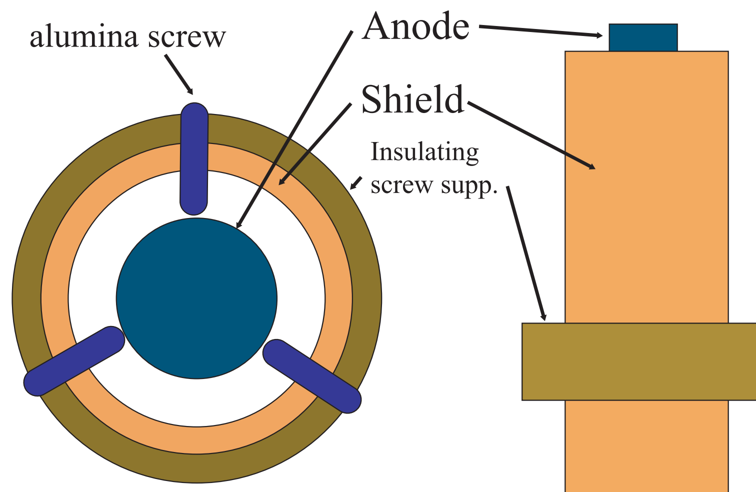

Figure 3.26: Alumina screws have been used as spacers between the anode and the anode shield.

3.3.2 The calibration of the PVD Source.

The reproducibility of film growth is extremely dependent on the reproducibility of source working conditions. The source calibration, i.e. the deposited film thickness as function of source calibration, has been done as follow. The main source parameters we considered were anode voltage and anode current (source power). First of all we deposited a series of Lutetium oxide films on a Si(100) clean surface. For each film thickness, the presence of chemical components in the film, the film quality and thickness has been monitored by measuring Auger spectra. A comparison of Auger spectra measured on successive Lu_2O_3 evaporations on a Si substrate is reported in figure 3.27. The Si peak at 90.1 eV, the Lu peak at 177 eV, the C (contamination) peak at 250 eV and the O peak at 500 eV are apparent and indicated in figure 3.27. Despite UHV conditions and accurate degassing of source, slight C contamination of Si substrate may occur due to residual C upon the cleaning procedure of the Si surface, or C on the chamber surface.

Auger spectra have been recorded as function of deposition time (t_s). Figure 3.28 reports the Si Auger peak amplitude measured on the sample as function of the exposure time of the Si surface to the Lu_2O_3 source. The thickness of film has been calculated as follows: the AES signal from the Si substrate is attenuated (i.e. reduced in intensity) due to inelastic scattering of some of the Si Auger-electrons as they traverse through the layer of adsorbate film [80]. The probability of such a scattering event for any single Auger electron passing through this layer is simply given by :

$$P = e^{\frac{-t}{\lambda}} \tag{3.1}$$

where: t is the thickness of the layer of the film and λ is the IMFP (inelastic mean free path) of the Auger-electron. It follows that the overall intensity of Auger signal is

$$I = I_0 e^{\frac{-t}{\lambda}} \tag{3.2}$$

where I_0 is the intensity of this signal in the absence of any covering layer. Due to the extended collecting aperture of the *CMA*, the above intensities should be integrated over the collection angle:

$$I = \int 2\pi I_0 e^{\frac{-t*\sec\theta}{\lambda}} d\theta \tag{3.3}$$

where θ is the angle of the electron direction to the surface normal. For the CMA with its axis along the surface normal and up to 45° from the normal an effective $\cos\theta = 0.74$ is found [81]; for other conditions lower values generally occur. In figure 3.28 the green line represents the thickness versus deposition time if the extended collecting aperture is considered, the blue line if it is not considered.
Its possible to calculate λ resolving the above equation with a set of experimental values of I and t_{exp}:

$$\lambda = t_{exp} \cdot 0.74 \cdot ln\left\{\frac{I_{exp}}{I_0 \cdot 4\pi^2}\right\} \tag{3.4}$$

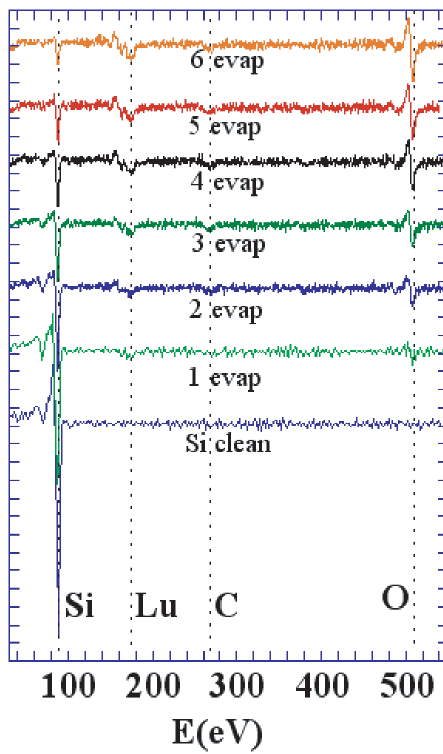

Figure 3.27: Auger spectra measured on a series of successive evaporations of lutetium oxide on Si(100).

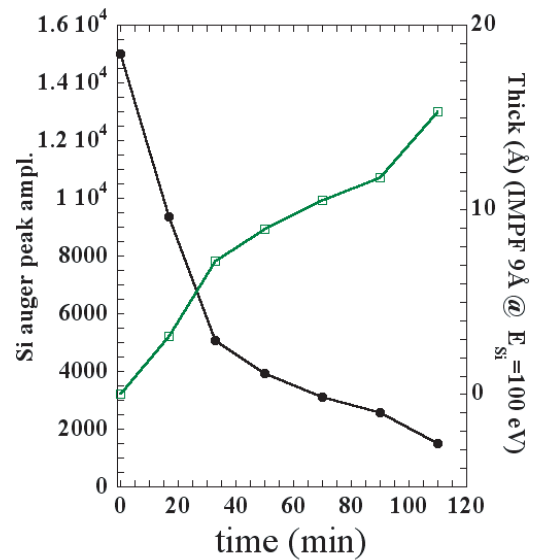

Figure 3.28: Si Auger peak amplitude and nominal thickness versus exposure time to the TriCon source.

In order to calculate λ, equation 3.4 has been resolved respect to I_{exp} (from AES) and t_{exp} (from TEM) measured for the sample grown at 450 °C(λ = 1.2 nm). At last, the thickness of the film upon Si peak intensity I is:

$$t = \frac{\lambda}{0.74} ln \left\{ \frac{I_0 \cdot 4\pi^2}{I} \right\} \tag{3.5}$$

In figure 3.28 is apparent the presence of a *knee* in the decreasing of Si Auger amplitude; it is due to the change from a rate of the Si Auger signal amplitude reduction $I = I_{0Si} \cdot \Theta_1$ to a different rate $I = I_{0Si}(1 + \Theta_2 e^{-t_1/\lambda})$ (I indicates the Si Auger peak intensity, Θ is the fraction of covered surface, λ is the Auger IMFP) ; this change indicates the formation of a layer on the substrate with coverage parameter $\Theta = 1$ (total surface coverage); so the *knee* feature indicates a complete coverage of the substrate. Now it is possible to calibrate the source by reporting the source power (anode voltage$\times$ anode current) vs. film thickness deposited in a fixed time interval (see table 3.5).

	Source power (W)	thickness (nm)	t_s (s)	deposition rate (nm/s)
film1	80 (2kV· 40mA)	0.4	270	0.0014
film2	100 (2.2kV· 45mA)	0.6	270	0.0022
film3	125 (2.5kV· 50mA)	2.7	270	0.010

Table 3.5: In this table, the TriCon source power and the calculated thickness deposited over a fixed time interval are reported.

In figure 3.28 the film thickness vs. time deposited using a 120 W source power is reported. The following chosen source working parameters were used in all deposition experiments:

- Source power: 125 Watt (2.5kV· 50mA)
- filament current: 6.0 Ampere
- deposition rate: 0.01 nm/s (0.1 Å/s)

3.3.3 Sample growth.

Substrate preparation

A clean surface is an important prerequisite for studying the initial stages of adsorption process. Most Si wafer vendors currently supply epi-ready wafers which are pre-cleaned and oxidized in a controlled environment. The oxide forms a protective layer which can be removed inside the growth chamber. The Si substrates were mounted on a sample holder by means of two clamps (see figures 3.30 and 3.29) and successively put into the preparation chamber. The specimens were heated, using direct current applying a DC voltage to the clamps. The substrate was heated by slowly increasing current through it while maintaining a pressure in the low 10^{-10} mbar range; the sample was heated for 12 hours to outgas the samples and sample holder (fig 3.29) at an outgassing temperature of 450 °C. After the outgassing, the substrate was cleaned in situ by thermal desorption of chemical silicon dioxide at T≈1000 °C for subsequent current flashes of 20 seconds; the background pressure in the cleaning chamber was $3 \cdot 10^{-10}$ *mbar* and during cleaning procedure the pressure was mantained below $2 \cdot 10^{-9}$ *mbar*. The Si (100) surface cleaning was monitored by measuring the Auger electrons emitted in the energy range [20-550] eV. The cleaning procedure has been monitored by means of subsequent Auger spectra measured after each series of thermal flashes. At the end of cleaning procedure, only the *Si LVV* Auger peak at *90.1 eV* is apparent in the Auger spectra of clean Si surface 3.32. Moreover, at the end of cleaning procedure a reconstructed 2×1 Si(100) surface has been obtained as seen by LEED image. (see LEED in figure 3.33 and 3.31). The clean Si surface LEED image formed on the fluorescent screen by the backscattered Bragg reflections associated to an incoming 45.6 eV electron beam is reported in the figure 3.32. In figure 3.31 a model on how the real space surface reconstruction appears in the reciprocal space is illustrated.

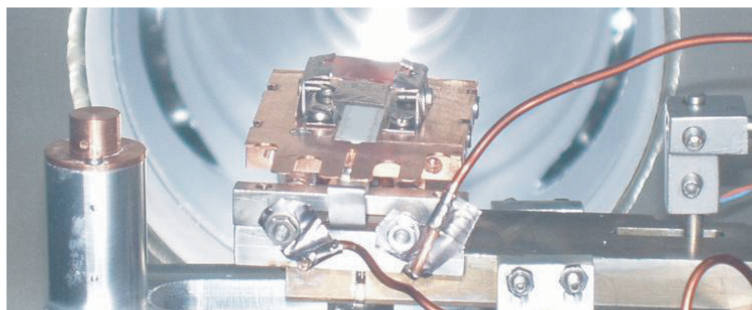

Figure 3.29: Photograph of Si substrate during flashing in UHV condition in the IPES lab preparation chamber

The Si substrate surface temperature has been successively measured as function of temperature by means of an optical pyrometer (set to the Silicon surface emissivity equal to 0.77). The surface temperatures versus heating currents are reported in the plot in figure 3.34. This calibration will allow us to set the proper temperature during annealing procedure or film growth.

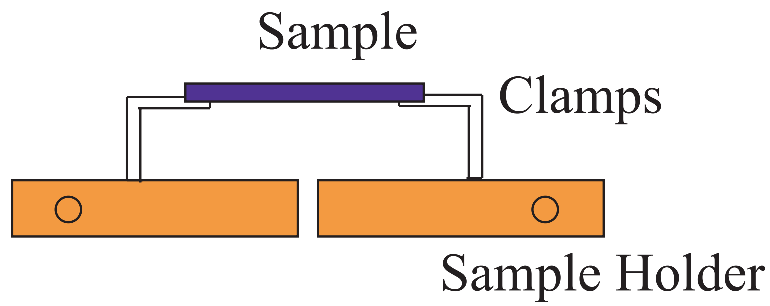

Figure 3.30: Sample holder and sample electrical connections (clamps).

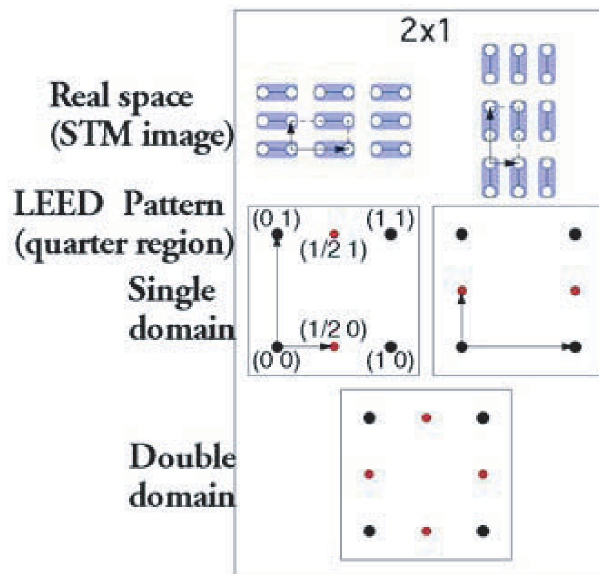

Figure 3.31: LEED model image compared to real space model of surface

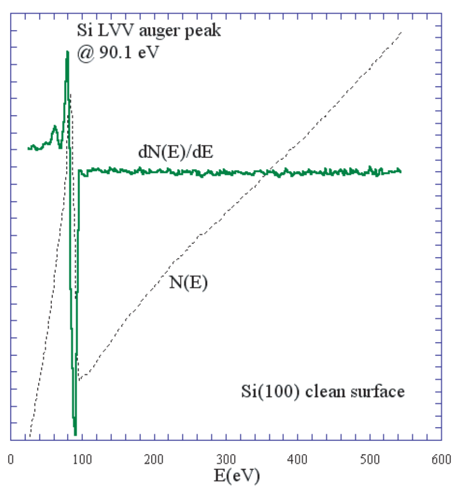

Figure 3.32: Auger spectra measured on a clean Si surface

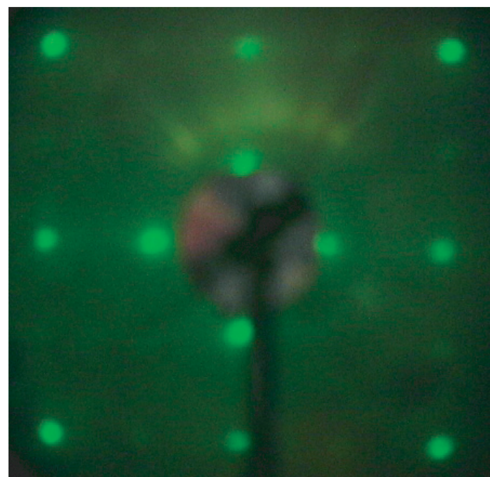

Figure 3.33: LEED of Si(100) clean surface

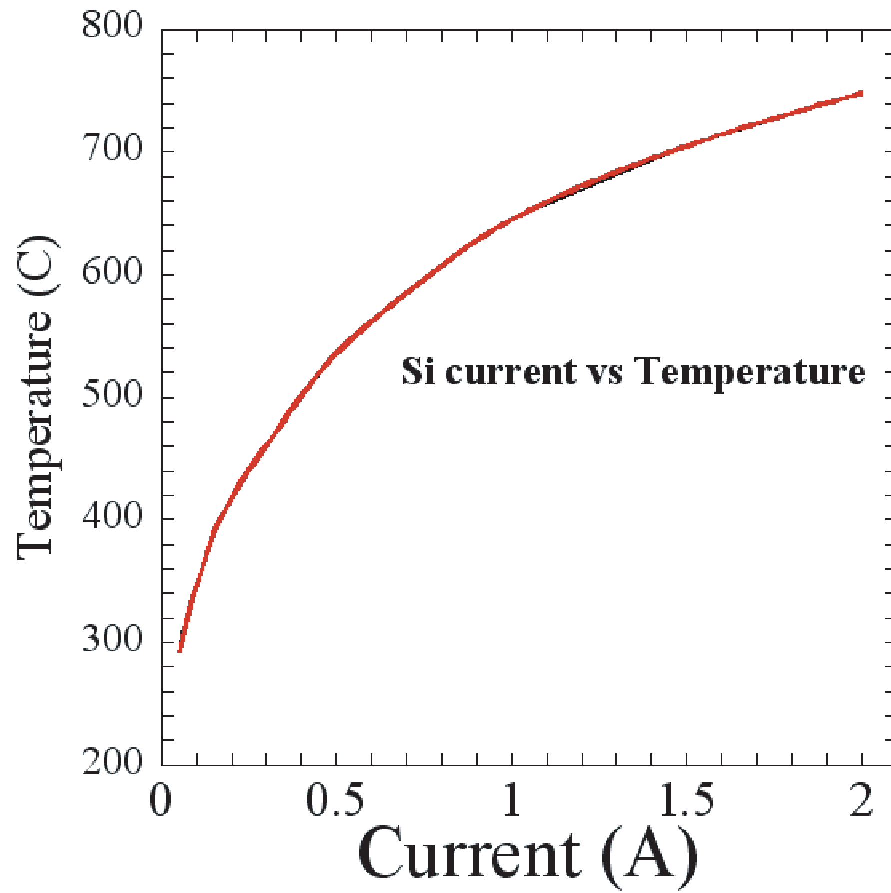

Figure 3.34: Clean Si substrate surface Temperature as function of heating current.

Stoichiometry

A measurement of the relative concentration of Lu and O allows the detection of possible deviations from the ideal 2:3 stoichiometry of Lu_2O_3. The stoichiometric ratios were calculated as follows:

$$R = \frac{N^{Lu}_{sample}}{N^{O}_{sample}} = \frac{\frac{I^{Lu}_{sample}}{I^{Lu}_{ref}}}{\frac{I^{O}_{sample}}{I^{O}_{ref}}} \tag{3.6}$$

where I^X_{sample} and I^X_{ref} refers to the Auger peak intensities of sample and reference sample respectively (see table 3.6 and 3.7). ALD grown Lu_2O_3/Si sample, 8 nm thick, has been used as reference samples. The Auger spectra of reference sample is reported in figure 3.35. Previous to the Auger measurement, the reference sample (only the thicker one) has been annealed at 300 °C for 30min [82]. In figure 3.35 the Si LVV

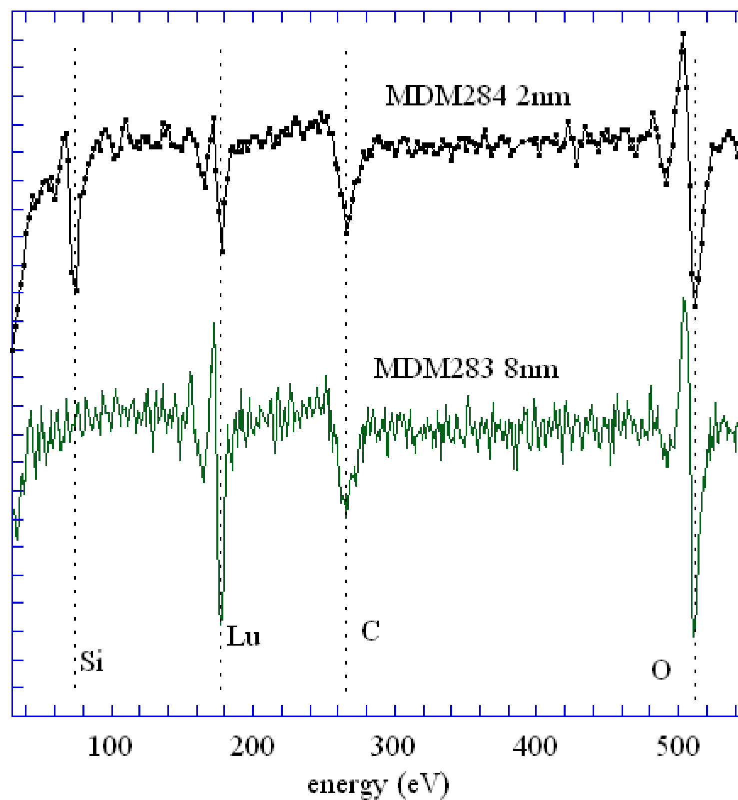

Figure 3.35: MDM reference samples: Auger signals of the sample 283 8nm thick and the sample 284 2nm thick.

Auger peak at 90.1 eV disappears in the thicker sample due to the limited penetration

length of Auger electrons coming from the Si substrate. Besides, the thicker layer results not contaminated by Si interdiffusion as confirmed by the disappeared Auger Si peak. Therefore the thicker Lu_2O_3 film have been considered the reference sample. The stoichiometry of these samples has been determined by Rutherford Backscattering Spectroscopy (RBS) [82].

Deposition of Lutetium oxide films.

A series of thin film samples ($\leq$10nm thick) were grown by PVD on Si(100) substrates under UHV conditions. The films were subsequently characterized by Auger spectroscopy, AFM, LEED and TEM. The O_2 partial pressure in the growth chamber was kept low with the intention to minimize or avoid the oxidation of the Si substrate. The primary objectives were to address in a systematic manner the quality of the deposited films and the presence and nature of (Lu Oxide)/Si interface layer upon thickness, growth temperature (T_g) and annealing. In table 3.7 are reported the growth parameters of selected films.

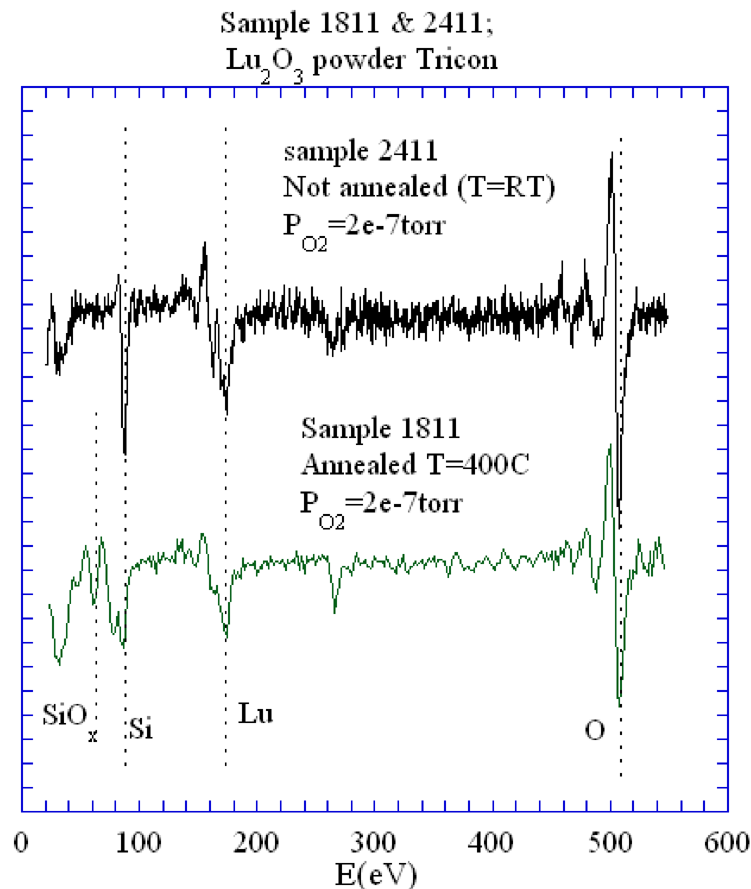

Figure 3.36: Comparison of Auger signals of annealed/not annealed Lu_2O_3 films obtained from TriCon source

T_g = room T

T_g = room T
T_{ann}=400 ^oC

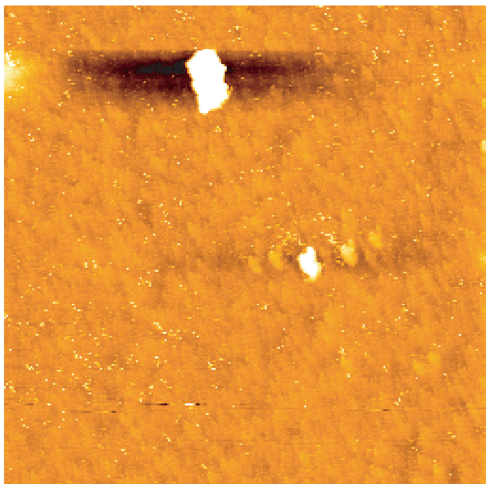

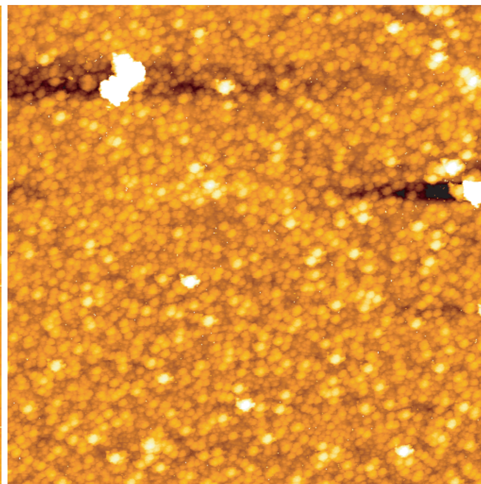

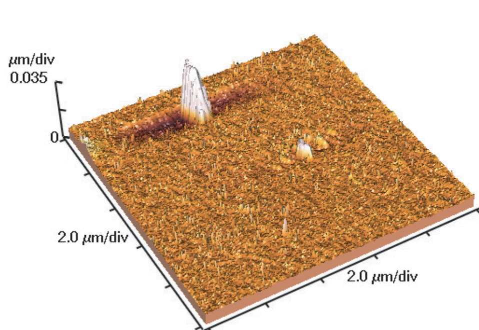

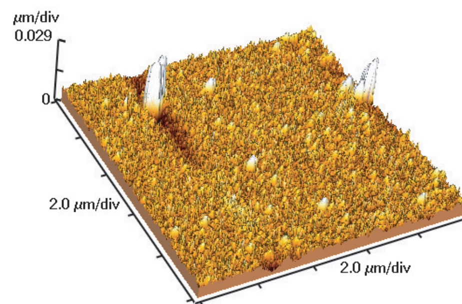

Figure 3.37: An $10{\times}10\mu m^2$ AFM image of the Lu_2O_3 2 μm sample grown at RT and post-annealed at 400 °C in O_2 atmosphere at p=$2{\cdot}10^{-6}$ mbar

sample	*source*	*ave r.* (*nm*)	*rms r.* (*nm*)
MDM	*ALD*	0.1917	0.2346
1811	*TriCon*	1.256	1.484
2411	*TriCon*	0.1559	0.1669

Table 3.6: Average (ave r.) and root mean square roughness (rms r.)

sample	R	thickness (nm)	T_g (°C)	anneal (°C)	$O_2(mbar)$	TEM	LEED	AFM
1811	0.69	2	RT	400	$2*10^{-6}$			
2411	1.08	2	RT	no	$2*10^{-6}$			
290405		2	350	no	no	clustering	none	clusters
110505	0.76	2.1IL+(2.5÷6.1)OL	450	no	no		none	clusters
030505	1.3	0.5IL+(1.4÷2.4)OL	610	no	no	small cryst. island interface layer	streaks	clusters line up
170505	1.6	2	650	no	no	abrupt interface	streaks	clusters line up

Table 3.7: Growth parameters and main features of grown films are reported in this table. IL and OL stands for Interface Layer and Over Layer.

Data and Results

In this section I present the data of the deposition of Lutetium Oxide films. Data will be illustrated considering the growth temperature T_g reported in table 3.7. Moreover, for selected temperatures (450 and 610 °C), data will be described according to the sample thickness.

The structural quality of the films were characterized by Auger, AFM, LEED and cross-sectional TEM. Film grown at room temperature (sample 2411) typically exhibit clear Auger peak of Lutetium at 177 eV, an intense Oxygen peak at 510 eV (see figure 3.36). R_{sample} for the as grown film is 1.08 indicating the presence of possible different oxidised lutetium phases like lutetium sub-oxide and/or lutetium silicate. However, the Si peak at 90.1 eV is slightly different from the clean Si Auger peak (figure 3.32) even though no energy shift occurred. This difference may indicate that possible lutetium silicate (Si-O-Lu) or SiO_x may be formed during the deposition. A small amount of C contamination probably degassed from the source during the Lu_2O_3 powder sublimation as indicated from the Auger peak at 255 eV. The Oxygen peak intensity increase upon the exposure of the film to O_2 atmosphere (sample 1811) and the final R_{sample} is 0.69 very similar to the reference sample. However it is not possible to distinguish between Oxygen in Lu_2O_3 phase and Oxygen in other phases like $Lu_{2-x}O_{3-x}$ or Lu silicate. Only in this annealed sample exposed to O_2 atmosphere we observe the Si oxidation in the SiO_2 phase from the Auger spectra; in fact the Si_{LVV} Auger peak shape and energy position are very similar to that reported in figure 3.38 measured on SiO_2 sample. Indeed, we cannot exclude that small amount of other phases (Silicates) are present in the other samples. The as grown and annealed films are more throughly examined by AFM. 10×10 μm^2 images are reported in figure 3.37. The as grown film surface average roughness is 0.1559 nm while increasing upon annealing at 1.256 nm. In fact, it is worth noting the formation of clusters in the annealed sample. The film

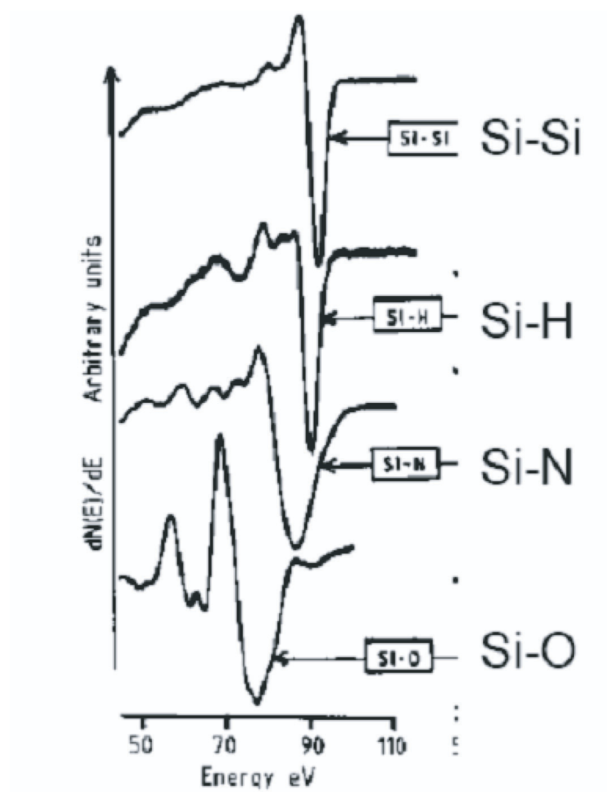

Figure 3.38: Si_{LVV} Auger peak as function of ligands and final states

has irregularities as it is apparent in figure 3.39. The thickness of the oxidised film is in the range 2.3-2.6 nm as it is seen from bright field image of cross sectional TEM reported in figure 3.39. It is apparent from TEM reported in figure 3.39 that the surface of the film is irregular due to the presence of clusters. This well correlates with AFM.

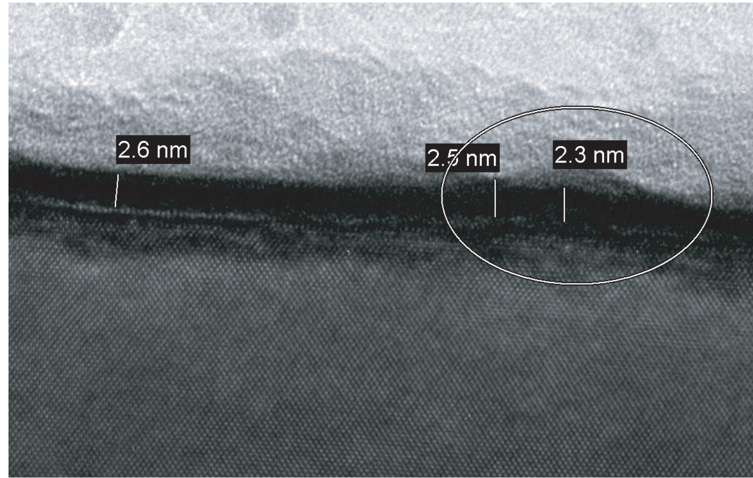

Figure 3.39: TEM images of the sample grown at room T_g

Films grown at 350 °C typically exhibit the formation of clustered and strongly irregular surface. It is seen from figure 3.40 that the film has an average thickness of 2nm and it is not apparent the presence of an interface layer. The Si surface present many dislocations which are filled of crystalline islands 20 nm thick. The O Auger peak intensity (see figure 3.41) is strongly reduced compared to the sample grown at room temperature (see figure 3.36). Moreover, the Si peak corresponds to an unoxidized Si surface.

The O Auger peak increases either when the T_g is increased to 450 °C and when the thickness of the film increases. R_{sample} results to be 0.76 (above the 2:3 ratio). It is apparent from figure 3.41 the shape changing of the Si_{LVV} peak respect to the clean Si peak (see figure 3.32) while the its energy position remaining unchanged. It is seen from AFM images (figure 3.43) the formation of a clustered surface. Such irregular surface structures are confirmed by the TEM investigation. It is seen from the TEM image in figure 3.40 that the structure of this film has the form layer/interface-layer/substrate. The thickness of the film (see figure 3.40) is in the range (2.5-6.1 nm) while the interface layer results to be 2.1 nm thick.

In the film grown at 610 °C the film thickness is in the range 1.4-2.4 nm as revealed by the TEM investigation. In figure 3.40 the film is apparently irregular; an interface layer 0.5 nm thick has been found between the substrate and the film. The low intensity of the O Auger peak confirms that in thin films R_{sample} is 1.3 (far from the 2:3 bulk ratio). Moreover, the shape of Si_{LVV} peak is apparently different from the clean Si case while the energy position remains unchanged. It is seen from AFM images the formation of clusters with average lateral dimensions 50nmX50nm lining up along preferred

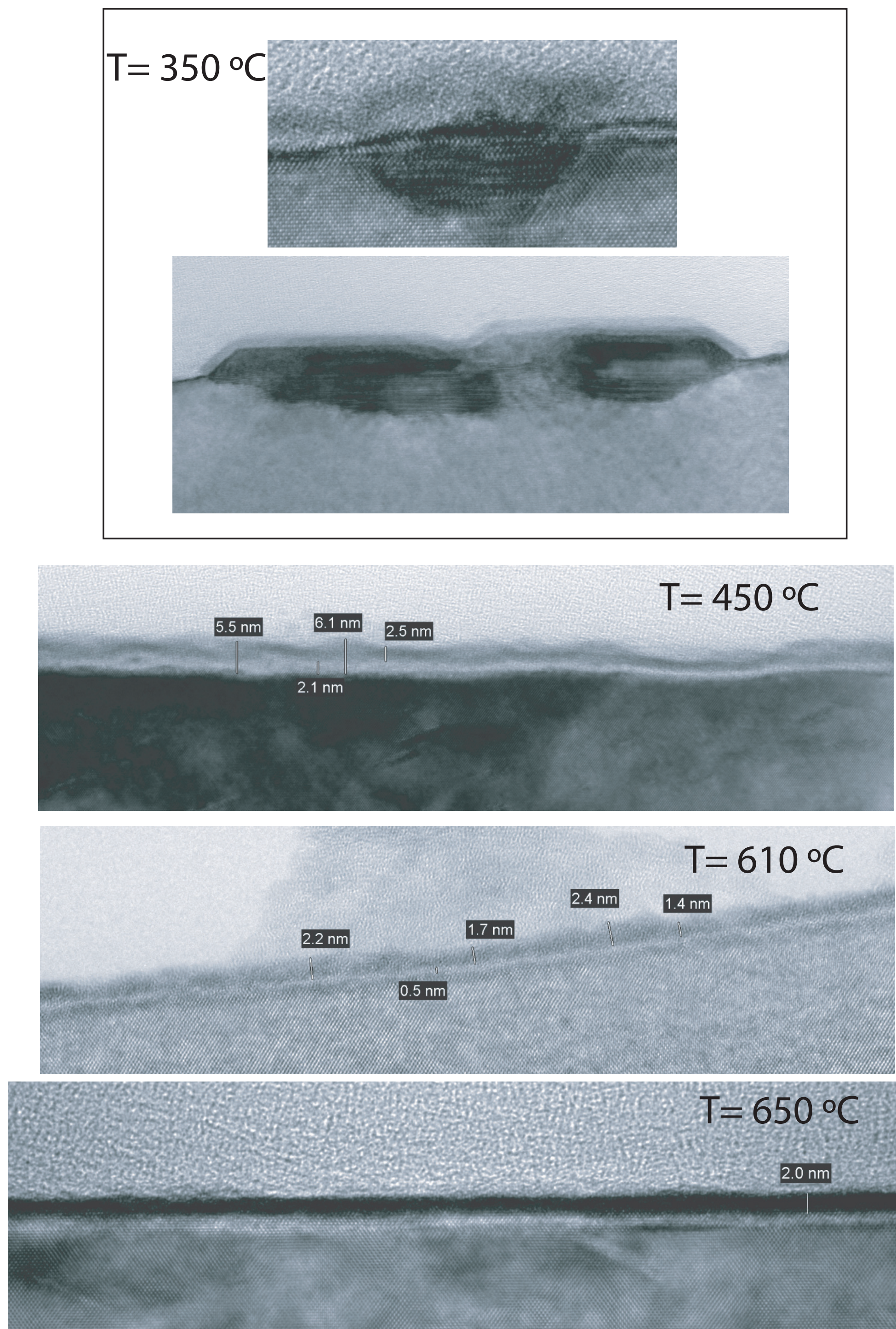

Figure 3.40: TEM images of samples grown at different T_g

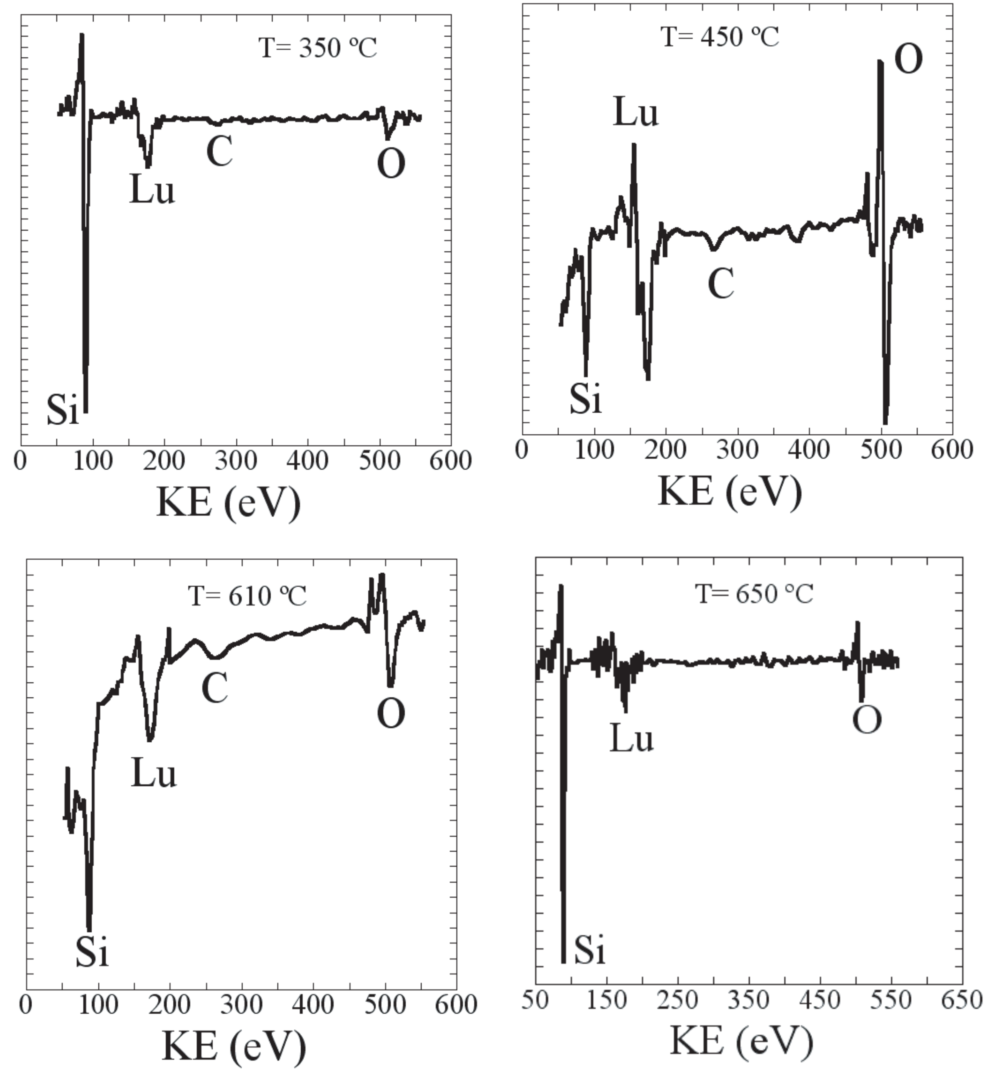

Figure 3.41: Auger spectra of samples grown at different T_g.

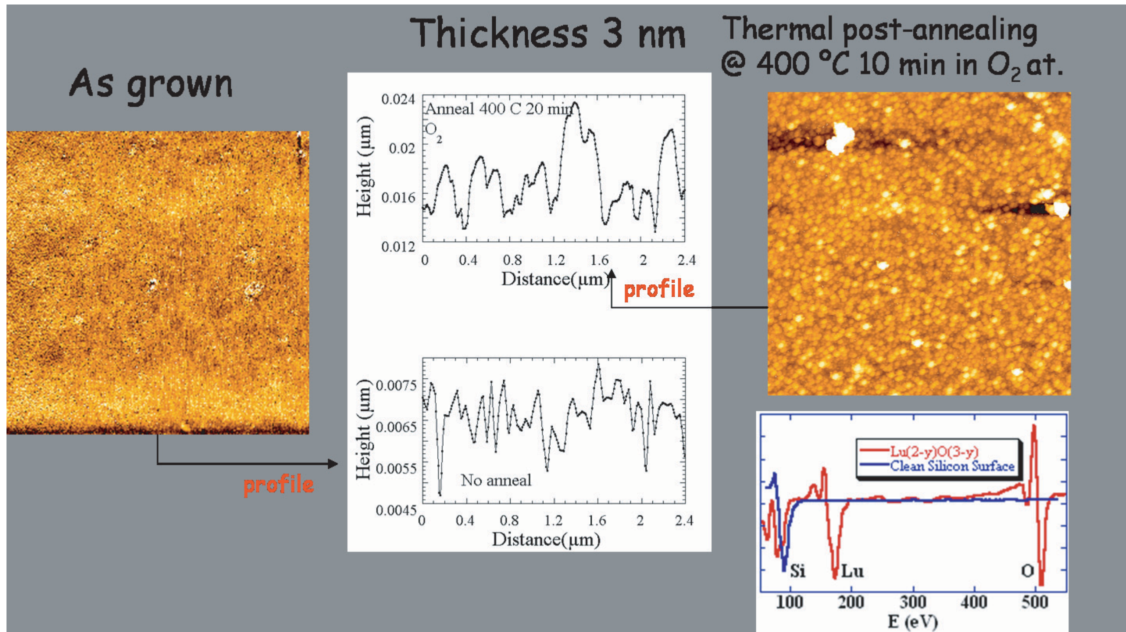

Figure 3.42: Comparison of AFM and LEED images for samples grown at RT and post annealed in a O_2 atmosphere.

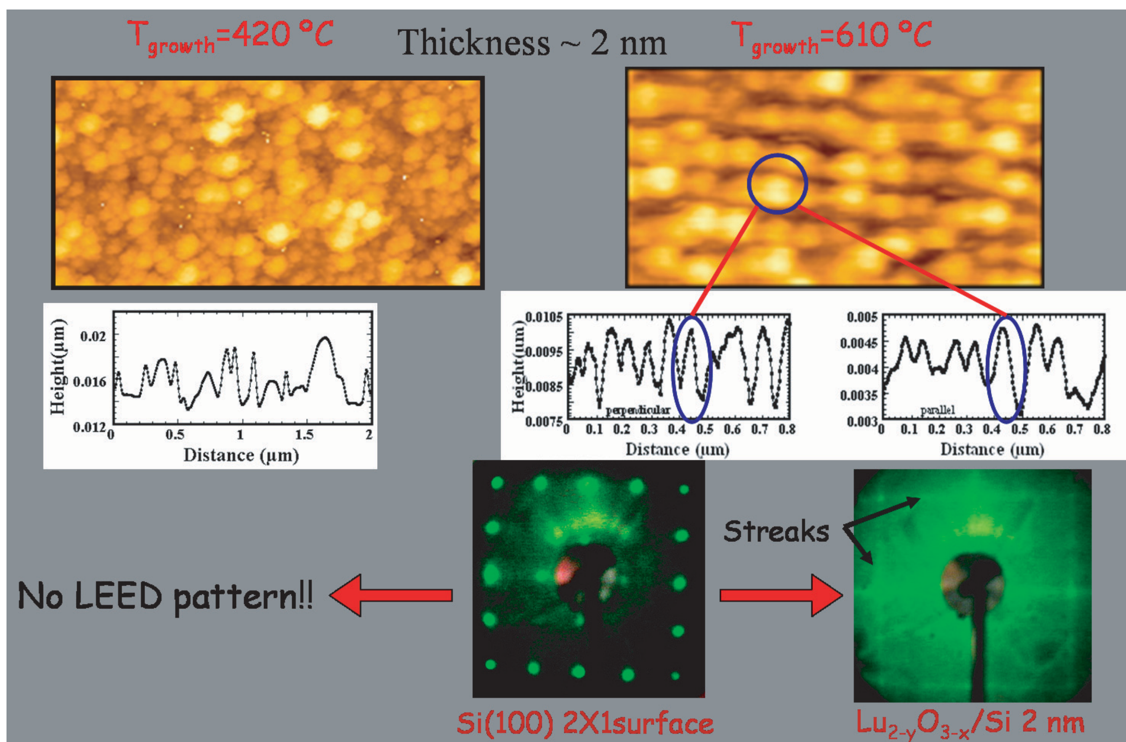

Figure 3.43: Comparison of AFM and LEED images for samples grown at 450 and 610 °C.

directions. This real space structures are present in the reciprocal space; in fact, it is seen in the LEED images in figure 3.43 the appearing of lines (streaks) connecting (superimposed with) the weak 2×1 reconstructed surface double-domain Bragg spots. Also, a sizable increase of the background can be noticed. The formation of streaks is determined by the formation of defected structures with $1Xn$ periodicity on each of the two domains. Adsorbed particles occupy neighboring rows with constant mutual distance within rows and random phase shifts between the rows. This kind of one dimensional disorder gives rise to sharp diffraction spots in integral order positions and streaks in fractional order [83].

In the film grown at 650 °C all the results from the previous case are confirmed but the presence of the interface layer. In fact, it is apparent from the TEM image in figure 3.40 the presence of an abrupt interface between the Si substrate and the overlayer. The film is uniformly 2.0 nm thick and has no irregularities or dislocations. First of all, it is worth noting that R_{sample} ratios in all samples grown at T_g above room temperature are significantly different from the bulk ideal ratio 2:3. This indicates an overall oxygen deficiency but also the possible presence of different oxygen bonding configurations. It is worth noting that the Si_{LVV} Auger peak shape changes correlate with the formation of an interface layer between the Lu_2O_3 film and the substrate as it is apparent in the samples grown at 450 and 610 °C respectively from TEM investigation. Since in these cases the Si_{LVV} shape is different compared to the Si_{LVV} peak corresponding to the Si-O bonds in SiO_2 as revealed in the annealed sample grown at room T, (see figures 3.36 and 3.38) we argue that possible $Si-O-Lu$ or $Si-Lu$ ligands may occur in the interface layer. However, since the Lu Auger peak shape and energy position remain unchanged in all samples we may conclude that only Lu-O ligands should be present in the film. A typical evolution of Auger spectra upon thickness is reported in figure 3.45. In fact, The Si_{LVV} peak modification in the 450 °C sample is apparent from the Auger data reported in figure 3.45; in this plot Auger spectra measured on successive deposition are reported. It is apparent that the Si peak shape modifies from the clean Si shape to a possible silicate Si-O shape upon increasing thickness. On the contrary, the Si_{LVV} peak shape remains unmodified upon thickness in the sample grown at 650 °C as it is seen in figure 3.44.

As far as R_{sample} is concerned, differences with thickness are also observed. We analyze the case of The film grown at 450 °C which results to be the thickest one; its final R_{sample} is 0.76 indicating that the oxygen deficiency reduces with increasing thickness. Moreover, in table 3.8 are reported R_{sample} ratios calculated from the O and Lu Auger peak intensities measured in the successive deposition (so as function of film thickness)(see figure 3.45) of the film grown at 450 °C. The thickness has been calculated following the Si_{LVV} peak intensity. The initial R_{sample} value is 1.10 corresponding to a film 1.3 nm thick. The decreasing of the ratio value starts with a film thickness of 2.4 nm and reaches the lowest value at 5.6 nm. The R_{sample} values upon thickness well correlate with the film structure (overlayer/interface/substrate) as revealed by TEM in figure 3.40: in the interface layer region the ratio is ≈ 1 (similar to Si-Lu-O silicate configuration) while decreases to 0.76 in the thickest Lu_2O_3 overlayer. This sort of correlation indicates that the first stages of film formation consist in SiO_x and LuO_x (possible LuSiO silicate may be present but no evidence from Auger spectra) due to

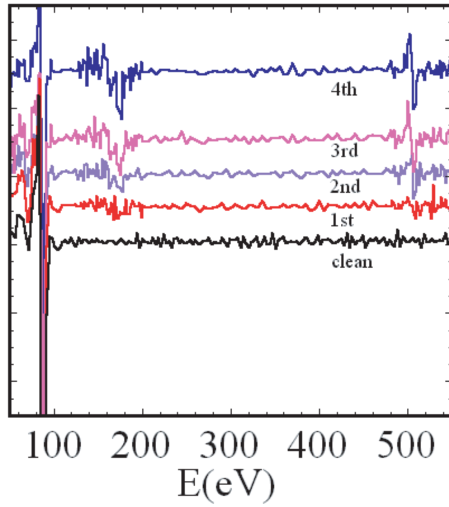

Figure 3.44: Auger spectra measured on the sample grown at 610 °C

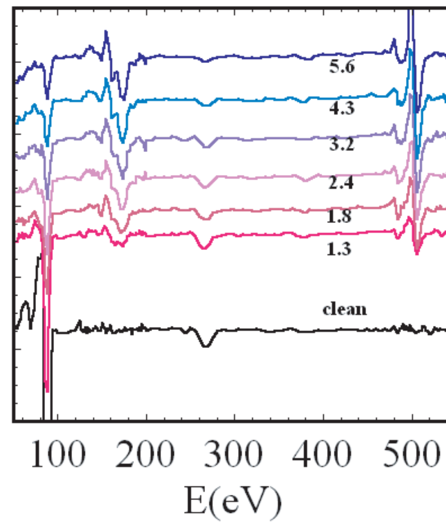

Figure 3.45: Auger spectra of a series of successive deposition of the sample grown at 450 °C . Thickness is reported in nm.

	ratio	thickness (nm)
1st evap	1.10	1.3
2nd evap	1.15	1.8
3rd evap	0.91	2.4
4th evap	0.86	3.2
5th evap	0.82	4.3
6th evap	0.76	5.6

Table 3.8: Sample grown at 450 °C: R_{sample} ratio calculated with increasing thickness.

Si oxidation and/or interdiffusion , while with increasing thickness the oxygen or the Si atom interdiffusion from the substrate into the growing film reduces or stops and the growing film result in a mixture of stoichiometric and sub-stoichiometric amorphous (or polycrystalline) layer. Besides, R_{sample} varies with varying temperature. At room temperature R_{sample} of the as grown film is near to 2:3 while with increasing T R_{sample} increases toward a 1:1 ratio. An interesting interface layer thickness evolution with increasing temperature should be noted. The interface layer thickness decreases to 0.5 nm with increasing the substrate T_g to 610 °C while disappears when the T_g reaches 650 °C. In this last case, Auger confirm the absence of Si-O ligands while the film remain strongly sub-stoichiometric. The presence of an interface layer means the unavoidable formation of silicate atomic configuration between RT and 610 °C.

3.3.4 Conclusions

In this work, ultra thin films of Lutetium Oxide were prepared by direct electron beam sublimation of Lu_2O_3 powder in an PVD chamber under UHV conditions directly on Si(100) substrates and subsequentely characterized by AES, AFM, LEED and cross-sectional TEM to assess the quality of the epilayer and interface. A systematic study as a function of growth T_g between RT and 650 °C was performed to determine the optimum growth conditions. On the basis of stoichiometry it was found that the best results were obtained at $T_g = RT$ upon O_2 exposure and annealing, while at higher temperature non stoichiometric films have been found. This important result allowed us to determine a feasible and reproducible recipe to grow Lu_2O_3 films on Si(100) which has been used for $in-situ$ experiment that will be discussed in section 5.1.

The characterization reveals several structural characteristics of the films which are directly related to the initial stage of film growth. For example, the unavoidable Si oxidation (Si surface chemically react with O) during deposition indicated by the modification of Si_{LVV} Auger peak and by the TEM images for all the films is a signature of thermodynamical instability of the film in contact with Si. This thermodynamical instability leads to the interface layer formation which has been attributed to SiO_2 and Lu silicate undergrowth due to oxygen or silicon diffusivity. The cluster formation either upon annealing and with T_g above RT may be driven by crystallization of the amorphous Lutetium oxide. Interface layer thickness decreases with increasing T_g and disappears at a T_g of 650 °C. The decrease of the oxygen Auger peak intensity in these films, indicating low oxygen concentration, may be correlated to the high oxygen desorption due to the high substrate temperature. In this conditions, the chemical reaction between Si (no change in Si_{LVV} peak shape) and O is avoided and only a lutetium suboxide films are formed. Finally, clusters formation and in particular the cluster line-up seem to indicate a structural ordering of the film correlated to the Si substrate reconstruction.

Chapter 4

Results

4.1 Y_2O_3/Si(100)

4.1.1 The Y K-edge

In this section I will report the analysis and the results of the experimental XAS data taken from samples of Y_2O_3/Si(100) deposited by molecular beam epitaxy (see table 4.1). The growth of these samples has been described in section .

Sample	code	thickness (nm)	Treatment
Yttria		Reference Powder	none
5	324	20	as-deposited
4	325	4	annealed
3	326	4	as-deposited
2	327	2	annealed
1	328	2	as-deposited
SiO_x		Reference Si Oxide	

Table 4.1: table Sample characteristics. Annealing was performed in situ at 500 °Cfor 30 min immediately after growth.

4.1.2 XAS data and analysis methods

In 4.1 we report the near-edge spectra (XANES) at the Y edge for all the samples and the yttria powder. Spectra have been normalized to equal jump height. The spectrum of the yttria powder is similar to that reported in the literature[84] but exhibits considerably better energy resolution. An overall similarity of the spectra of the samples with that of bulk yttria is apparent; however, all the samples have slightly broadened spectral features, the broadening increasing as the thickness decreases and it is greatest for the 2 nm as deposited sample (no. 1). In order to gain further understanding of the XANES line shape simulations within one-electron real space full multiple scattering theory were performed, using the FEFF 8.20 program [47]. In the bixbyite structure the cation has two inequivalent sites (see fig 4.2 from [84]), which we will call *site* 1 and *site* 2 following Jollet et al.;[84] in site 1 all the cation oxygen bonds have the same lengths, while this is not the case for site 2. For the Y *K* edge a cluster consisting of 7 atomic shells around the central Y was used, i.e., of 102 atoms (7 Å)(see figure 4.3). Self-consistency was imposed up to a radius of 3.5 Å. The muffin-tin approximation to the atomic scattering potential was used, with a 15 % overlap between the muffin - tin radii. The energy-dependent Hedin-Lundqvist complex potential was chosen for the exchange potential; the obtained simulation were convoluted with a 0.2 eV experimental broadening. In Fig. 4.4 we show the simulations of the Y edge XANES line shape obtained in this way. Since the local atomic structure is (slightly) different in the two sites, variations in the XANES line shapes are possible. As demonstrated in Fig. 4.4, in which we show separately the simulations for the two sites along with

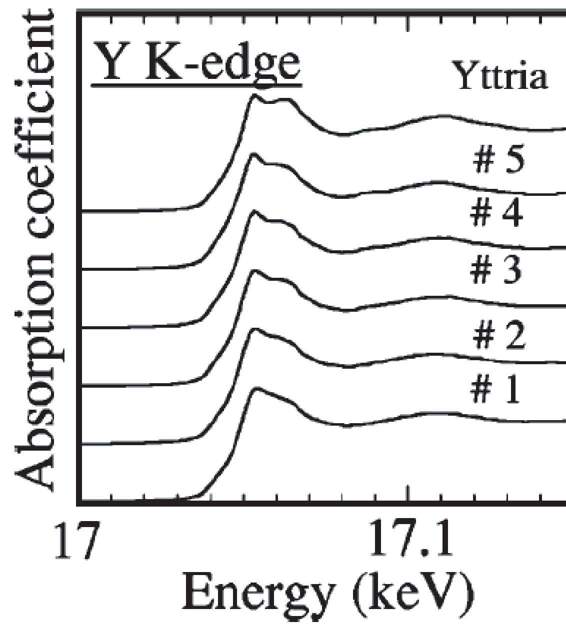

Figure 4.1: XANES spectra at the Y K edge for the five samples of Y_2O_3 epilayers on Si(001) and for bulk yttria.

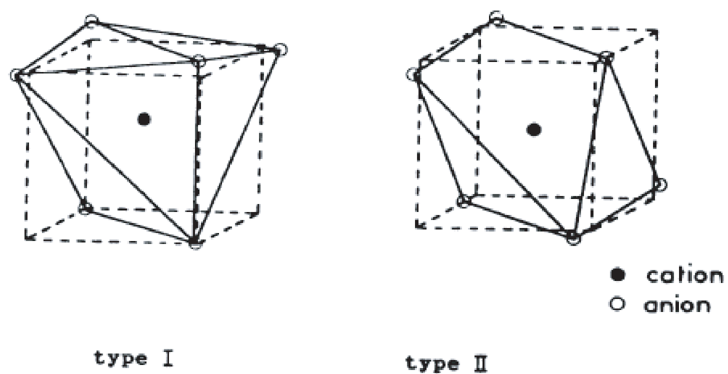

Figure 4.2: Site 1 and Site II of Bixbyite structure.

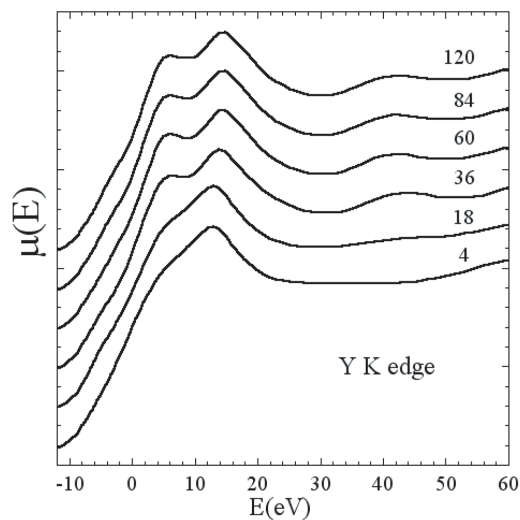

Figure 4.3: Simulated XANES spectra of Y K-edge reported as a function of increasing number of atoms in the cluster centered on the Y photoabsorber atom.

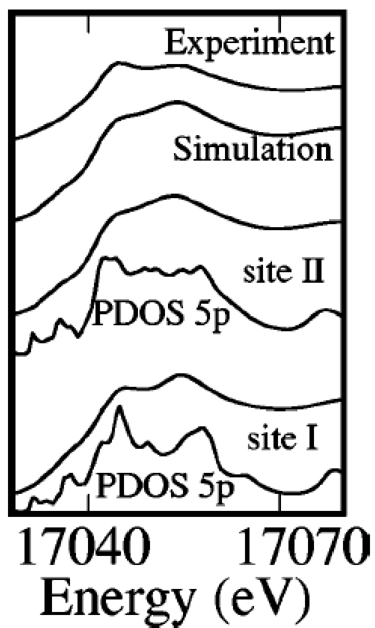

Figure 4.4: Simulations of the Y-edge XANES line shapes with full multiple scattering calculations for the two inequivalent sites in the yttria structure; also shown are the 5p partial density of states on the Y atom. The top curves report the comparison between the weighted average of the two simulations and the experimental spectrum.

the density of states for Y 5p states, the two lineshapes are in fact similar, with that of site 2 exhibiting only a slightly greater broadening, in line with the more disordered environment. At the top of the figure we compare the weighted average of the two simulations with the experimental line shape; the position of the spectral features is correctly reproduced by the simulations, while there are discrepancies in the relative intensities.

Analysis of the Y edge EXAFS data allows to quantify the changes in the local environment. The Y edge EXAFS was analyzed with the IFEFFIT program[85] as implemented in the ATHENA and ARTEMIS packages.[86] The pre-edge background was fitted with a linear function and the atomic background was fitted with a cubic spline. In the inset of Fig. 4.5

we show raw EXAFS oscillations [$\chi(k)$] for sample 4, which illustrates the good signal-to-noise ratio obtained. A Fourier transform (FT) of all spectra was performed in the range 411 Å^{-1} with a k^2 weight and the result is displayed in the main part of Fig. 4.4. Based on the analysis of yttria (see below) the first peak is assigned to Y-O correlations and the second and third to Y-Y ones. It can be clearly seen that sample 5 has a signal bearing a close similarity to that of yttria, and that in going from sample 4 to sample 1 the second peak is progressively damped and the first peak gradually shifts to lower distances. This is a qualitative indication that with decreasing thickness the local structure undergoes disordering and that annealing tends to reduce this effect. The interpretation of the peak shift will be given in the discussion. The first step in the quantitative analysis was the simulation of the Y edge EXAFS signal of yttria based on the one-electron, curved wave, multiple scattering formalism; the FEFF 8.20 program was used.[47] Yttria has the cubic bixbyite Mn_2O_3 structure (space group number 206, $Ia\bar{3}$) with lattice parameter a=10.60 Å[87]. As mentioned above, in this structure Y has two nonequivalent sites, in each of which Y is surrounded in the first coordination shell by six oxygen atoms; for the first site, all O atoms lie at a distance of 2.247 Å, while in the second site the O atoms have a range of interatomic distances with average value 2.295 Å. The second neighbors are Y atoms, 6 of which lie at an average distance of 3.516 Å while another 6 lie at approximately 4.0 Å. In the second Y site there are also two oxygen atoms at 4.01 Å, the contribution of which was however seen to be negligible. The simulations showed that for k >5 Å^{-1} multiple scattering signals are negligible in this structure; hence, the first three peaks observed in the FT are due, in the order of increasing interatomic distance, to the $Y-O$, $Y-Y$, and $Y-Y$ two-body atomic correlations. Based on the simulations, the Y edge spectra were fitted with a nonlinear least squares routine (ARTEMIS). For yttria and for sample 3, 4, and 5 the analysis was performed in the range $R = 1.34.05$ Å(values uncorrected for the phase shift), that is for the full EXAFS signal. Free variables used during the fitting were a common energy origin shift and interatomic distances and Debye-Waller factors (σ^2) for each shell; the values of the many-body amplitude reduction factor was fixed to the value obtained from analyzing the yttria spectrum. Excellent fits were obtained, as illustrated in figure 4.6. The numerical results of the fitting procedure are reported in Table 4.2 and the values obtained confirm the qualitative indications previously mentioned: the interatomic distances are equal to those found in yttria and with decreasing thickness the second and third shell Debye-Waller factors increase.

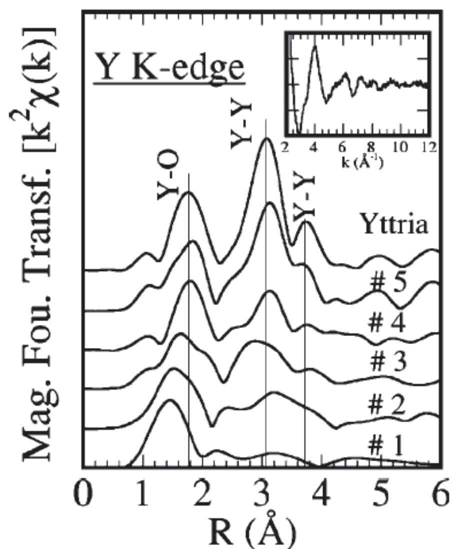

Figure 4.5: Magnitude of the k^2-weighted Fourier transform of the Y edge EXAFS for the five samples of Y_2O_3 epilayers on Si(001) and for bulk yttria; the thin vertical lines identify the positions of the main peaks in yttria. Inset: Raw $\chi(k)$ for sample 4. lines indicate the fitting range in k space.

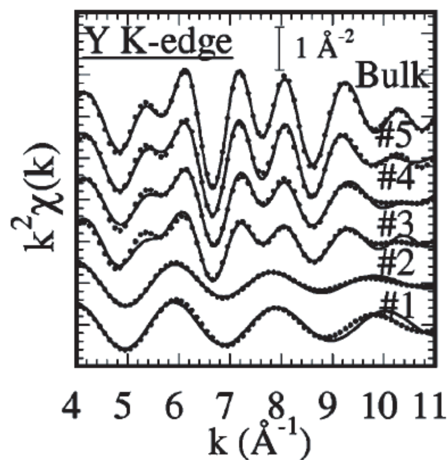

Figure 4.6: Fits in k space of EXAFS spectra taken from Y_2O_3 epilayers on Si(001)

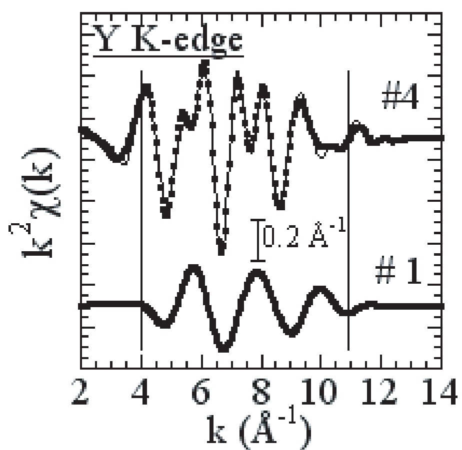

Figure 4.7: Examples of fits in k space for Y_2O_3 epilayers on Si(001) for sample 4 (in the range $R = 1.34.05$ Å) and for sample 1 (limited to the first peak in the FT, range 1 to 2 Å) the thin vertical lines indicate the fitting range in k space.

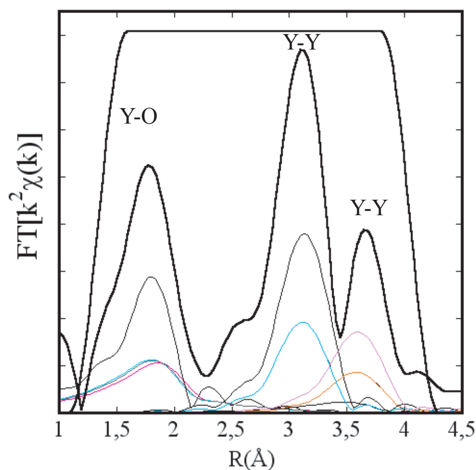

Figure 4.8: Fourier transform magnitude of EXAFS fits for the bulk Y_2O_3.

For samples 1 and 2 it was found to be impossible to reproduce the signal based on a structure similar to that of yttria. The analysis was limited to the first peak in the FT, in the range 12 Å. Even with this limitation it was found that a pure Y-O signal could not fully reproduce the data, as previously described in a preliminary description of our work [88]. In the present paper we confirm the presence of an Y - Si contribution for sample 1 and, in an improvement over our previous analysis, we find that also in sample 2 such a contribution is detectable. The first shell signal of samples 1 and 2 was fitted with a linear combination of Y-O and Y-Si signals; the Y-O signal was based upon the previously described structure of Y_2O_3 while the Y - Si signal was simulated based on the known structure of YSi_2,[89] in which there are two Si neighbors at a distance of 2.07 Å. The parameter w reported in table 4.2 determines the relative weight of the Y-Si first shell contributions sin the YSi_2 structured. In the lower half of Fig. 4.6 we report the best fits for sample 1 and 2. The relative weight of Y-Si contributions was found to be w=0.8 in the as-deposited sample (no. 1) and to decrease to 0.5 in the annealed sample (no. 2).

4.1.3 The O K-edge

In Fig. 4.9 we report the O K-edge XANES spectra for the five samples, the yttria powder and the silicon oxide sample. The spectra for bulk yttria exhibit an overall similarity with those previously obtained by XAS[84] or EELS,[5] but are of much higher quality in terms of energy resolution and signal-to-noise ratio. The comparison of the O-edge XANES spectra of bulk yttria and those of samples 3, 4, and 5 indicates that the local environment of O is very similar; this confirms the conclusions which can be drawn from the Y edge data. Also shown at the top of Fig. 4.9 are full multiple scattering simulations performed using the same method previously described for the Y edge. In this case the cluster radius was 200 atoms (9.0 Å) and self consistency was imposed up to a radius of 2.5 Å; the other parameters were the same as for the Y edge case. The simulation correctly reproduces the main spectral features consisting in the two peaks at approximately 536 eV and 541 eV; however the experimental spectra the two peaks are roughly the same intensity while in the simulation the intensity of the lower energy peak is greater than the intensity of the higher energy one. Also shown at the top of Fig. 4.9 is the p - projected density of states on the O atom, which exhibits similar features as the simulated absorption spectrum. The O K-edge XANES spectra relative to samples 1 and 2 exhibit clear differences with respect to the other samples; note especially that the valley at $\approx$ 538 eV is less deep. A comparison with the silicon oxide spectrum sbottom curve in the figured hints to the origin of this change; in fact, the silicon oxide spectrum has a single peak near the edge (in good agreement with literature spectra for silicon oxide in the $\alpha - quartz$ structure[90, 91]) which has a maximum near 538 eV. In Fig. 4.10 we present selected O K-edge EXAFS data. The inset reports the background subtracted $\chi(k)$ function for sample 5 (continuous line) and yttria (dashed line), which are evidently quite similar. The main part of the figure reports, as the continuous line, a k^2 weighted FT performed in the range 26 Å^{-1}. The relatively limited k range available and the highly distorted local structure limits the amount of quantitative structural information which can be obtained from these

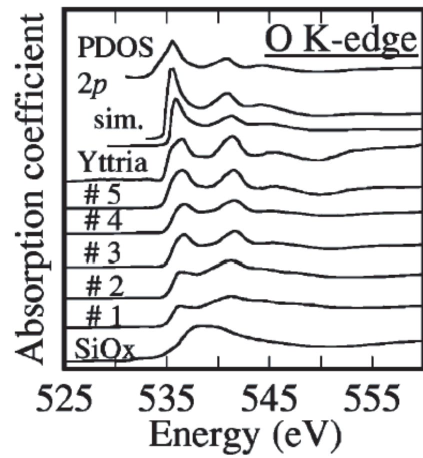

Figure 4.9: O K-edge XANES data for bulk yttria, the five epilayer samples, and for silicon oxide. The top curves report the simulated spectrum and the 2p partial density of states projected on the O atom.

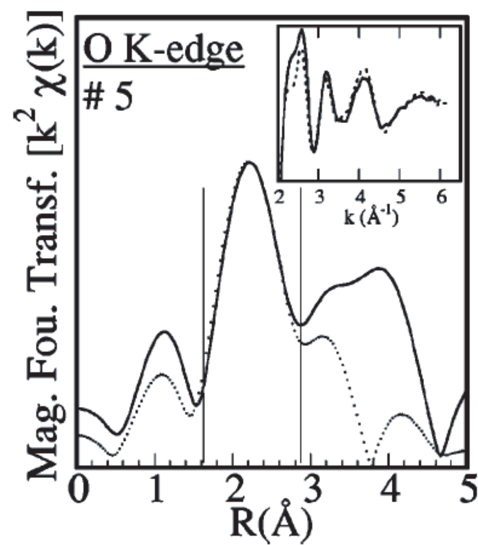

Figure 4.10: O K-edge EXAFS data. The inset reports the $\chi(k)$ function for sample 5 (continuous line) and yttria (dashed line). The main figure shows the magnitude of the Fourier transform (continuous line) and the fit (dots) as described in the text and performed in the R range indicated by the thin vertical lines.

spectra. However, we were successful in reproducing the first peak in the FT (in the range 1.62.8 Å) on the basis of the bixbyite structure of yttria; the first peak is due to the superposition of the signal due to 4 Y atoms at distances 2.2 2.3 Åand to 10 O atoms at distances 2.9 3.7 Å; this is shown as the dashed line. Similar results were obtained in samples 3 and 4. This is a further quantitative confirmation that the local structure in samples 3 to 5 is similar to yttria.

4.1.4 Discussion

From the presentation of the data in the previous section it is apparent that the experimental spectra naturally fall into two categories. Samples 3 to 5 (thickness from 4 to 20 nm) exhibit spectral features similar to those of bulk yttria, while the spectra of samples 1 and 2 show considerable deviations. We make the very reasonable assumption that we can model the samples as composed of a near - interface layer on top of which a Y_2O_3 epilayer grows. Analysis of samples 35 provides information on the local structure of the Y_2O_3 epilayers. Instead, since the thickness of samples 1 and 2 is 2 nm and our probe depth is larger, the analysis of these spectra gives information on the near - interface structure. We will discuss these two issues in turn. The spectra of samples 1 and 2 show considerable deviations. We make the very reasonable assumption that we can model the samples as composed of a near - interface layer on top of which a Y_2O_3 epilayer grows. Analysis of samples $3-5$ provides information on the local structure of the Y_2O_3 epilayers. Instead, since the thickness of samples 1 and 2 is 2 nm and our probe depth is larger, the analysis of these spectra gives information on the near - interface structure. We will discuss these two issues in turn.

Sample	$R(Y_1-O)$ Å	$<R_1(Y_2-O)>$ Å	$\sigma^2(Y-O)$ Å^2	$R(Y-O)$ Å	$\sigma^2(Y-O)$ Å^2	w Å	$<R(Y-O)>$ Å^2	$\sigma^2(Y-O)$	$<R(Y-O)>$	$\sigma^2(Y-O))$
bulk	2.247	2.295					3.516		4.006	
Yttria	2.234(5)	2.304(5)	7(3)			0	3.527(3)	6(1)	4.010	9(2)
5	2.24(1)	2.31(1)	9(5)			0	3.54(1)	7(1)	4.03(2)	10(2)
4	2.23(1)	2.30	7(4)			0	3.53(1)	8(1)	4.01(2)	10(2)
3	2.23(1)	2.30	11(3)			0	3.52(1)	10(1)	4.00(2)	9(2)
2	2.31(2)	2.30(2)	8(3)	2.09(1)	6(3)	0.5				
1	2.3(2)	2.30(2)	6(5)	2.09(1)	6(3)	0.8				

Table 4.2: table Local structural parameters for the yttria reference powder sample and for the samples. Bulk refers to structure of Y_2O_3 as determined by x-ray diffraction (Ref. 29). One standard deviation errors on the least significant figure are indicated in brackets. For the $Y2-O$ first shell, and the two Y-Y second shell contributions the average distance is indicated. w is the normalized weight of Y-Si first shell contributions in the YSi_2 structure relative to the total.

4.1.5 Local structure of Y_2O_3 epilayers

The similarity of the Y- and O-edge XANES line shapes of samples 3 to 5 with those of bulk yttria demonstrates that these Y_2O_3 epilayers have similar unoccupied states electronic structure to that found in bulk yttria. The comparison between the experimental lineshapes and our original full multiple scattering simulations (figure 4.4) is

good and allows a direct connection between the real - space crystallographic structure and the electronic density of states; indeed, assuming the bixbyite structure a good comparison between the experimental spectra and the simulations is obtained. Moreover, this shows that a one electron theory can reproduce the unoccupied electronic density of states of yttria and presumably of other bixbyite structure transition metal oxides. The Y-edge XANES line shapes (figure 4.1) can be compared to the tight binding calculations by Jollet et al.[84] These authors found that the double peak structure is due to a splitting of the p orbitals due to the distorted octahedral geometry around Y. Their calculations predicted a 1.5 eV splitting, significantly smaller than the 8 eV exhibited by our spectra. Our full multiple scattering calculations (figure 4.4) confirm that the splitting originates in the 5p density of states but reproduces its magnitude much better than the tight binding calculations. Coming now to the O-edge XANES spectra (figure 4.9), the double peak structure exhibited by bulk yttria (and other transition metal oxides) can be interpreted within a molecular orbital picture as due to the crystal-field splitting of states derived from O p and Y d atomic orbitals into t_{2g} and e_g (see figure 4.11) states.[84, 92, 93, 94] Our simulations (also shown in figure 4.9)

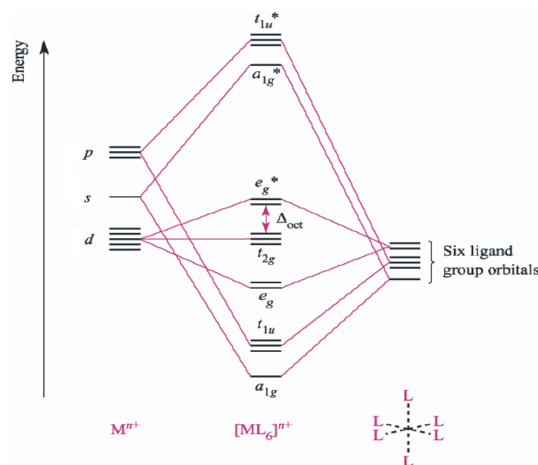

Figure 4.11: O p and Y d atomic orbitals into t_{2g} and e_g molecular orbitals.

reproduce this splitting and explicitly show that it is due to the p-projected density of states on the O atom. It is known that yttria has a tendency to be oxygen-deficient and that this brings about a variation in the relative intensity of the first peak with respect to the second.[92, 5] In the XANES lines shape reported in figure 4.9 for bulk yttria the two peaks have approximately equal height, an indication that the measured powder was not perfectly stoichiometric. Also in samples 3 to 5 the two peaks in the XANES have roughly equal height, suggesting that also the epilayers are, on the average, not perfectly stoichiometric. This is in agreement with the observation by high spatial resolution electron energy loss [5] of lateral oxygen vacancy ordering with a periodicity equal to 13 Å. This evidence, together with the very similar EXAFS signal for bulk yttria and samples 35 (figure 4.10), points to a similar local structure. The quantitative analysis of the EXAFS spectra, the results of which are reported in table 4.2, further illustrates the similarity between samples 3 to 5 and bulk yttria. It is apparent that the bixbyite structure, with its characteristic splitting in the Y-O first shell,

reproduces well the signal for samples 3 to 5. A clear trend is apparent in the values of the Debye-Waller factor for the first and second shells. Upon decreasing the thickness from 20 to 4 nm the Debye-Waller factors increase, with the as-deposited sample sno. 3d exhibiting the highest value of this parameter. The large increase in the second shell Debye-Waller factor causes the decrease of the second peak amplitude in figure 4.5. Assuming there are no changes in the vibrational properties and since all measurements were performed at the same temperature this demonstrates there is an increase in static disorder with decreasing thickness. It is natural to link the observed decrease of local static disorder upon annealing to the observation by electron microscopy that annealing induces a reduction of the density of twin domains and defect superstructure [69]. Extending the validity of this correlation we infer that thinner films exhibit a higher defectivity.

4.1.6 Near interface structure

Significant deviations from bulk yttria are apparent in all XAS spectra for samples 1 and 2 (2 nm thickness). At the Y edge, the most obvious feature is the shift of the first shell peak of the FT towards low R values. As described in the previous section we were able to demonstrate that this is due to the presence of Y-Si atomic correlations. The values reported in table 4.2 are rather informative. First, we notice that the Y-Si interatomic distance found from the fitting (2.09± 0.01 Å) is very close to that found in bulk YSi_2.[89] This is strong evidence that Y-Si bonds are in fact formed. Some of these detected bonds could be those hypothetically formed directly at the interface between Si and the yttria epilayer. However, the thickness of samples 1 and 2 (2 nm) and the high number of these bonds (w=0.8 for sample 1) implies that most of the detected bonds are the result of significant intermixing over the whole thickness of the samples; interface bonds alone would give a significantly smaller value of w. An in situ experiment on even thinner samples would be needed to study the structure directly at the interface, and to test whether O or Y atoms (or both) are bonded to the Si substrate. While the existence of direct Y - Si bonds excludes the formation of an yttrium silicate (in which there are no Y - Si bonds) it must be stressed that our data cannot be interpreted as demonstrating the presence of an extended silicide phase of stoichiometry YSi_2. If such a phase were present, Y-Y correlations at 2.22 Å(present in the YSi_2 structure) should have been detected, which was not the case. We note that the formation of an YSi_2 phase with sufficient long range order to give rise to a diffraction peak has been detected at a deposition temperature of 610 °C[95]. The present samples have been deposited at 450 °C, a temperature at which no such diffraction peak has been detected. The Y-Si bonds observed here must therefore be the precursors of the silicide phase which forms at a higher deposition temperature. We point out that very recently Choi et al.[96] have provided evidence that, in the related $HfO_2/Si(001)$ system, cation-silicon bonds are present and are responsible for catalyzing the reaction between the cation and oxygen to form the interface SiOx layer. Finally, another interesting structural aspect which is apparent from table 4.2 is that all the Y-O distances are approximately 2.30 Å. This implies that the characteristic two sites for Y disappear and the oxygen first shell becomes more symmetric in the interface layer. The

oxygen edge XANES spectra reported in Fig. 5 exhibit strong deviations for samples 1 and 2. The filling-in of the valley at 538 eV and the fact that the silicon oxide spectrum has a maximum at precisely this energy clearly points to the formation of silicon oxide at the interface. The present observation confirms previous data obtained by electron microscopy on similar samples.[95, 69] The annealed sample no. 2 has a slightly more structured double peak, indicating a reduction of the thickness of the silicon oxide layer. This is compatible with previous reports which demonstrated the elimination of the interface oxide layer with annealing at 650 °C;[69] in the present samples, annealing was performed at 500 °C, leading to an only partial elimination of the interface layer. Summarizing the evidence from the analysis of both absorption edges, we find an interface layer characterized by the combined presence of silicon oxide and Y-Si atomic correlations in a configuration similar to those present in YSi_2. Our results should be compared to theoretical predictions on interface stability for yttria on silicon. Using tabulated thermodynamic data, Hubbard and Schlom[97] have calculated the variation of Gibbs free energy for the reaction of silicon with numerous metallic oxides at 1000 K. With this criterion they predicted the reaction of Si and Y_2O_3 to form SiO_2 and Y to be thermodynamically not allowed. No prediction on the possible formation of silicides or silicates was possible due to the absence of tabulated data. Using density - functional theory Marsella and Fiorentini[98] have also tackled this issue, calculating the enthalpy of formation for yttria, silicides, and silicates. They found that yttria is more stable than silicon oxide and yttrium silicide but less stable than the silicate. Our experimental data is in apparent contradiction with both these predictions since we find the formation of an interface silicon oxide layer (most probably amorphous SiO_2, in agreement with previous work) and moreover provide previously unavailable evidence for the presence of Y-Si bonds precursors to the formation of an YSi_2 phase. It therefore must be concluded that the quoted theoretical predictions fail in the vicinity of the interface. It must be pointed out, however, that both theoretical estimates deal with bulk solids and do not include effects which occur at the surface such as those due to low dimensionality, low coordination, adatom diffusion and enhanced reactivity at surface defects and steps.

4.1.7 XANES and electronic structure of Yttrium (Transition Metal) oxide

In order to shed light on the type of transition involved, we present a series of ab initio full multiple scattering calculations of the XANES spectra at the Y and O K edges for bixbyite strucutre by using different choices for the cluster size around the photoabsorbing atom. In this way we try to connect the specific atomic arrangement and the electronic structure of yttrium oxide with the position and intensity of the various features in the observed spectra. We also calculate the projected density of states derived on the basis of the *multiple scattering* (MS) method. From a comparison between the simulated XANES and the calculated partial density of state, we try to reach some conclusions about the assignments of the various spectral features. Reasonable agreement between Y and O K edge experimental data and simulated XANES is achieved with a

cluster consisting of 120 atoms. The following assignments con be proposed for the features in the experimental spectra:

Peaks A1 and A2

In fig 4.12 MS calculations of the O K-edge spectra in the case of bixbyite using different cluster sizes (4, 8, 36, 60, 84 and 120 atoms) are reported. For a four atom cluster,

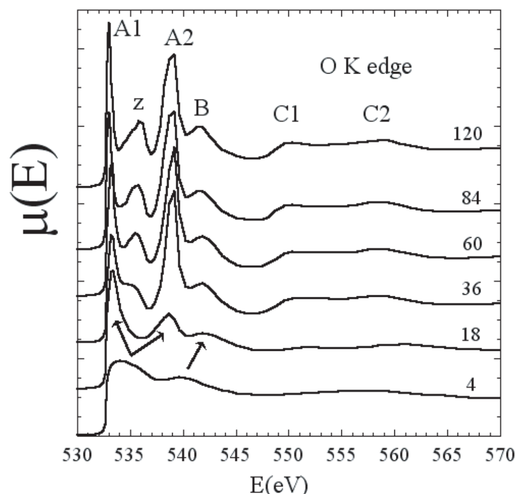

Figure 4.12: Simulates XANES spectra of O K-edge as a function of the number of atoms in the cluster centered on the O photoabsorber atom.

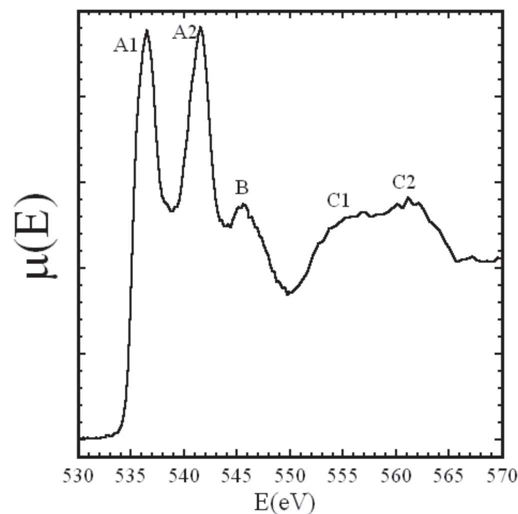

Figure 4.13: Experimental XANES of O K-edge from bulk Y_2O_3.

consisting of an O central atom plus the first coordination shell of four Y atoms a single peak A is obtained, which however is not split into two components. Experimentally this peak splits into two components *A1* and *A2*(see the expertimental spectra in figure 4.17). This feature (In the first $5-10eV$ from the threshold) reflects transition to the O 2p states hybridized with the Y 5d states localized at the Y sites [93]). de Groot et al [93]) have interpreted these two peaks as due to the dipole transitions to band states of $e_g - t_{2g}$ symmetry separated by the *ligand-field splitting*($(O_h$ symmetry-octahedral, see figure 4.11). The t_{2g} orbitals are metal-oxygen π antibonding and lower in energy than the e_g orbitals which are metal-oxygen σ antibonding. In a molecular orbital picture, the *d* orbitals from the transition metal atoms mix with the p orbitals from the oxygen. Hence, $1s-p$ transitions might be expected to reflect to some extent the *d* density of state around the metal atoms. The splitting is infact reproduced by our MS approach when using larger clusters (the simulated spectra is reported together with simmetry prejected Density of States 4.14). In fact the 18-atoms cluster contains the central atom O, its nearest four Y neighbors and the outer neighboring 14 oxygen atoms that provide exactly an octahedral enviroment for these three Y. In the octahedral enviroment the Y d levels result splitted. The doublet A1-A2 is very well defined. This is further evidence that the splitting in the anion spectra is due to the hybridization of the oxygen *2p* orbitals with the transition metal 5d orbitals electrostatically split by the

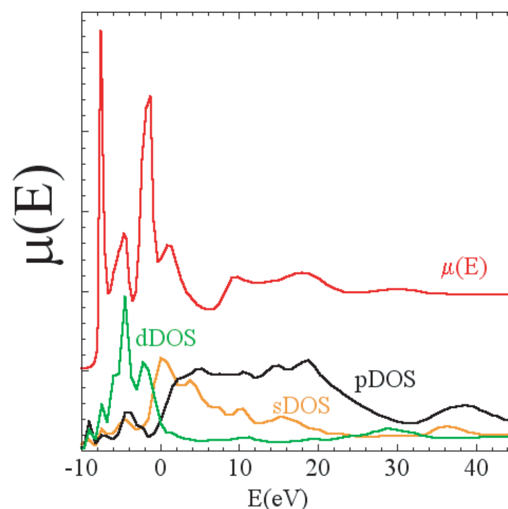

Figure 4.14:

local octahedral crystal filed, as found in other transition-metal oxides [99, 100, 101]. The presence of the z peak between *A1* and *A2* peaks in the simulated spectra is not well understood. A possible explanation might be the finite size of the cluster used for simulation. A second possible explanation may be ascribed to the distorted *Y1* and *Y2* local atomic arrangement respect to a perfect octahedral one. The distortion may lift the degeneracy of e_g and t_{2g} levels. In order to make a comparison with the XANES region measured at the Y K-edge, the experimental (see figures 4.15) and the simulated (see figures 4.16) XANES of Y K-edge have been derived. The derivative function allows to highlight the features of XANES region. In fact, as it is seen from figures 4.15 and 4.16 the features A1, A2, B, C1 and C2 (B, C1 and C2 feature will be discussed below) have been resolved.

Peak B

In this second region, from 5 or 10 e to about 30 eV, the B feature can be ascribed to the O 2p orbital hybridized with the weakly structured metallic 4sp band and constitutes an accessible continuum state [93]. More details appear when third shell nearest neighbors oxygen atoms are included to the simulation cluster indicating that XANES are sensitive to long range and multiple scattering effects. This peak reflects transitions to oxygen 2p states hybridized with the more-delocalized transition-metal 5s and 5p (for Y). From our MS calculation we derive that this features is strongly enhanced by multiple scattering within the first oxygen coordination shell. The assumption of distorted octahedral coordination justifies the splitting of 5p level as confirmed by Y K XAS.

Peaks C1 and C2

For a O central atom (Y K-edge), the first shell, including four yttrium atoms, gives rise to a broad peak which corresponds to transition to Y p-like final states. After adding the

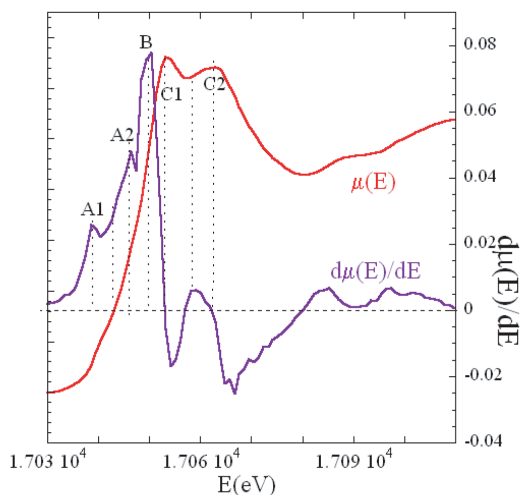

Figure 4.15: Experimental XANES spectra of Y_2O_3 measured at Y K-edge. Its derivative function is reported to highlight the structures of the near edge region.

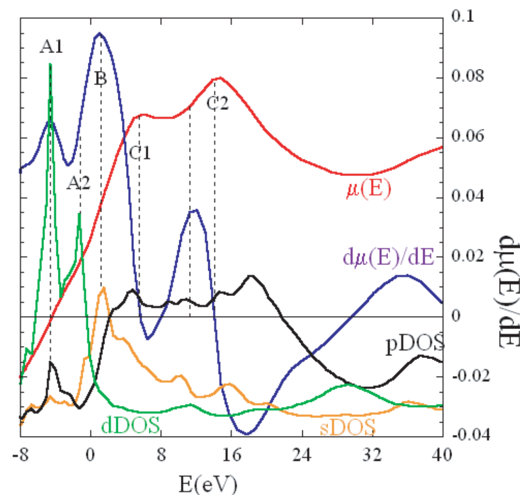

Figure 4.16: Simulated XANES spectra of Y_2O_3 measured at Y K-edge. Its derivative function is reported to highlight the structures of the near edge region.

second shell made of Y atoms, the peak C appears indicating that this feature reflects transitions to Y 5p mixed with 4d orbitals of this higher Y coordination shell. The double peaks *C1* and *C2* appear including the third oxygen coordination shell which complete a quasi-octahedral geometry around the Y of the second coordination shell. The Y 4d levels result splitted by the crystal field. These findings point to the faact that the appearence of the doublet (C1, C2) is due to the interaction of the central Y 5p orbitals with higher-neighbor Y 4d orbitals and show that a 18-atoms cluster is not sufficient to achieve the observed spectral features (see fig.4.15). They are indeed the counter part of the same features as seen from the O *K* edge and for this reason have been labelled in the same way (see fig. 4.12). In the case of Y K edge XAS explore the pDOS projected on the *Y* absorbing atom and thus this *pDOS* results ehanced in intensity respect to that on *O* atom. However it is possibile to highlight the presence of the *pDOS* projected on the *O* scattering potential by plotting the first derivative of $\mu_Y(E)$ (see figs. 4.15, **??**)

Molecular Orbitals

Molecular Orbital (*MO*) calculations are carried out for the YO_6^+ molecule. We performed electronic structure calculations within the *Extended Huckel Molecular Orbital* approximations as implemented in the *C.A.C.A.O.* (Computer Aided Composition of Atomic Orbitals) code [102]. This type of analysis is very powerful to focus on the formation of specific chemical bond(s) within the molecule. In fact we can determine the nature of each molecular orbital resulting from the linear combination of atomic orbitals. We construct an interaction diagram between the sets of molecular orbitals and results are illustrated in figure 4.23. *MO* calculation confirms that the e_g and t_{2g} *d* levels are mixed with the oxygen *p* and hybridized *sp* orbitals. The calculated en-

ergy splitting of $3e_g$ and $2t_{2g}$ MOs is $5.6eV$ in good agreement with the experimental difference between energy positions of peaks $A1$ and $A2$ of O K absorpion edge of Y_2O_3 ($5.7eV$). 4.24. The three-dimensional figures of electronic configuration of e_g and t_{2g} Yttrium d levels mixed with oxygen p and hybridized sp orbitals for the YO_6^+ molecular geometry are reported in figs. 4.18,4.19,4.20,4.21,4.22. Indeed, the direct comparison of MO and $ab-initioMS$ calculations allows a complementary approach to the electronic and multiple scattering information. For example, the MS calculated O K-edge absorption coefficient and in particular the partial d DOS shape (see fig.4.13) in the energy range [-10:0] are understood only if distorted YO_6^+ molecular geometry is considered. Infact, as shown in figure 4.24, the $3e_g$ and $3t_{2g}$ MOs results splitted.

conclusions

Since our one-electron MS theory includes only the dipole-allowed transitions, the good agreement between experimental data and theoretical calculations indicates that all the peaks appearing in the spectra of Y and O K edges correspond to transitions to states which have at least a significant amount of p symmetry. In fact, for the Y K-edge absorption, symmetry considerations show that the p orbitals of the central Y atom can mix with d orbitals of the higher-neighboring Y octahedra.

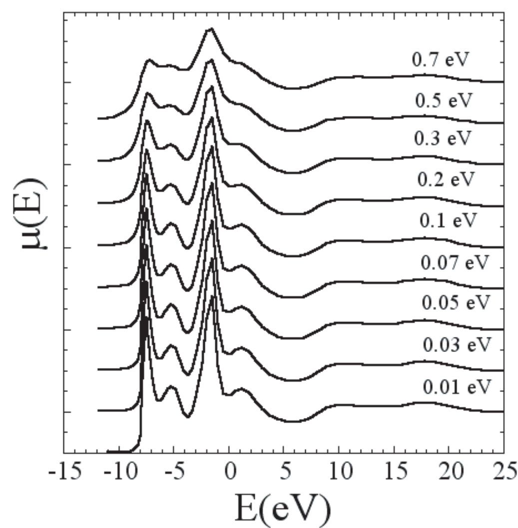

Figure 4.17:

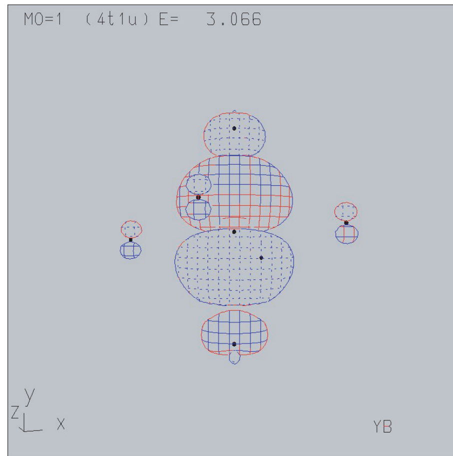

Figure 4.18:

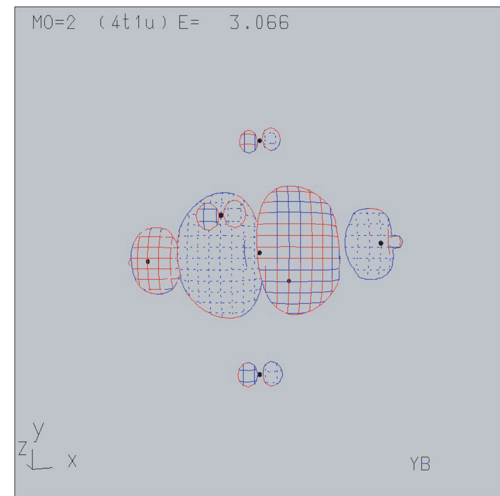

Figure 4.19:

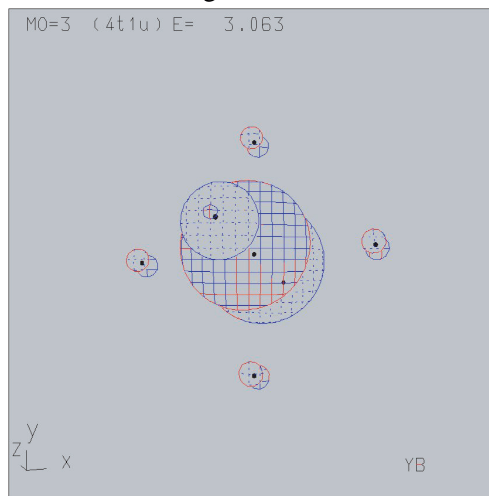

Figure 4.20:

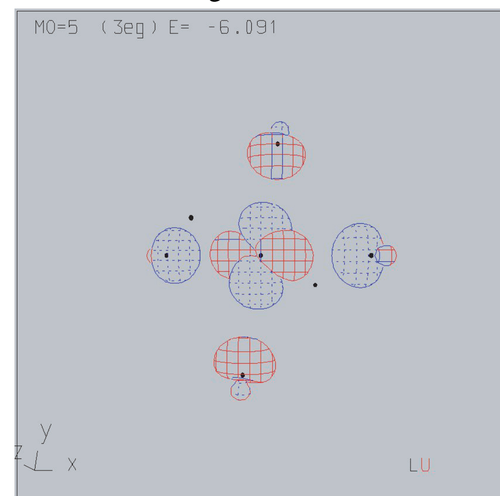

Figure 4.21:

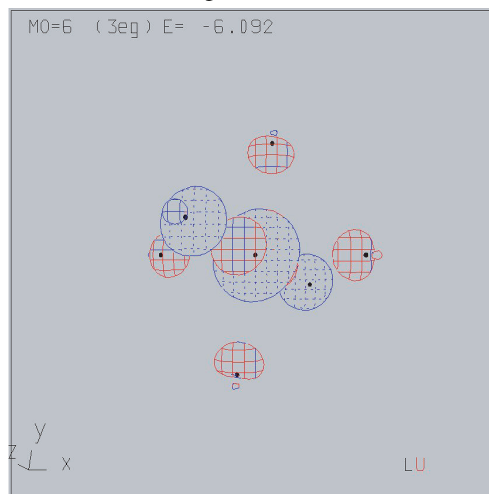

Figure 4.22:

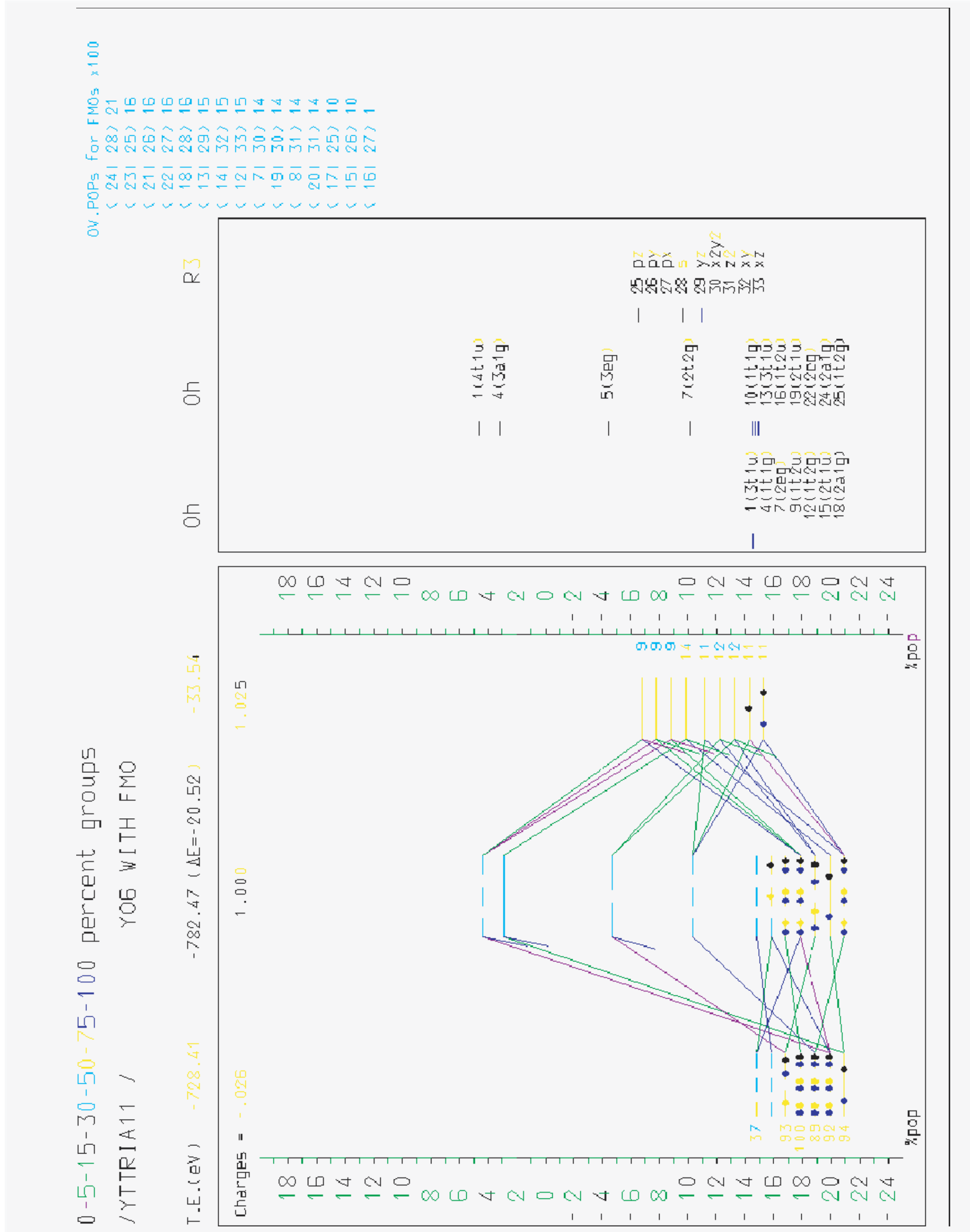

Figure 4.23:

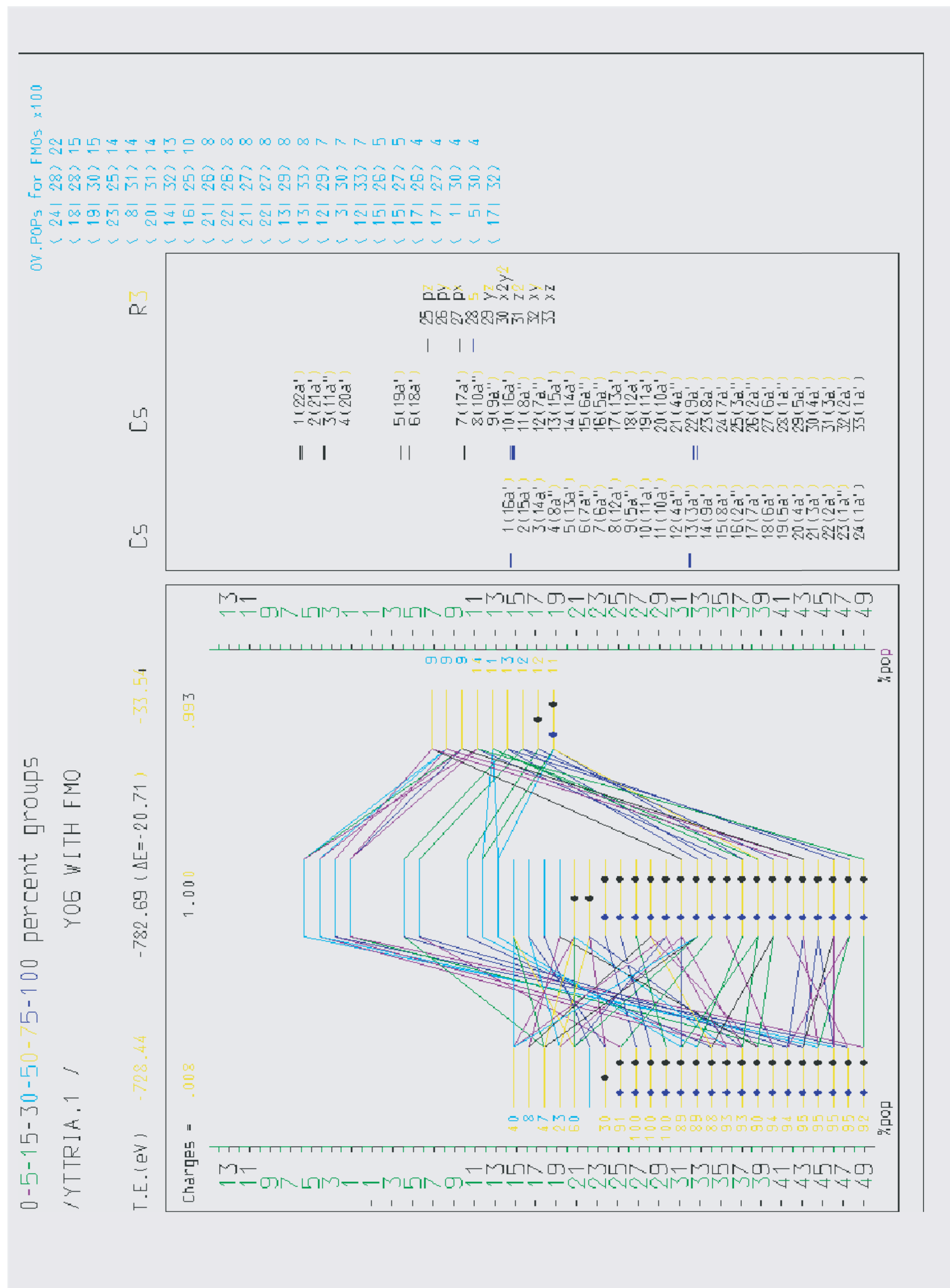

Figure 4.24:

4.1.8 CONCLUSIONS

We have presented a study of the growth of yttria on $Si(001)$, using XAS at both the Y and O K edges. The XANES spectral region has been analyzed with the aid of simulations in the full multiple scattering formalism; these original simulations provide a link between the unoccupied electronic density of states and the atomic structure and have been used to discuss the origin of spectral features in the bixbyite lattice. The EXAFS region has been analyzed up to the third coordination shell for the Y edge. We find that above an $\approx 2nm$ thin near-interface layer the epilayers have a local atomic and electronic structure bearing a close similarity to that of bulk yttria. For thicknesses higher than 4 nm we have detected an increase of the static disorder with respect to bulk yttria which is linked to an increased defectivity. The interface layer exhibits the spectral signature, at the O edge, of the presence of silicon oxide. However, we find that the interface layer has a more complex composition than suggested by previous investigations, since at the Y edge we have been able to detect the presence of Y-Si bonds even at the relatively low growth temperatures here employed, 450 °C. The bonds are the precursors of the long range ordered silicide phase which is formed at higher growth temperatures. Finally, the present results are in disagreement with available theoretical estimates of thermodynamic stability of yttria in comparison to silica and yttrium silicides and silicates, as far as the 2 nm thin interface layer is concerned.

4.2 XAS study of Lu_2O_3/Si(100) and Yb_2O_3/Si(100) films grown by ALD

4.2.1 X-ray absorption measurements and data analysis

In this section we will focus on the analysis of the extended part of the spectra (EXAFS) taken from Lu_2O_3/Si(100) and Yb_2O_3/Si(100) samples grown by ALD. The growth of these samples has been discussed in section 3.2. Bulk Lu_2O_3 and Yb_2O_3 have the cubic bixbyite Mn_2O_3 structure with space group $T_h^7 - I_3^a$ and lattice constants aYb_2O_3=10.436 Åand aLu_2O_3=10.391 Å[77], [78]. The bixbyite structure can be thought of as derived from a fluorite structure (MO_2 stoichiometry) in which one quarter of the anions is removed. There are two inequivalent cation sites, both of which are six - fold coordinated to oxygen atoms in a quasi - octahedral configuration. In site I, all oxygen atoms lie at the same distance (2.19 Åand 2.21 Årespectively for Lu_2O_3 and Yb_2O_3). In site II, O atoms lie at different interatomic distances with average distances of 2.24 Åand 2.27 Å, respectively. Second shell cation- distances are two-fold and four-fold for site I and site II, with a characteristic splitting of 0.3 - 0.4 Å. EXAFS oscillations were extracted from the raw data and analyzed with the IFEFFIT program [85], implemented in the ATHENA and ARTEMIS packages [86]. The extracted experimental EXAFS are reported in Figs. 4.25a and 4.25a. The pre-edge

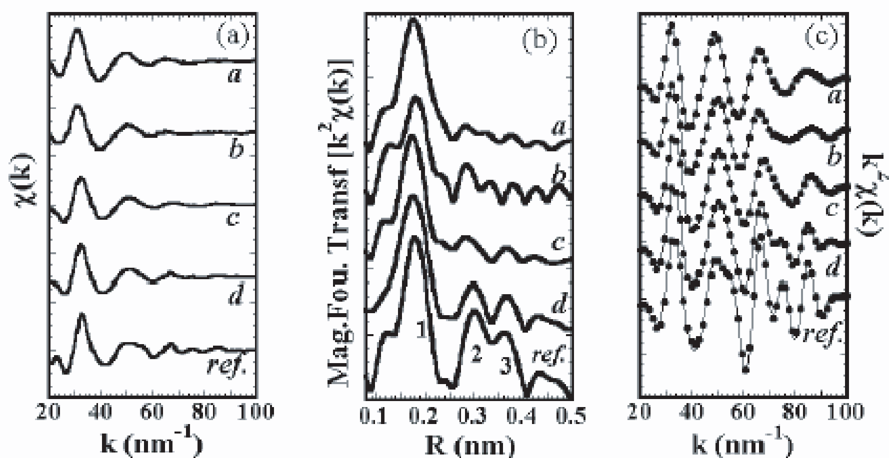

Figure 4.25: Background extracted EXAFS data (a), magnitude of the Fourier Transform (b), and comparison between the inverse Fourier Transform (dotted line) and the fit (solid line) (c) for Lu_2O_3/Si(001) and the powder reference compound.

background was fitted with a linear function and the atomic background using a spline function. In figures 4.25b and 4.26b we report the magnitude of the Fourier Transform (FT) for all the samples, performed in the range $k = 30 - 95nm^{-1}$ with a k^2 weight. The first peak in FT represents RE-O correlations, while the second and third peaks

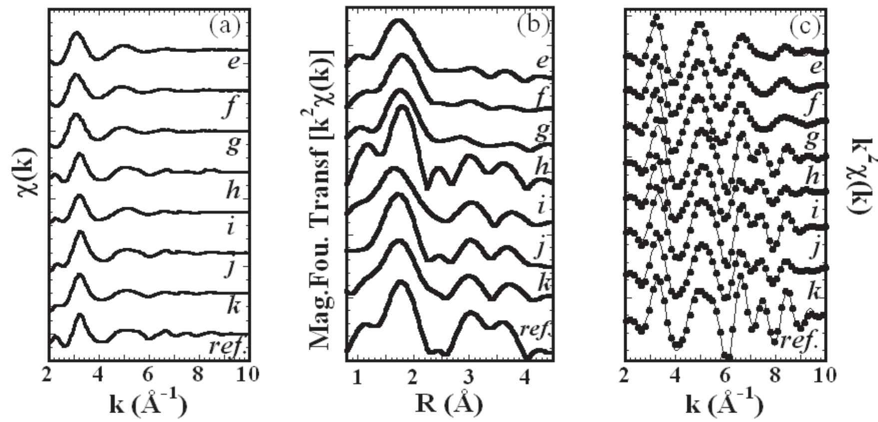

Figure 4.26: Background extracted EXAFS data (a), magnitude of the Fourier Transform (b), and comparison between the inverse Fourier Transform (dotted line) and the fit (solid line) (c) for $Yb_2O_3$3/Si(001) and the powder reference compound.

correspond to RE-RE correlations. The inverse Fourier transforms of the signals were performed in the range $R = 1.21 - 4$ Åfor Yb_2O_3 and in the range $R = 1.31 - 4$Åfor Lu_2O_3. Data analysis was performed by ab-initio modelling of the XAFS signal using the $FEFF8.20$ code based on the one-electron, curved wave, multiple scattering formalism [47]. The theoretical signals were calculated using RE_2O_3 model clusters. The EXAFS spectra were fitted with simulated total EXAFS signals using a non linear least square routine. Fitting parameters were the RE-O and RE-RE interatomic distances and the corresponding Debye Waller (DW) factors. The energy shift and the many-body amplitude reduction factor (S_0^2) were set to the value found for the reference samples. Finally, multiple scattering signals corresponding to RE-O-O paths (second shell oxygen atoms), relatively weak but detectable in reference compounds, were not used for the samples. Indeed, their amplitudes were found to be negligible, presumably because of the disorder in the films, which the fitted DW factors indicate to be larger than in the reference compounds. The results of the fitting procedure are compared to the Fourier filtered data in figures 4.25c and 4.26c, while the numerical values of the fitting parameters are reported in table 4.3. We note here that the scattering phase shifts calculated on the basis of the bixbyite cluster are able to reproduce well the EXAFS data of the reference compounds; however, a significant difference in the values of the interatomic distances compared with the expected ones, is apparent. This discrepancy is most probably due to systematic errors in the ab initio calculation, but has no practical consequences in the discussion of the trends in the local structure of the samples.

4.2.2 Discussion

First of all, we note that the bixbyite structure provides a good basis for a description of the local structure of all the samples. We can safely conclude that the first shell is composed of six oxygen atoms and the second and third coordination shells are composed of RE atoms. While we cannot exclude that other phases are present in small concentrations (say, up to 15 atomic %) the majority of RE atoms are present in a local structure which bears a significant resemblance to that of the bulk compound. However, differences depending on the thickness and sample treatment are apparent, as will be discussed below. Inspection of Fig. 4.25b indicates that the two thinner Lu_2O_3 films a and b exhibit a first shell peak which appears to be at a slightly greater interatomic distance compared to the thicker samples and to the reference; moreover, the second and third shell region is less intense and structured than in the thicker ones. These qualitative differences are borne out by the numerical values reported in table 4.3: the first shell distances are significantly greater for samples a and b than for samples c and d and the reference, and DW factors for the second and third shells are quite high. We interpret a high DW factor as indicating the presence of static disorder (high local bonding distortions). Comparing the two thicker films c and d, we note that the annealed sample d exhibits significantly sharper second and third shell peaks (figure 4.25b) than sample c and this is confirmed by a lowering of the DW factors (table). It is interesting to note that GIXRD indicates that annealing induces a significant crystallization; the EXAFS data shows that crystallization is accompanied by a decrease of the static disorder, as measured by the second and third shell DW factor. The EXAFS results for Yb_2O_3 films exhibit both similarities and differences with those for Lu_2O_3 ones. Thin samples e, f and g all have an expanded first shell distance compared to the bulk, just as for samples a and b. Similarly to the case of the thin Lu_2O_3 samples, the second and third shell structure in thin Yb_2O_3 is weak and this is borne out by the high values of the DW factors. Coming now to the thicker samples h, i, j and k, we note that annealing does not bring about a sharpening of the second and third shell features of Yb_2O_3 samples; in fact, second and third shell DW factors are either constant or actually increase with annealing (compare samples g and h, and j and k). This trend is opposite to that found for Lu_2O_3 samples, but is again in qualitative agreement with the results of GIXRD, which showed that annealing reduces the crystalline fraction of the films. For thicker samples of both RE oxides, by comparing the local structure as probed by EXAFS with the long range order probed by GIXRD, we can conclude that the changes of long range order induced by annealing are accompanied by corresponding variations in the local order, without a change of the basic bixbyite structure. In the thicker samples, XRR detected an IL characterized by an electronic density with a value intermediate between the one of stoichiometric Lu and Yb oxides and the one of SiO_2. The evaluated electronic densities could correspond the Yb and Lu silicates (higher values), or to RE cation - rich SiO_2 layers (lower values). The exact composition of this IL is clearly an important point, since it has implications on the issue of the thermodynamic stability of the RE oxide on Si. Our EXAFS results are compatible with a local structure which is always similar to that of the corresponding bulk RE oxides, with no evidence of a silicate phase. Depending on the thickness of the IL, the

sensitivity of EXAFS to the presence of a silicate varies; moreover the sensitivity can also be expected to decrease if the silicate is highly disordered. In samples in which the IL accounts for approximately 10% of the total thickness, an atomic fraction as high as 50% of an ordered silicate phase in the IL is probably compatible with our data. In samples in which the IL is thicker we can estimate that no more than 10% of RE atoms are present in an ordered interface silicate layer. Higher atomic fractions of silicate are possible in the case of significant local disorder. Concerning the thinner samples, we were able to detect a significant expansion of the first shell (RE - oxygen) interatomic distance for both Yb_2O_3 and Lu_2O_3 films. Understanding the origin of this expansion requires further investigation. Possibly, local distortions induced by the growth process could be at the origin of the phenomenon. The formation of a silicate (at least of such a compound with a significant degree of local order) appears unlikely, since no second shell RE - Si signal could be detected, and any attempt to fit the data with the silicate structure failed. Finally, we note that for Yb_2O_3 samples no significant effect of the substrate preparation is evident (compare samples *e*, *f*, and *g*) and that no clear differences between the local structure of the Yb_2O_3 samples deposited using H_2O or O_3 as the oxygen source are detected (sample *h* and *i* on one hand and *j* and *k* on the other).

Sample	$R(RE_1-O)$ Å	$<R(RE_2-O)>$ Å	$\sigma_1^2(RE-O)$ Å^2	$<R_2(RE-RE)>$ Å	$\sigma_2^2(RE-RE)$ Å^2	$<R_2(RE-RE)>$ Å	$\sigma_3^2(RE-RE)$ Å^2
Cryst.	2.2407	2.2736		3.5319		3.8254	
Lu_2O_3	2.19(3)	2.19(4)	0.001(5)	3.43(3)	0.005(4)	3.92(1)	0.006(16)
a	2.26(2)	2.26(2)	0.003(1)	3.55(3)	0.02(4)	3.94(3)	0.01(1)
b	2.24(3)	2.24(3)	0.006(1)	3.43(7)	0.009(2)	3.64(7)	0.008(3)
c	2.20(3)	2.207(7)	0.004(1)	3.42(2)	0.016(4)	3.68(2)	0.02(1)
d	2.20(1)	2.20(1)	0.0032(7)	3.47(4)	0.011(1)	3.91(4)	0.012(7)
Cryst.	2.2562	2.2451		3.4650		3.9401	
Yb_2O_3	2.21(1)	2.20(1)	0.006(4)	3.44(1)	0.004(3)	3.87(1)	0.007(4)
e	2.25(1)	2.24(4)	0.008(1)	3.50(4)	0.016(6)	3.75(8)	0.02(1)
f	2.26(2)	2.25(2)	0.008(1)	3.43(3)	0.022(7)	3.67(3)	0.03(2)
g	2.27(2)	2.26(2)	0.0080(8)	3.50(3)	0.019(4)	3.75(3)	0.02(1)
h	2.20(1)	2.19(1)	0.007(1)	3.46(3)	0.010(3)	3.85(3)	0.008(3)
i	2.21(3)	2.20(3)	0.009(1)	3.50(2)	0.009(2)	3.92(2)	0.03(3)
j	2.20(2)	2.19(2)	0.005(1)	3.47(1)	0.009(2)	3.86(1)	0.008(2)
k	2.21(4)	2.20(4)	0.008(1)	3.49(2)	0.009(2)	3.85(2)	0.017(8)

Table 4.3:

4.2.3 XANES and electronic structure of Lutetium and Ytterbium oxides

In figures 4.27,4.28, 4.29and 4.30 L_I and L_{III} experimental high resolution normalized absorption spectra of all measured samples together with powder reference sample of both Lu_2O_3 and Yb_2O_3 are reported. L_{III} edge are due to *2p-6d* dipole transitions, while L_I edge are due to *2s-6p* dipole transitions. In fig 4.31 and 4.32, L_{III} edges in the XANES region for both reference samples are reported together with their second derivatives. The latter allow to highlight the intensity distribution of absorption

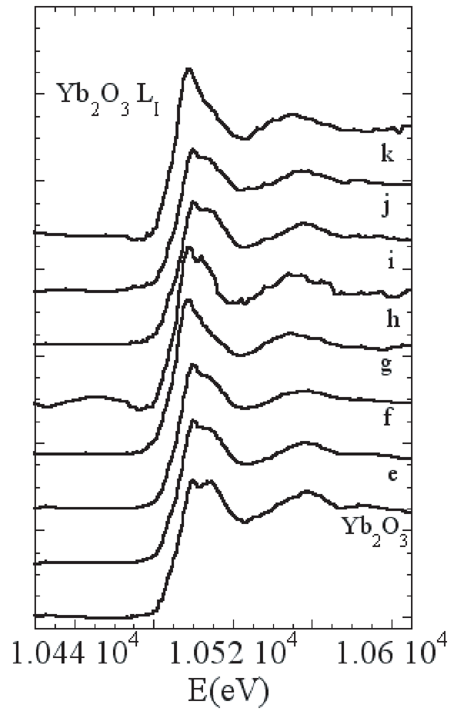

Figure 4.27:

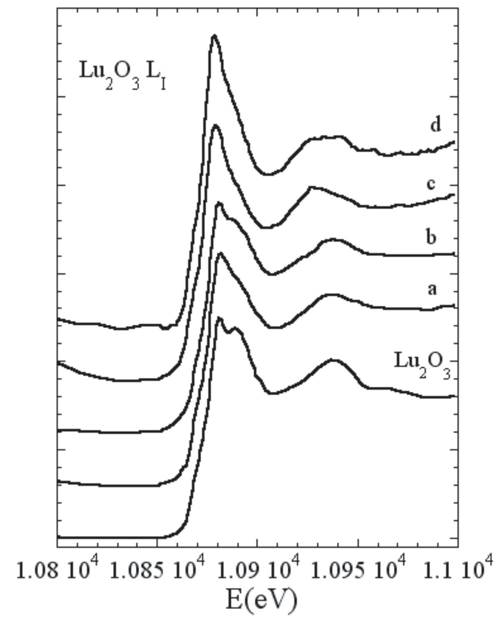

Figure 4.28:

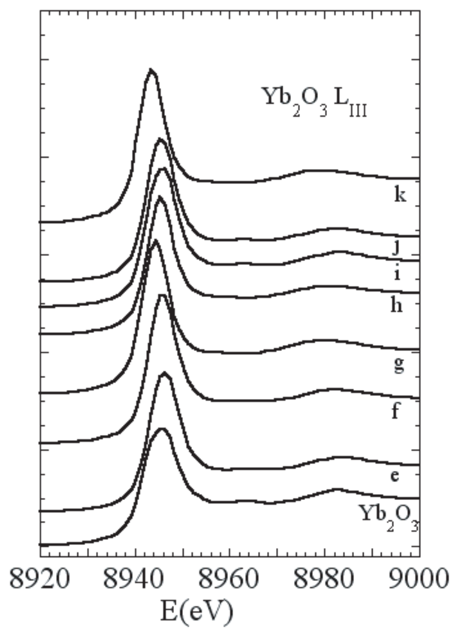

Figure 4.29:

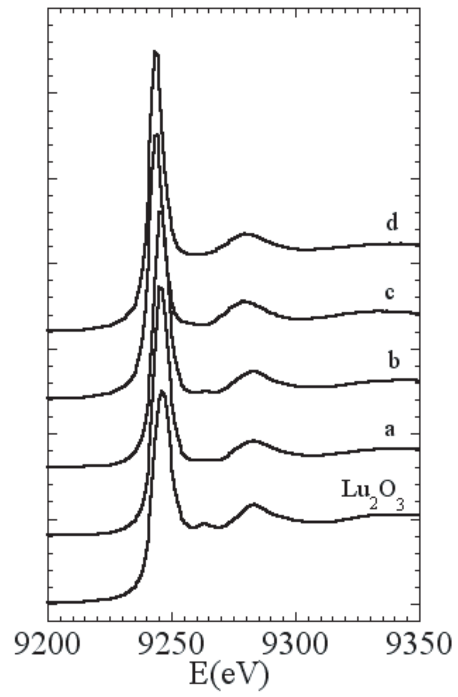

Figure 4.30:

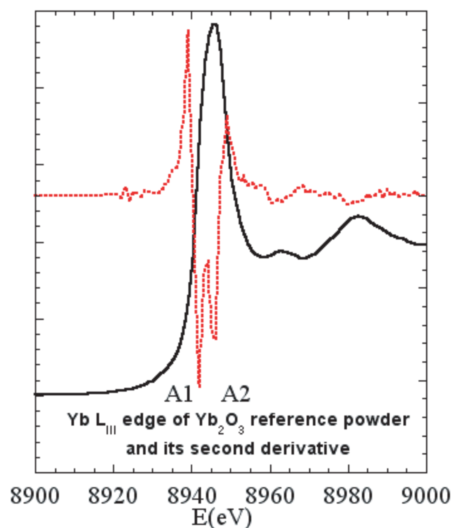

Figure 4.31:

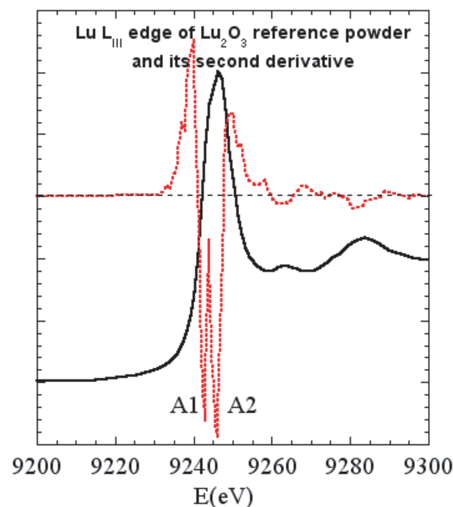

Figure 4.32:

coefficient; the height ratio of the peaks is reported in table 1(da fare) (exp. height ratio for Yb_2O_3 is 1.62, while for lutetia is 0.9.theoretically, $e_g/t_{2g} = 1$ (Lu_2O_3) and = 1.5 (Yb_2O_3)) ; this ratio corresponds to the ratio of the d symmetry density of states anti-bonding Molecular Orbital in Lu_2O_3 and Yb_2O_3 (see table..da fare); this results identify peak *A1* and *A2* (see fig) as due to final states t_{2g} and e_g molecular orbital in the *2s-6d* dipole transitions; however the energy difference of the two molecular electronic states in not equal to that measured at LI edge (circa 3.5 eV per L_{III} e 8eV per L_I) ; even if the final states of the two transitions (L_I and L_{III}) are different, the reason for the reported energy difference is not clear. Another possible splitting of the L_{III} edge may be due to the two kinds of distorted LuO_6 octahedral in Lu_2O_3; anyway the two edges XANES give complementary information about the p and d symmetry density of states of the molecular orbital that form the lowest region of conduction band.

Chapter 5

Atomic and electronic structure of Lu_2O_3/Si(100): $in-situ$ synchrotron radiation photoemission.

5.1 Photoemission measurements

In this section I will describe the Photoemission measurements taken from Lu_2O_3 ultra thin films deposited on Si(100) Physical Vapor Deposition. The films were deposited *in situ* exploiting the PVD source described in section 3.3.

The experiment was conducted at the BEAR (BL 8.1L) [103] beamline at ELETTRA synchrotron radiation facility (Trieste, Italy). Photoemission data were taken with a double-pass Perkin-Elmer cylindrical mirror electron analyzer operated at constant pass energy. Energy resolutions varied according to the different spectral ranges investigated. All spectra were measured at room temperature.

Photoemission spectra were taken from the shallow core levels of the adsorbate (Lu $4d$, O $1s$), from the Lu_2O_3 and Si valence band (VB), from the Si $2p$ as a function of the amount of deposited material (thickness) and post-oxidation. The photoemission spectra were also taken from the core levels O $1s$ and Si $2p$ and VB of a Si substrate with ≈ 30 Å of native SiO_2. the sample was obtained by repeated cycles of chemical reduction and oxidation, with the last step being the oxidation. These spectra were taken as reference. Moreover, x-ray absorption spectra at the O $1s$ edge were measured. The purpose was to focus on the chemical reactions occurring at the interface and to identify bonding configurations through the analysis of spectral lineshape and core level shifts.

$\mathrm{Lu_2O_3}$ ultra thin film samples were grown according to the results obtained in the section 3.3. Samples were deposited *in-situ* by electron beam evaporation of Lu_2O_3 powder, directly on clean Si (100) surface; the substrate was maintained at room temperature in the experimental chamber under UHV conditions. Film with deposition times of 3 min $\approx$ 1 nm (sample B), 6 min $\approx$ 2.5 nm (sample C) and 6 min with post oxidation (sample D) were studied (clean Si surface was named sample A). According to these deposition times, the resulting thickness resulted 10, 26 Å respectively (summary in table 5.1) indicating a growth rate of $\approx$ 1.6Å/min. Growth was performed in

Film	Dep.Time (min)	Thick (Å)
A clean Si surface		
B (1st evap)	3	10
C (2nd evap)	6	26
D (2nd evap + O_2)	6	26

Table 5.1: Deposition times and thickness of the deposited films.

an UHV chamber (base pressure low 10^{-11} mbar).

5.1.1 Si $2p$ core level photoemission

High-resolution photoemission spectra from the Si $2p$ levels taken on the clean Si(100) 2×1 surface and on the deposited films are shown in figure 5.1. The top spectra shows

SiO_2, whereas the bottom spectra represent deposited thin films and clean surface of Si substrate. Spectra were acquired at an emission angle of 45° (8° of angular acceptance) and with a photon energy of 140 eV to ehance the surface sensitivity and with a photon energy of 350 eV to enhance bulk sensitivity. The total energy resolution (photon and electron analyzer) was better than 80 meV. Data are reported in binding energy (see

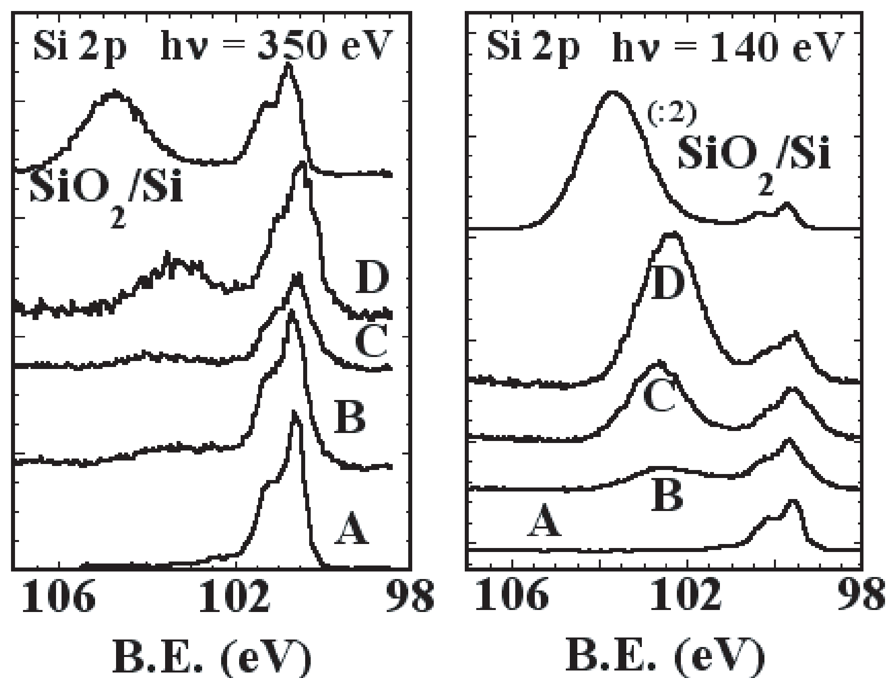

Figure 5.1: Photoemission spectra taken on Si clean surface and on deposited films. Two photon energies of the incoming beam have been used.

figure 5.1) referred to Fermi energy (4.56 eV) which was determined by photoemission valence band measurement of a reference copper sample electrically connected to the sample holder. In order to make quantitative comparison between different spectra and for better comparison on line-shape changes, they have been normalized to the spectra measured on the clean Si surface. Spectra have been normalized to equal height of the bulk $Si2p_{3/2}$ (see figure 5.1). Photoemission spectra of core levels have been deconvoluted according to standard method as illustrated previously in this thesis (section 2.3.1). The program used to analyze the photoemission spectra was XPScasa ([104]). Curve fitting was performed after a Shirley background subtraction and sums of Voigt functions are used to model core level spectra. In the deconvolution of the core level spectra we have followed this procedure:

- The Si 2p spectra of clean Si surface has been deconvoluted and the bulk and surface components resolved and identified according to previous works from literature (Landemark et al. [105, 106, 107])

- The Si 2p spectra of SiO_2/Si has been analyzed according to Himpsel et al [108].

- Finally, the previous resolved components have been used as a building block to fit and deconvolve the experimental spectra taken on the deposited films of lutetium oxide. The energy relative position of the clean surface and SiO_2/Si components are kept fixed and the areas of the components were a fit parameter. Especially when a spectrum consists of many shifted components (as for Si(001) 2×1), a precise identification of their evolution in the presence of an adsorbed species can be difficult: an adsorbate can induce band bending or charging effects in addition to adsorbate-induced shifted components. The method used here permits to evaluate separately band bending, through the observation of the displacement of the clean surface curve, from features arising from bonds.

The fit results for the spectrum taken from the clean surface of silicon are reported in figure 5.2. The Si $2p$ spectrum of the clean Si surface is clearly dominated by the Si^0 ($2p_{3/2}$ and $2p_{1/2}$) double peak. The spectrum is decomposed into components consisting of four Voigt doublets accounting for spin-orbit splitting (see figure 5.2). Best fit results are obtained using a full width at half maximum of 480 meV, a spin orbit splitting of 602 meV, and a branching ratio for $2p_{1/2}$ and $2p_{3/2}$ components of 0.53 (see values reported in the table in figure 5.2). The spectrum and fit results are in good agreement with the work of Landemark et al.([105, 106, 107]). The main difference is that we do not resolve 5 Si^0_{2p} components but 4. Following Landemark et al.[105, 106, 107]), the components of the clean Si(100)-2×1 surface are dimer-up, dimer-down, bulk, second layer respectively. In the original paper by Landemark et al.[107] the components at 0.062 meV (in our case the peak is at 99.04) and -0.485 meV (in our case the peak is at 99.75 eV) correspond to the up and down atoms of asymmetric dimers which results in an energy split of about 0.55 eV between these two components. For this two components we obtain an energy split of 0.71 eV. The component at about 100 eV was assigned to the second layer atoms (see figure 5.3). The deconvoluted spectrum shows the presence of weak silicon oxidized components (at 101.15 eV and 100.50 eV) indicating that the surface was not completely free from oxygen (see figure 5.1 and tab 5.2).
The deconvolution of the photoelectron spectra of Si $2p$ core level SiO_2/Si reference sample reveals four states correlated to the four oxidation states of Silicon. They are chemical shifted from Si^0 $2p$ peak arising from Si substrate by 0.95, 1.75, 2.48 and 3.5 eV respectively. Hollinger and Himpsel [108] found very similar structures and attributed these peaks to Si^{4+}, Si^{3+}, Si^{2+} and Si^{1+} Si oxidation states arising from SiO_2 and three suboxide states of Silicon.
Deconvolution of the Si $2p$ photoelectron spectra measured on deposited thin films reveal that the spectra consist of five components. Among these components, three are associated to the three Si suboxides (Si^{1+}, Si^{2+} and Si^{3+} oxidation states) respectively shifted by 0.95, 1.75 and 2.49 eV; one (highest chemical shift) is correlated with Si^{4+} oxidation states arising from SiO_2; the final one, with intermediate binding energies between Si^{4+} and Si^{3+} (see table 5.2) is associated to Lu-O-Si bonding configurations because electro negativity of Si atom is larger than that of Lu (see figure 5.4 and table 5.2). The components of Si 2p core levels of Silicon surface has been included in the fits. It is worth noting a number of spectral changes between the spectra of deposited

Name	Pos.	FWHM	L.Sh.	Area	%Area	Pos Const
Bulk3/2	99.50	0.364	GL(30)	14439.7	28.320	107.44 , 97.54
Bulk1/2	100.10	0.364	GL(30)	8380.0	16.435	A + 0.602
Surf3/2	99.04	0.364	GL(30)	2801.2	5.494	107.44 , 97.54
Surf1/2	99.64	0.364	GL(30)	1400.6	2.747	C + 0.602
Surf3/2	99.75	0.364	GL(30)	10350.5	20.300	99.75 , 99.7
Surf1/2	100.35	0.364	GL(30)	5175.3	10.150	E + 0.602
surf3/2	100.00	0.364	GL(30)	1336.1	2.620	100.1 , 100
surf1/2	100.60	0.364	GL(30)	668.0	1.310	G + 0.602
SiOxide	101.15	0.653	GL(30)	1962.1	3.848	102 , 100.8
Si Oxide	100.50	0.653	GL(30)	4474.2	8.775	104 , 100.5

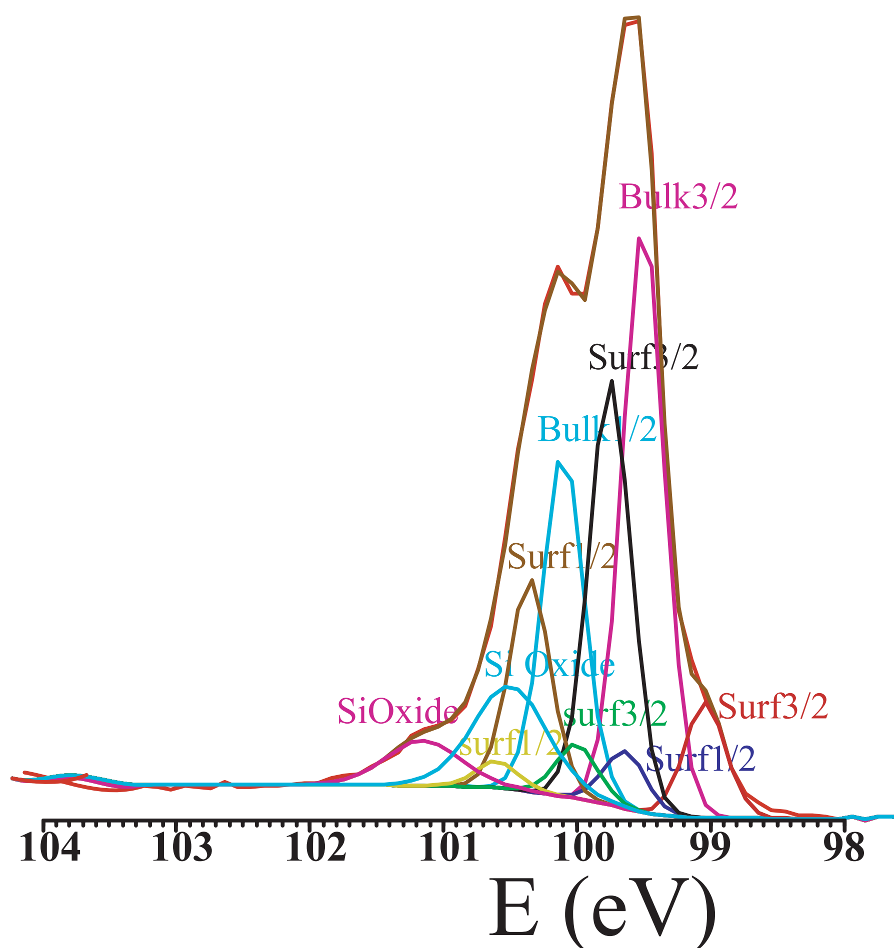

Figure 5.2: Deconvoluted components of Si 2p core level spectra of clean Si. The labels of the components, their energy position in eV (Pos.), their Full Width Half Maximum (FWHM), their Area and the constrain on their energy position are reported in the table.

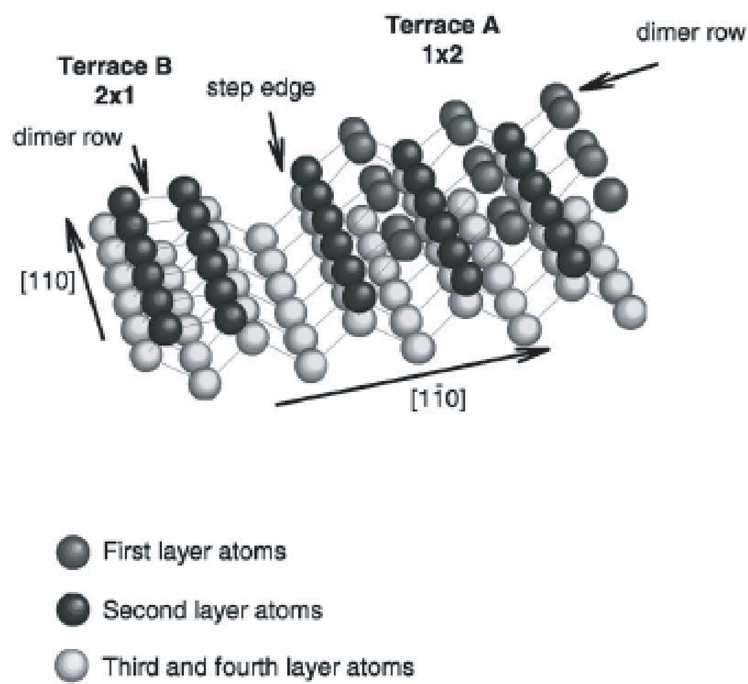

Figure 5.3: Perspective view of the Si(001) double-domain surface with monoatomic steps [109].

film and those of SiO_2/Si and clean Si surface:

- the Si^0 $2p$ substrate components shift to lower binding energy up to 0.2 eV with respect to the clean Si $2p$ and up to 0.3 eV respect to SiO_2/Si reference sample; the shifting is apparent in both surface and bulk sensitive spectra.
- the Si $2p$ oxide peak also shifts to lower binding energy by an amount up to 1.2 eV with respect to the SiO_2/Si case;
- the intensity of the Si $2p$ surface component decreases upon thickness respect to the clean Si case, but the relative intensity respect to bulk Si $2p$ line increases; after post oxygen exposure both overall and relative intensity decrease but do not disappear; this indicates that Si substrate is not completely covered during the exposure to Lu_2O_3 source.Increasing the Lu_2O_3 coverage leads to a general reduction of the Si $2p$ intensity of the Si substrate while increasing the Si $2p$ oxidized components intensity;
- after post oxidation the reacted Si $2p$ peak is still enhanced and it is position is slightly shifted toward lower binding energy (0.5 eV);
- the postoxidation treatment increases the area of the Si^{1+}, Si^{2+}, Si^{3+} and Si^{4+} with respect to as-deposited sample.
- spectral profiles change with deposition time and post oxidation and in comparison with the SiO_2/Si case.

Taken together these data suggest both physical and chemical interactions during the formation of the thin film structure. The bulk core level shifts to higher binding energy may indicate band bending, whereas the modifications of the spectral profile show the formation of silicate and sub stoichiometric silicon oxides.

BE	A (SiClean)	FWHM	B (eV)	FWHM	C (eV)	FWHM	D (eV)	FWHM	SiO_2	FWHM
Si2p3/2	99.72	0.48	99.52	0.628	99.52	0.649	99.56	0.6	99.82	0.5
Si2p1/2	100.33	0.48	100.12	0.628	100.13	0.649	100.16	0.6	100.42	0.5
Si2p3/2surf	98.99	0.48	99.02	0.6	99.02	0.649	99.02	0.6		
Si2p1/2surf	99.59	0.48	99.62	0.6	99.62	0.649	99.62	0.6		
Si2p3/2surf	99.75	0.48	99.81	0.6	99.75	0.649	99.75	0.6		
Si2p1/2surf	100.35	0.48	100.41	0.6	100.35	0.649	100.35	0.6		
Si4+			103.60	1.3	103.6	1.1	103.6	1.1	103.66	1.1
Si3+			102.30	1.3	102.38	1.1	102.30	1.1	102.30	1.1
Si2+			101.55	1.3	101.55	1.1	101.63	1.1	101.55	1.1
Si1+			100.64	1.3	100.64	1.1	100.55	1.1	100.57	1.1
Si-O-Lu			102.88	1.3	102.95	1.1	102.97	1.1		

Table 5.2: Energy positions of the components resolved in the fit of experimental photoemission spectra of Si $2p$ core level taken from the clean Si surface, SiO_2/Si, and samples.

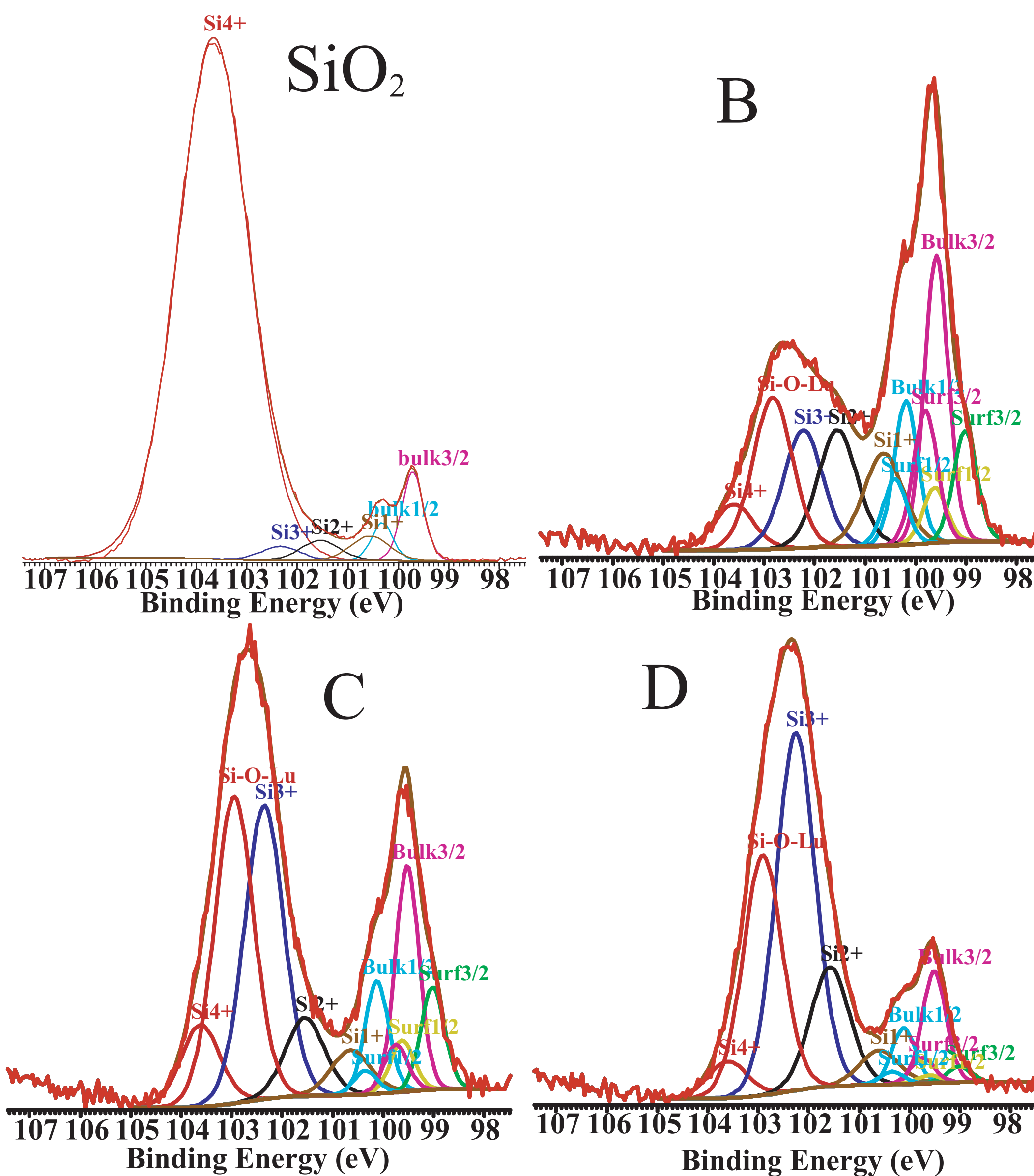

Figure 5.4: The deconvolved spectra of Si 2p core levels taken from SiO2/Si reference sample and Lu_2O_3 ultra thin films are reported in this figure.

5.1.2 O 1*s* core level photoemission

Next we discuss the O 1*s* core level lineshape. O 1*s* spectra recorded on the three thin film samples are reported in figure 5.5. For comparison the spectra of SiO_2/Si (below) is reported too. All data sets were normalized to equal heights for better comparison of line-shape changes. Core level O 1*s* lines were recorded with incident photon energy of 580 eV (pass energy 30eV) in order to achieve photoionization cross section maximization. By performing the deconvolution of the spectra of O 1*s* core level taken from SiO_2/Si reference sample a single state related to Si-O-Si with binding energy at 534.05 eV was found (see figure 5.5). In order to decompose the spectra of

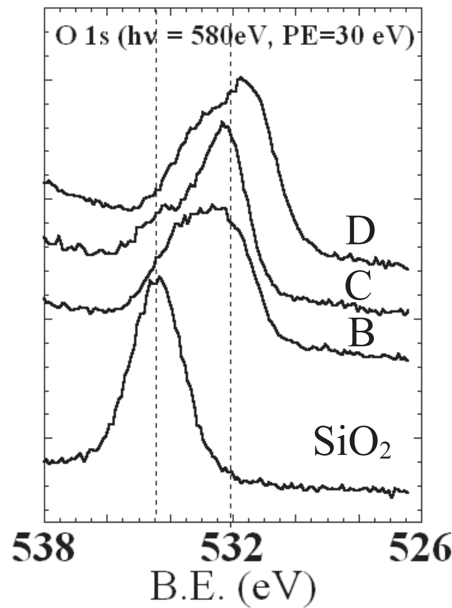

Figure 5.5: Spectra of O 1*s* core level taken from samples and SiO_2/Si.

O 1*s* core level taken from sample B, C and D we followed the spectral decomposition of O 1*s* spectra taken on sample grown by ALD and proposed by Zenkevich et al. [82, 110, 111]. Zenkevich et al. resolved three components with binding energies 532.03 eV, 533.54 eV and 534.42 eV respectively: the first is attributed to O in Lu_2O_3, the second is usually attributed to superstoichiometric O in Lu_2O_3, the third is attributed to $(OH)^-$ groups. Back to our case, in the sample B three oxygen binding configurations were resolved. In fact, the spectrum consists of a peak at E_B=531.98 eV (attributed to Lu-O-Lu bonding configuration), the second peak (named *W* in figure 5.7) at E_B=533.16 eV, the third peak at E_B=534.20 eV (correlated to Si-O-Si configuration as indicated by SiO_2/Si spectrum deconvolution). The nature of the *W* peak (at E_B=533.16 eV) has not been correlated to $(OH)^-$ bonds (as in the case of Zenkevich et al. [82, 110, 111]) because UHV conditions used in our experiment. We propose that the *W* peak at 1.18 eV is due to Lu-O-Si and substoichiometric SiO_x bonding configurations. In fact, since the presence of Lu-O-Si and substoichiometric SiO_x bonding

configurations has been revealed from the analysis of Si 2p core levels, the area and width of the W peak and its energy position correspond to the weighted average of the different binding energies and shapes of all these components. The results of deconvolution of spectra of samples C and D are reported in figure 5.6. According to the

SiO_2

Name	Pos.	FWHM	L.Sh.	Area	%Area	Pos Const	FWHM Const
O2-	534.39	1.926	GL(30)	168.7	98.820	539.44 , 526.54	0.3918 , 9.796

B

Name	Pos.	FWHM	L.Sh.	Area	%Area	Pos Const	FWHM Const
W	533.16	1.569	GL(30)	56.5	35.301	539.44 , 526.54	C * 1
SiO2	534.20	1.569	GL(30)	35.0	21.855	539.44 , 526.54	C * 1
Lu2O3	531.98	1.569	GL(30)	68.5	42.844	539.44 , 526.54	0.2252 , 5.631

C

Name	Pos.	FWHM	L.Sh.	Area	%Area	Pos Const	FWHM Const
W	533.36	1.488	GL(30)	33.6	20.572	539.44 , 526.54	C * 1
SiO2	534.52	1.488	GL(30)	28.7	17.609	539.44 , 526.54	C * 1
Lu2O3	532.19	1.488	GL(30)	100.9	61.818	539.44 , 526.54	0.2252 , 5.631

D

Name	Pos.	FWHM	L.Sh.	Area	%Area	Pos Const	FWHM Const
W	532.68	1.712	GL(30)	49.8	25.538	539.44 , 526.54	C * 1
SiO2	533.54	1.712	GL(30)	37.6	19.284	539.44 , 526.54	C * 1
Lu2O3	531.39	1.712	GL(30)	107.6	55.177	539.44 , 526.54	0.2252 , 5.631

Figure 5.6: Binding energies of the resolved O 1s core levels. The labels of the components, their energy position in eV (Pos.), their Full Width Half Maximum (FWHM), their Area and the constrain on their energy position are reported in the table.

Si 2p case, the relative abundance of each silicate and substoichiometric SiO_x components varies upon the second evaporation and post-oxygen exposure. This is clearly apparent also from the energy position of the component W (SiO_x and silicate) that varies with respect to the energy position of the Lu_2O_3 component and also with respect to the energy position of the centroid (black vertical line in the plots in figure 5.7) of the photoemission spectra of sample B, C and D (B 532.88 eV, C 532.83 eV D 532.12 eV). The centroid has been calculated by the program XPScasa [104] used for the deconvolution of photoemission spectra.

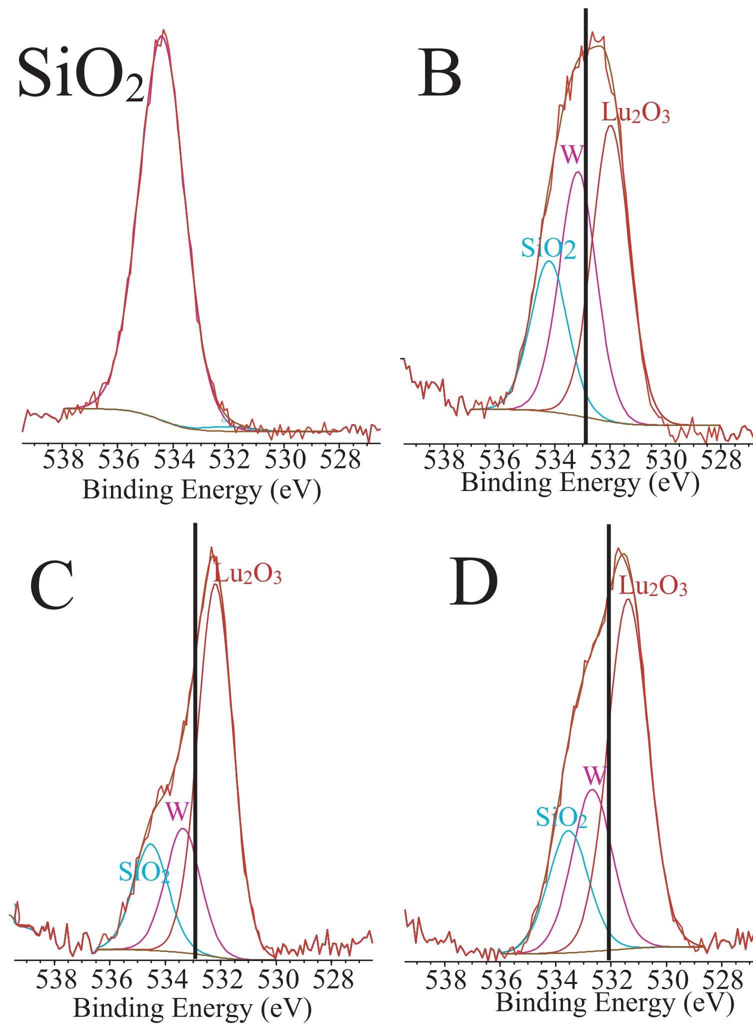

Figure 5.7: O 1s fitted spectra

5.1.3 Valence Band photoemission.

Valence band (VB) spectra were recorded with incident photon energy of 25 eV (pass energy 15 eV) for photoionization cross section maximization; a 15 V negative bias was applied to all samples. Valence band spectra of the A, B, C and D films are reported in figure 5.8. For comparison SiO_2/Si, VB is reported too. In figure 5.9 is reported a VB spectrum from literature ([112]) for comparison with VB spectrum of sample A. Spectra of samples B, C and D are normalized to equal intensity; spectra of the clean surface and of SiO_2 are arbitrary normalized for graphical purpose. The

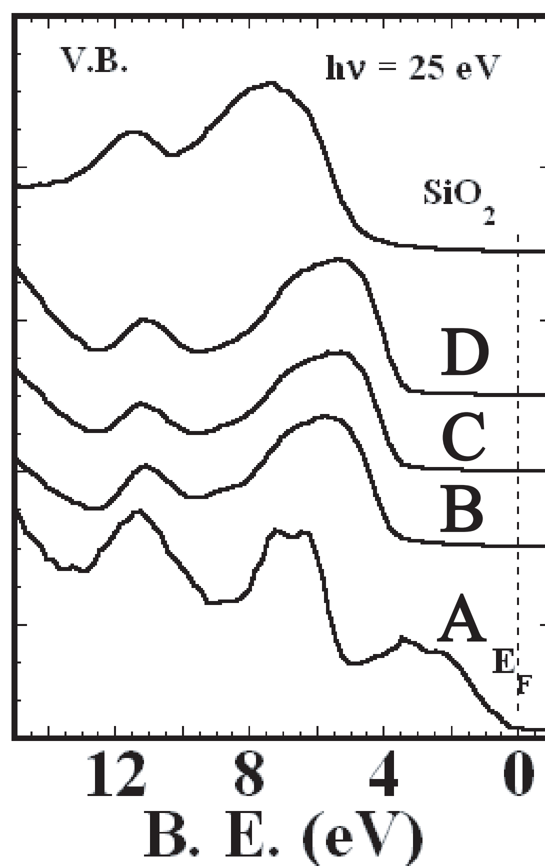

Figure 5.8: Valence band spectra of Si clean surface (c), 1st film 10 Å thick (1), 2nd film 26 Å thick (2), and post oxidized film (3).

SiO_2/Si VB shows emission from the O 2p SiO_2 valence band with structures at 11 eV and between 5 and 9 eV, and the weak intensity between E_F and 5 eV is derived from the underlying Si substrate. The VBs of grown films (figure 5.8) are mainly determined by O 2p character of O-Lu and O-Si bonds in the range 3.5-8 eV from E_F (valence bands consist of O 2p, Si 3p and Lu 5d 5s).

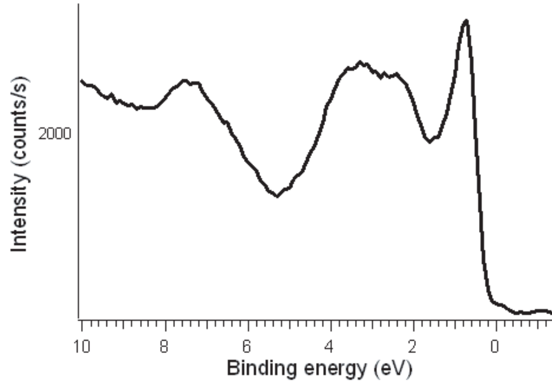

Figure 5.9: VB spectra of clean Si Surface measured at 21.2 eV. We thank Dr. Luca Pasquali for the spectrum.

5.1.4 Offset measurement

In the following paragraph I will illustrate two methods that have been used in order to obtain the valence band offsets between the deposited film and the Silicon substrate. Referring to the clean Si surface case, the onsets of grown layer and substrate VB contribution were clearly identified. In figure 5.10 the changing of maximum of each valence band contribution (VBM) upon film deposition is schematically illustrated. The VBM may be defined with good approximation as the intercept of background intensity level with the linear extrapolation function of the valence band onset; an example is shown in figures 5.11.

Method I In order to obtain the layer/Si VBM offsets, the energy separation between Fermi level an VBM of Si is subtracted from the position of VBM of the layer with respect to Fermi level. We obtained the following values for the valence band offsets ΔE_{VBM}: A 3.16 eV, B 3.14 eV, C 3.01 eV.

Method II An alternative method may be followed to measure valence band discontinuities. A schematic illustration of the method in illustrated in figure 5.10.The valence band discontinuity ΔE_V is given by:

$$\Delta E_V = E_{Si2p-CS} + (-E^{Si}_{VBM-CS} + E^{Si}_{VBM-TF}) - E_{Si2p-TF} \tag{5.1}$$

where CS and TF stand respectively for Clean Surface and Thin Film. The $E_{Si2p-CS}$, $E_{Si2p-TF}$, $E^{Si}{}_{VBM-CS}$ and $E^{Si}{}_{VBM-TF}$ values were extracted from photoemission core level and from the top of the valence band measured on clean Si surface and Lu_2O_3 samples. The position of the Si and grown layer VB maxima in thin film samples has been determined following the Si 2p bulk component shifts respect to reference samples: $E^{Si}{}_V$= Si2p$_{sample}$-(Si2p-$E^{Si}{}_{VBM}$). The core level binding energies, the valence band maximum positions and the corresponding differences are reported in table 5.4.

VB discontinuity values obtained from both methods, are reported in table 5.3 and 5.4, together with literature data on *ex-situ* deposited films (ΔE_V=2.6 eV Seguini at al.[113] and ΔE_V= 3.0 eV Nohira et al. [114]).

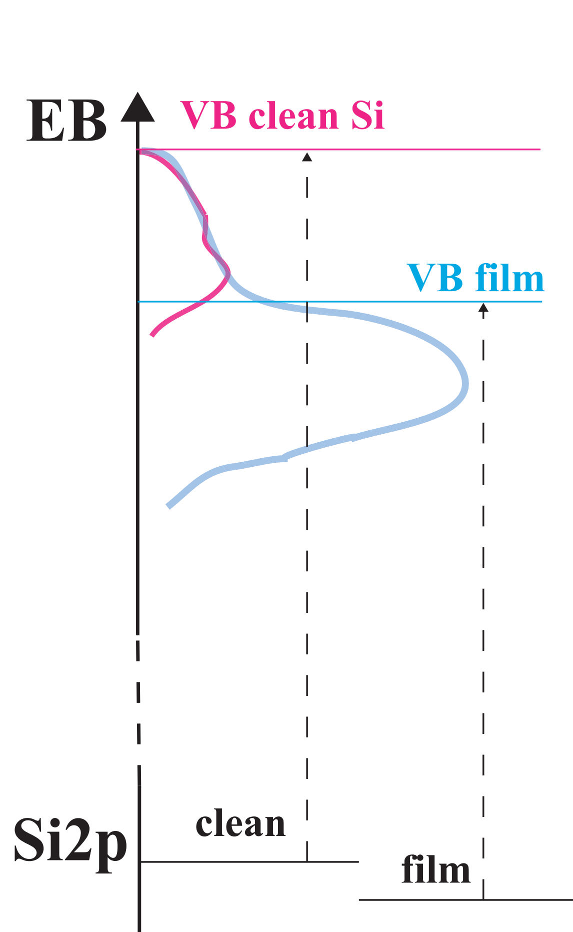

Figure 5.10: Valence band change upon film deposition.

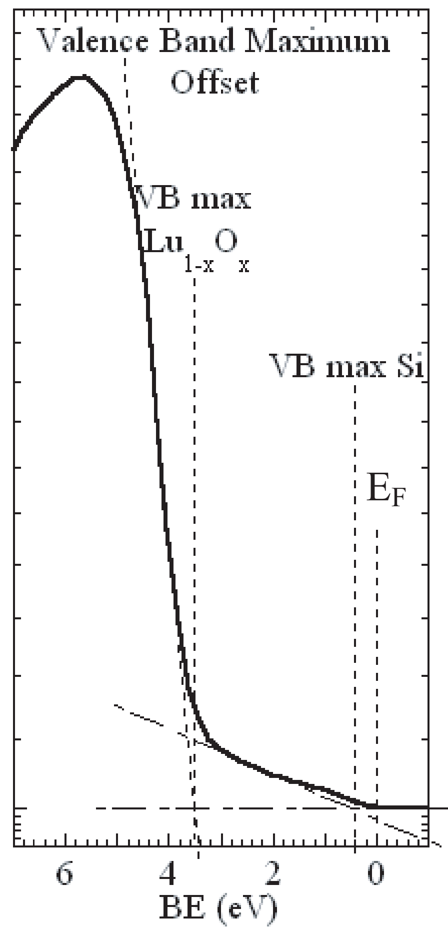

Figure 5.11: Linear extrapolation of the valence band taken from D sample.

The second method, based on core level measurements, allows to track down the binding energy position of the bulk emission which will not be affected by any chemical reaction and will only suffer shifts as induced by band bending. This method may be affected by final state effects like surface photo voltage or oxide charging (core-hole relaxation...). The first method is clearly insensitive to these last effects.

film	Si VBM	Layer VBM	VBO
B	0.41	3.58	3.16
C	0.32	3.47	3.14
D	0.33	3.42	3.09
Clean Si	0.42		
Nohira [114]			3.00
Seguini [113]			2.60

Table 5.3: Method 1

film	Si 2p 3/2 (eV)	VBM (eV)	VBO
B	99.66	3.58	3.22
C	99.57	3.47	3.2
D	99.56	3.42	3.16
Clean Si	99.72	0.42	

Table 5.4: Method 2

5.2 O K-edge XAS spectra.

In this section I will discuss the XAS measurements taken from B, C and D sample during the *in situ* experiment. XAS measurements were carried out in order to make a comparison of the XANES region of O K-edge of samples B, C, and D with that of bulk L_2O_3.

The energy resolution was 200 meV; the typical photon flux on the sample was of the order of 10^{10} photons/s. Measurements were performed by recording the total electron yield in order to enhance the surface sensitivity. The sample was polarized at +100 V in order to avoid electrons excited by the photon beam reaching the photo diode detector. The O K-edge XANES are reported in fig 5.12 in comparison with Lu_2O_3 powder spectra and theoretical simulation and SiO_2/Si spectra; the theoretical simulation was performed within one-electron real space full multiple scattering theory using the FEFF 8.20 program. A comparison between the absorption line shapes in the XANES regions of reference Lu_2O_3 powder and thin film samples suggests that the local atomic and electronic structures of thin films do not matches the known Mn_2O_3 type bixbyite structures of bulk Lutetia; in fact from photoemission data analysis, O K-edge spectra are expected to be linear combinations of absorption edges of oxygen atoms in different bonding configurations. In figure 5.13 is reported a simulated linear combination of O K-edge spectra of bulk Lutetia, SiO_2 and silicate (LuSiO). The components in the linear combination are weighted by the area percentage of O 1s core level lines resolved in O 1s spectra deconvolution. The experimental line shape is well reproduced by the simulates absorption edge.

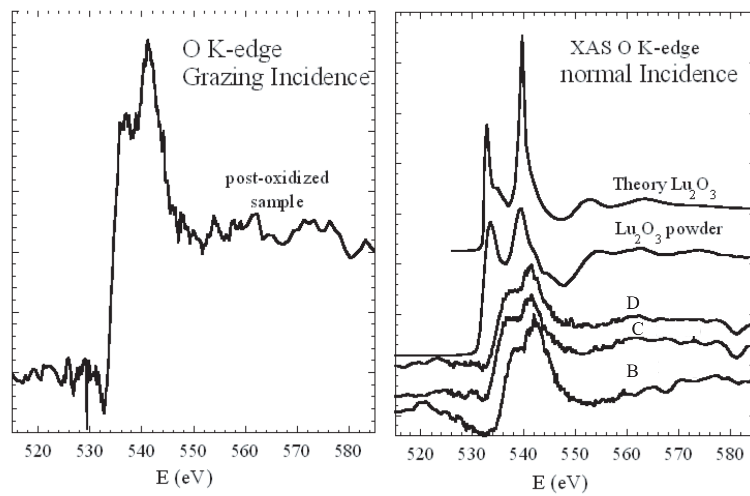

Figure 5.12: Experimental XAS spectra of samples B, C and D. Experimental and simulated XAS spectra of Lu_2O_3 are reported.

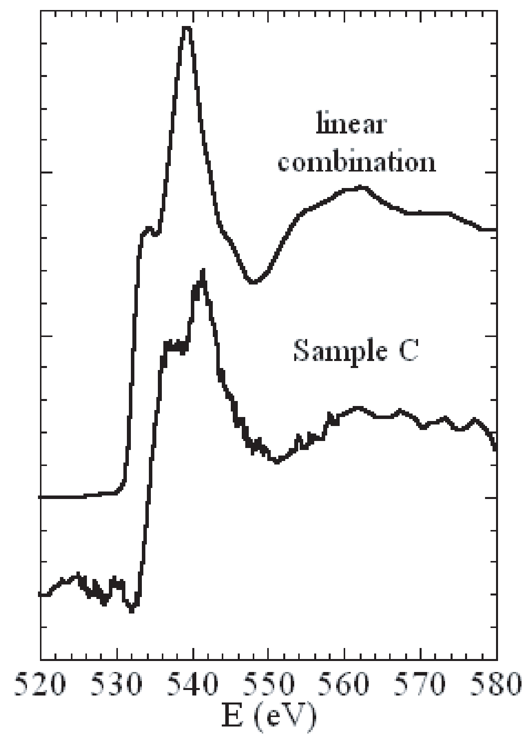

Figure 5.13:

5.3 TEM investigation

The figure 5.14 shows cross-sectional TEM images of Lu_2O_3 grown on clean Si (100) surface. It is seen from figures 5.14 5.15 that the film has a uniform thickness with a flat surface at least over a few tenth of nanometers. The film thickness is in the range 2.3-2.6 nm. The film results to amorphous but crystalline seeds with a diameter of about 10 nm appear (see figure 5.15). The crystalline islands seem to nucleate in correspondence of irregularities of Si substrate. In such regions the EELS profile indicates that the film results to be structured in a stoichiometric Lu_2O_3 overlayer, an SiO_2 crystalline cluster and a lutetium silicate interface layer between the seed and the Si substrate.

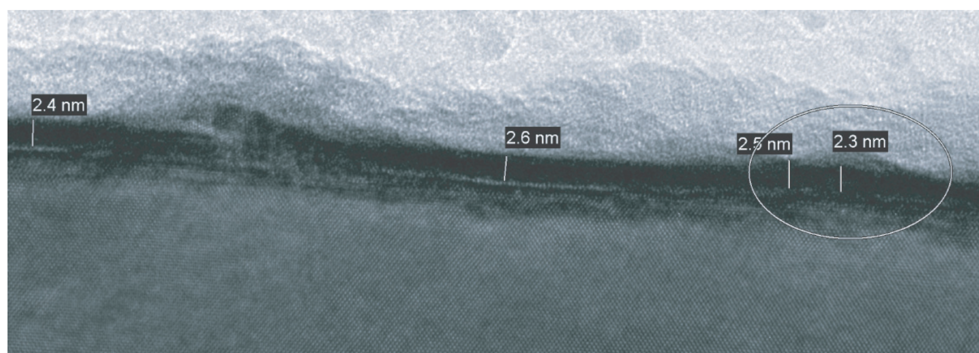

Figure 5.14: Bright field image of cross sectional TEM of Lu_2O_3 film. The ellipse shows the presence of a cluster.

5.4 Conclusions

In this section we have presented an experimental study of the initial stages of the adsorption process during the deposition of Lu_2O_3 film on Si(100) substrate. PES Si $2p$, O $1s$, valence band and XAS O K-edge measurements on a series of three ultra thin film samples reveal that the early stages of lutetium oxide growth on clean silicon are characterized by the formation of different bonding configurations. In fact, O $1s$ and Si $2p$ spectra of sample B, C and D have been deconvolved in Lu_2O_3-like, silicon oxide-like and a silicate like (Lu-O-Si) components. These results may be compared to previous *in-situ* work by Nohira et al. [114] and *ex-situ* work by Scarel et al.[113]. Nohira et al. indicates the presence of a transition layer between Si substrate and the Lu_2O_3 layer in annealed samples with strong predominance of silicon oxides near the interface; while Scarel et al. indicates surface segregation of Si related to surface outdiffusion of interfacial SiO_2 decomposition products after annealing while the signal drops after ion etching indicating its absence in the bulk. Our results show that in the initial stage of as grown sample, Si-O-Lu, Si-O-Si and Lu-O-Lu bonding configurations are formed while there is no evidence of Lu-Si bonds. The relative

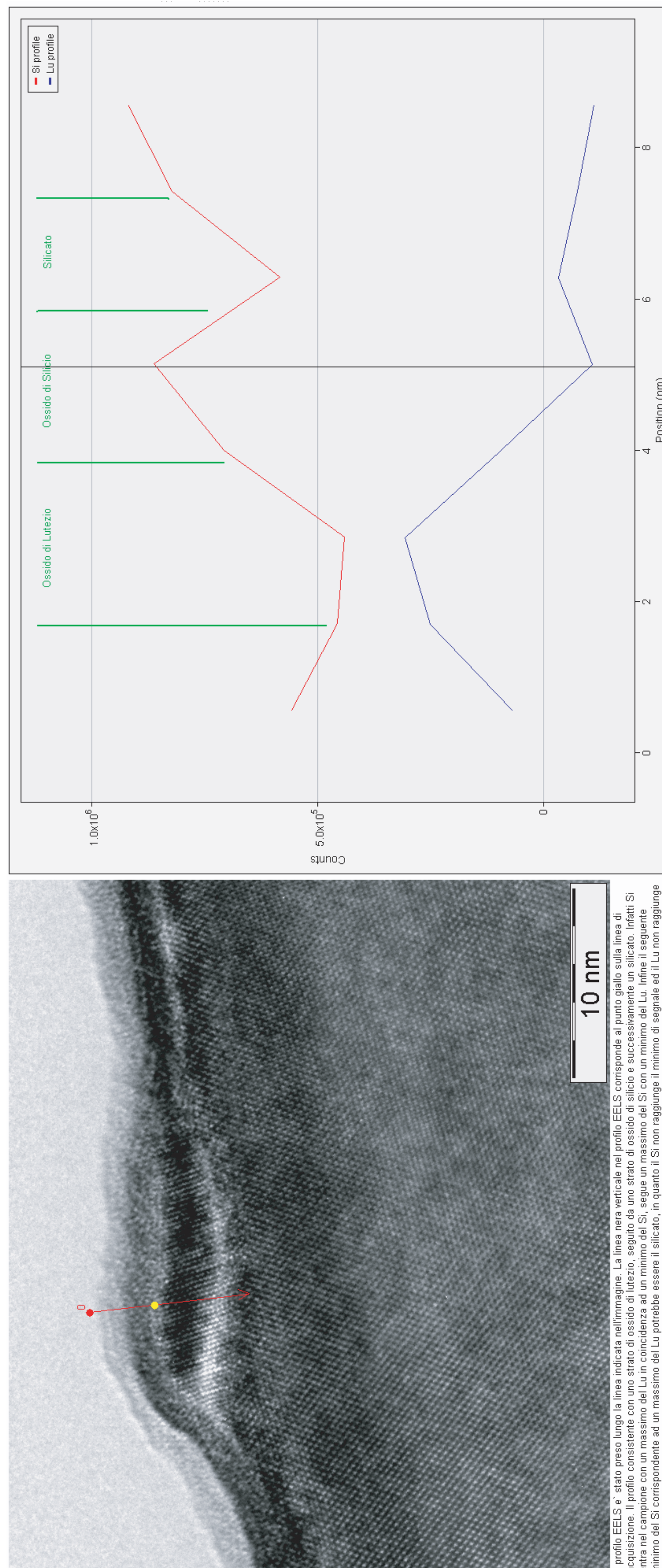

Figure 5.15: The EELS profile has been taken following the line in the image.

abundance of different bonding states varies upon successive evaporation and with post oxygen exposure. Moreover, O absorption K-edge indicate a mixture of oxygen absorbing atoms embedded in different and distorted local atomic Lu_2O_3, Lu-O-Si and SiO_x environments. The presence of structural disorder can be caused (or related to) deviations from ideal stoichiometry.

Conclusions

This thesis work provides a structural and electronic characterization of a class of Rare Earth (Lutetium and Ytterbium) and Transition Metal (Yttrium) Oxide deposited on Silicon (100) substrate. These systems are of strategic importance in the manufactory of microelectronic devices, like complementary metal-semiconductor oxide (CMOS), of the next future.

By means of X-ray Absorption measurements and Photoemission spectroscopy we studied the local atomic and electronic structure of the deposited films in order to have a deep insight on the initial stages of adsorption process of these oxides on the Si substrate. Moreover, we looked for mechanisms underlying the formation of the interface layer between the oxides and the substrate.

Thin films were deposited by means of three different techniques: 1) Atomic Layer Deposition 2) Molecular Beam Epitaxy and 3) Physical Vapor Deposition. We investigated a wide range of growth conditions with special attention to the thickness of the films, the growth temperature and post-growth treatments like annealing and O_2 exposure. As far as the ALD samples are concerned, we investigated samples grown using a series of different optimized precursors.

By exploiting XAS, performed at metal and oxygen edges we found that the interface layer formation between the film and the substrate is unavoidable whichever are the growth parameters considered. We found that this interface layer is most often a non-stoichiometric Si oxide with occasional silicide-like and silicate-like atomic coordination. These assignments, confirmed also by the analysis of Photoemission spectroscopy data, proved the thermodynamical instability of these oxides in contact with Si in all cases investigated.

The Physical Vapor source has been developed as part of this thesis work. A feasible Physical Vapor Source has been optimized and has been demonstrated to work in reproducible conditions and experimentally used to grow ultra thin films of Lu_2O_3 on Si substrate. The configuration of the PVD apparatus set up illustrated in this thesis employed an electron beam gun to sublimate rare earth oxide powder contained in a crucible. The system has been set up with the idea that it might be able to deposit rare earth films directly from a rare earth oxide powder in an opposite way respect to classical MBE technique.

By means of AES, AFM and TEM we have characterized the growth of Lu_2O_3 films on Si(100). We have found that the stoichiometry of the film depends on the substrate temperature and the substrate thickness. Post oxidation procedure contribute to reduce the Oxygen deficiency in the films.

Further results are that the thickness and the presence of the interface layer between the film and the substrate depends on the substrate temperature. Finally, the growth parameters of stoichiometric Lu_2O_3 films on Si(100) have been optimized.

The PVD source and has been successfully used during *in situ* experiments on the BEAR beam line at ELETTRA. These samples have been investigated by Photoemission spectroscopy and clear evidence of the formation of a lutetium silicate-like phase and of Si oxides during the initial stages of film growth have been demonstrated.

Bibliography

[1] Italian Physical Society. In S. Mobilio and G. Vlaic, editors, *Synchrtron Radiation: Fundamentals, Methodologies and Applications*, volume 82, S. Margherita di Pula, 2001.

[2] Cardona. *Photoemission in solids (I and II).*

[3] C. N. Berglund and W. E. Spicer. *Phys. Rev.*, 136:A1030, 1964.

[4] C. N. Berglund and W. E. Spicer. *Phys. Rev.*, 136:A1044, 1964.

[5] G. Apostolopoulos A. Travlos, N. Boukos and A. Dimoulas. *Appl. Phys. Lett.*, 82:4053, 2003.

[6] R. McKee et. al. *Phys. Rev. Lett*, (81):2014, 1998.

[7] Bonera et. al. *Phys. Rev. Lett*, (94):027602, 2005.

[8] F. Boscherini F. D'Acapito S. Spiga M. Fanciulli A. Dimoulas M. Malvestuto, R. Carboni. *Phys. Rev. B*, (71):075318, 2005.

[9] F. Boscherini et al. M. Malvestuto. *submitted to Phys. Rev. B*, 2006.

[10] F. Boscherini et al. M. Malvestuto. *accepted for publication in Nucl. Inst. Meth.*, 2006.

[11] V. Heine et al. *Phys. Rev. B*, (138):1689, 1965.

[12] W. Monch et al. *Surf. Sci.*, (300):928, 1994.

[13] V. Fiorentini and G. Gulleri. *Phys. Rev.Lett.*, (89):266101, 2002.

[14] Karlheinz Schwarz Clemens J. Forst, Christopher R. Ashman and Peter E. B. *Nature*, 427:53, 2004.

[15] Tsu-Jae King Yee-Chia Yeo and Chenming Hu. *J. Appl. Phys.*, 92:7266, 2002.

[16] Sze. Physics of semiconductor devices. *John Wiley and Sons*, 1981.

[17] Monch. Semiconductor surfaces and interfaces. *Springer*, 2001.

[18] Resta Baldareschi, Baroni. *Phys. Rev. Lett.*, 61:734, 1988.

[19] C. G. Van de Walle. *Phys. Rev. B*, 39:1871, 1989.

[20] Robertson. *The European Physical Journal Applied Physics*, 28:265–291, 2004.

[21] R. de L. Kronig. *Z. Phys.*, 70:317, 1931.

[22] H. Fricke. *Phys. Rev.*, 16:202, 1920.

[23] G. Hertz. *Z. Phys.*, 3:19, 1920.

[24] D. E. Sayers, E. A. Stern, and F. W. Lyttle. *Phys. Rev. Lett*, 27:1024, 1971.

[25] D. E. Sayers, E. A. Stern, and F. W. Lyttle. *Adv. X-ray Anal.*, 13:248, 1970.

[26] B.M. Kincaid and P. Eisemberg. *Phys. Rev. Lett*, 34:1361, 1975.

[27] B. K. Teo and P. A. Lee. *J. Am. Chem. Soc.*, 101:2815, 1979.

[28] A. G. McKale, G.S. Knapp, and S.K.Chan. *Phys. Rev. B*, 33:841, 1986.

[29] N. Binsted, S. L. Cook, J .Evans, G. N. Greaves, and R. J. Price. *J. Am. Chem. Soc.*, 109:3669, 1987.

[30] A. Ankudinov R. C. Albers S. I. Zabinsky, J. J. Rehr and M. J. Eller. *PRB*, 52:2995, 1995.

[31] M. Benfatto, C. R. Natoli, C. Brouder, R. F. Pettifer, and M-F. Ruiz-Lopez. *Phys. Rev. B*, 39:1936, 1989.

[32] P. A. Lee and J. B. Pendry. *Phys. Rev. B*, 11:2795, 1975.

[33] C. A. Ashley and S. Doniach. *Phys. Rev. B*, 11:1279, 1975.

[34] W. L. Schaich. *Phys. Rev. B*, 8:4028, 1973.

[35] J. J. Boland, S. E. Crane, and J. D. Baldeschwieler. *J. Chem. Phys.*, 17:142, 1982.

[36] J. J. Sakurai. *Modern Quantum Mechanics*, Rev. Ed., AddisonWesley, 1994.

[37] A. L. Ankoudinov. *Relativistic Spin-Dependent X-ray Absorption Theory, dissertation, University of Washington*, 1996.

[38] L. G. Parrat. *Rev. Mod. Phys.*, 31:616, 1959.

[39] P. Eisemberger P.A. Lee, P.H. Citrin and B. M. Kincaid. *Rev. Mod. Phys.*, 53:769, 1981.

[40] H. Menth E. Sevillano and J.J. Rehr. *Phys. Rev. B*, 20:4908, 1979.

[41] J. M. Tranquada and R. Ingalls. *Phys. Rev. B*, 28:3520, 1983.

[42] E. A. Stern. *X-ray absorption: principles and application techniques of EXAFS, SEXAFS and XANES. J. Wiley*, page 1024, 1988.

[43] A. Di Cicco A. Filipponi and C.R. Natoli. *Phys. Rev. B*, 52:15122, 1995.

[44] B.L. Gioffry. *Phys. Rev. B*, 5:2382, 1972.

[45] P. Lloyd and P. V. Smith. *Adv. Phys.*, 21:69, 1975.

[46] E. Merzbacher. *Quantum Mechanics*, John Willey:34, 1970.

[47] J. J. Rehr A. L. Ankudinov, B. Ravel and S. D. Conradson. *Phys. Rev. B*, 58:7565, 1998.

[48] P. J. Durham. *X-ray absorption: principles and application techniques of EXAFS, SEXAFS and XANES. J. Wiley*, 1988.

[49] A.K. McMahan R. C. Albers and J. E. Muller. *Phys. Rev. B*, 31:3435, 1985.

[50] O. Jepsen J. E. Muller and J. W. Wilkins. *Solid State Commun.*, 42:365, 1982.

[51] M. P. Klein A.S. Robertson G.S. Brown J. Jaklevic, J.A. Kirby and P. Eisemberger. *Solid State Commun.*, 1977.

[52] http://xdb.lbl.gov/Section1/Sec1 3.html.

[53] P.A. Lee. *Phys. Rev. B*, 1976.

[54] P. Eisemberger P. H. Citrin and R. C. Hewitt. *Phys. Rev. Lett*, 1980.

[55] G. Tolkiehn G. Martens, P. Rabe and A. Werner. *Phys. Status Solidi A*, 1979.

[56] R. Frahm R. F. Boehme A. Erbil, G. S. Cargill III. *Phys. Rev. B*, 1988.

[57] P. Ghigna F. DAcapito, I. Davoli and S. Mobilio. *J. Synchrotron Radiat.*, 10:260, 2003.

[58] G. Tondello S. Nannarone G. Naletto, M.G. Pelizzo and A. Giglia. *Proc. SPIE*, 4145:105, 2001.

[59] L. Brillouin. *Science and information Theory, Academic, New York*, 1962.

[60] B. Ravel. *J. Synchrotron Rad.*, 8:314–316, 2001.

[61] A.L. Ankudinov and J. J. Rehr. *PRB*, 56:R1712, 1997.

[62] L. Mattheiss. *PRB*, 133:A1399, 1964.

[63] U. von Barth and L. Hedin. *J. Phys. C*, 5:1629, 1972.

[64] L. Hedin and S. Lundqvist. *Solid state Phys.*, 23:1, 1969.

[65] Doniach S. and Sunjic M. *J. Phys.*, C31:285, 1970.

[66] Tougaard S. *Surf. Interface Anal.*, 11:453, 1988.

[67] Shirley D. A. *Phys. Rev.*, 55:4709, 1972.

[68] Castle J. E. et al. *J. Electr. Spectr. Related Phenom*, 106:65, 2000.

[69] A. Travlos V. Ioannou-Sougleridis A. Dimoulas, G. Veillanitis and A. G. Nassiopoulou. *Phys. Rev. B*, 92:426, 2002.

[70] Th. Matthee G. Friedl A. Bardal, O. Eibl and J. Wecker. *J. Mater. Res.*, 8:2112, 1993.

[71] M. A. Gribelyuk N. A. Bojarczuk S. Guha, E. Cartier and M. C. Copel. *Appl. Phys. Lett*, 77:2710, 2000.

[72] M. Leskela L. Niinisto, M. Ritala. *Mater. Sci. Eng B*, 41:23, 1996.

[73] M. Ritala M. Leskela. *J. Physique IV*, 5:C5–937, 1995.

[74] T. Suntola. *Mater. Sci. Rep.*, 4:261, 1989.

[75] S.K. Streiffer A. I. Kingon, J.-P Maria. *Nature*, 406:1032, 2000.

[76] M. Hummert G. Scarel E. Bonera H. Schumann, I. L. Fedushkin and M. Fanciulli. *Z. Naturforsch.*, 59b:1035, 2004.

[77] File No 40471. Inorganic Crystal Structure Database. *Fachinformationzentrum Karlsruhe*, 2005.

[78] File No 62871 20. Inorganic Crystal Structure Database. *Fachinformationzentrum Karlsruhe*, 2005.

[79] R. Verucchi and S. Nannarone. *Review of Scientific Instruments*, 71(4):3444, 2000.

[80] D. P. Woodruff and T. A. Delchar. *Modern Techniques of Surface Science*. Cambridge, University Press, 1986.

[81] M. P. Seah. *Surf. Sci.*, 32:703, 1972.

[82] G. Scarel., E. Bonera, C. Wiemer, G. Tallarida, S. Spiga, M. Fanciulli, I. L. Fedushkin, Yu. Lebedinskii H. Schumann, and A. Zenkevich. *Appl. Phys. Lett.*, 85:630, 2004.

[83] L. Pasquali, S. D'Addato, and S. Nannarone. *Phys. Rev. B*, (65):115417, 2002.

[84] N. Thromat M. Gautier F. Jollet, C. Noguera and J. P. Durand. *Phys. Rev. B*, 42:7587, 1990.

[85] M. Newville. *J. Synchrotron Radiat.*, 8:322, 2001.

[86] M. Newville B. Ravel. *Proceedings of the 12th International Conference on X-ray Absorption Fine Structure Malm, Sweden,*, 2004.

[87] G. M. Paton and E. N. Maslen. *Acta Crystallogr.*, 19:307, 1965.

[88] G. Tallarida M. Fanciulli M. Malvestuto F.Boscherini F. DAcapito A. Dimoulas G. Vellianitis S. Spiga, C. Wiemer and G.Mavrou. *Mater. Sci. Eng. B*, 47:109, 2004.

[89] J. P. Julien L. Magaud and F. Cyrot-Lackmann. *J. Phys.: Condens.Matter*, 4:5399, 1992.

[90] F. Jollet Z. Y. Wu and F. Seifert. *J. Phys.: Condens. Matter*, 10:8083, 1998.

[91] A.-M. Flank M. Taillefumier, D. Cabaret and F.Mauri. *Phys. Rev. B*, 66:195107, 2002.

[92] M. Gautier N. Thromat F. Jollet, C. Noguera and J. P. Durand. *J. Am. Ceram. Soc.*, 74:358, 1991.

[93] J. C. Fuggle J. Ghijsen G. A.Sawatsky F. M. F. de Groot, M. Grioni and H. Petersen. *Phys. Rev. B*, 40:5715, 1989.

[94] J. J. M. Michiels M. T. Czyzyk M. Abbate and J. C. Fuggle F. M. F. de Groot, J. Faber. *ibid.*, 48:2074, 1993.

[95] G. Vellianitis N. Boukos A. Dimoulas, A. Travlos and K. Argyropoulos. *J. Appl. Phys.*, 90:4224, 2001.

[96] H. Harris S. Gangopadhyay L. Xie K. Choi, H. Temkin and M. White. *Appl. Phys. Lett.*, 85:215, 2004.

[97] K. J. Hubbard nad D. G. Schlom. *J. Mater. Res.*, 11:2757, 1996.

[98] L. Marsella and V. Fiorentini. *Phys. Rev. B*, 69:172103, 2004.

[99] Z.Y. Wu, S. Gota, F. Jollet, M. Pollak, M. Gautier-Soyer, and C.R. Natoli. *Phys. Rev. B*, 55:2570, 1997.

[100] C. Colliex H. Kurata, E. Lefe‘vre and R. Brydson. *Phys. Rev. B*, 47:13793, 1993.

[101] C. Colliex, T. Manoubi, , and C. Ortiz. *Phys. Rev. B*, 44:11402, 1991.

[102] http://www.complang.tuwien.ac.at/cacaojvm/.

[103] A. DeLuisa B. P. Doyle G. C.Gazzadi A. Giglia P. Finetti N. Mahne L. Pasquali M. Pedio G. Selvaggi G. Naletto M. G. Pelizzo S. Nannarone, F. Borgatti and G. Tondello. *Synchrotron Radiation Instrumentation: Eighth International Conference on Synchrotron Radiation Instrumentation, edited by T. Warwich et al., AIP Conf. Proc. No. 705 AIP, Melville, NY*, page 450, 2004.

[104] http://www.casaxps.com/.

[105] E. Landemark. *Ph.D. Thesis, Linkping Studies In Science and Technology*, Dissertation No.313, 1993.

[106] Y.C. Chao R.I.G. Uhrberg, E. Landemark. *Journal of Electron Spectroscopy and Rel. Phenomena*, 75:197–207, 1995.

[107] Y.C. Chao R.I.G. Uhrberg E. Landemark, C. J. Karlsson. *Phys. Rev. Lett.*, 69:1588, 1992.

[108] Hollinger and Himpsel. *Phys. Rev. B*, 28:3651–3653, 1983.

[109] V. P. Ulin N. S. Sokolov G. Selvaggi A. Giglia N. Mahne M. Pedio L. Pasquali, S. M. Suturin and S. Nannarone. *Phys. Rev. B*, 72:045448, 2005.

[110] Zenkevich et al. *Topic on Applied Physics*, in press.

[111] Yuri Lebedinskii and Andrei Zenkevich. *Moscow Engineering Physics Institute, Russia*, (private communication).

[112] C. Y. Su P. Pianetta C. M. Garner, I. Lindau and W. E. Spicer. *Phys. Rev. B*, 19:3944, 1979.

[113] S. Spiga G. Scarel G. Seguini, E. Bonera and M. Fanciulli. *Appl. Phys. Lett.*, 85:5316, 2004.

[114] T. Nakamura K. Takahashi M. Takeda S. Ohmi H. Iwai H. Nohira, T. Shiraishi and T. Hattori. *Appl. Surf. Sci.*, 216:234, 2003.